FORMATION AND EXTRACTION OF A DENSE PLASMA JET FROM A HELICON-PLASMA-INJECTED INERTIAL ELECTROSTATIC CONFINEMENT DEVICE

BY

BENJAMIN ADAM ULMEN

DISSERTATION

Submitted in partial fulfillment of the requirements
for the degree of Doctor of Philosophy in Nuclear Engineering
in the Graduate College of the
University of Illinois at Urbana-Champaign, 2013

Urbana, Illinois

Doctoral Committee:

Emeritus Professor George H. Miley, Chair
Professor James Gary Eden
Professor David N. Ruzic
Professor James F. Stubbins
Adjunct Professor Charles P. Marsh, US Army Corps of Engineers, ERDC-CERL

Abstract

An inertial electrostatic confinement (IEC) device has several pressure and grid-geometry dependent modes of operation for the confinement of plasma. Although the symmetric grid star-mode is the most often studied for its application to fusion, the asymmetric grid jet-mode has its own potential application for electric space propulsion. The jet-mode gets its name from the characteristic bright plasma jet emanating from the central grid. In this dissertation work, a full study was undertaken to provide an understanding on the formation and propagation of the IEC plasma jet-mode.

The IEC device vacuum system and all diagnostics were custom assembled during this work. Four diagnostics were used to measure different aspects of the jet. A spherical plasma probe was used to explore the coupling of an external helicon plasma source to the IEC device. The plasma current in the jet was measured by a combination of a Faraday cup and a gridded energy analyzer (GEA). The Faraday cup also included a temperature sensor for collection of thermal power measurements used to compute the efficiency of the IEC device in coupling power into the jet. The GEA allowed for measurement of the electron energy spectra. The force provided by the plasma jet was measured using a piezoelectric force sensor. Each of these measurements provided an important window into the nature of the plasma jet. COMSOL simulations provided additional evidence needed to create a model to explain the formation of the jet.

It will be shown that the jet consists of a high energy electron beam having a peak energy of approximately half of the full grid potential. It is born near the aperture of the grid as a result of the escaping core electrons. Several other attributes of the plasma jet will be presented as well as a way forward to utilizing this device and operational mode for future plasma space propulsion.

To my mother, father and brother

Acknowledgements

I would like to thank my advisor George Miley and my committee members Gary Eden, David Ruzic, Charlie Marsh, and Jim Stubbins for their guidance during my graduate career at the University of Illinois. Thank you Charlie for the opportunity to do some excellent research for the Army Corps of Engineers. Additionally I would like to thank George for his financial support for my work and for discussions and advice during the course of my dissertation work.

Thank you to my laboratory colleagues, George Chen, Akshata Krishnamurthy, Paul Keutelian, and Drew Ahern and to all the undergraduate students who helped out in the lab over the years.

I want to thank the great friends I've made during my time at Illinois. We navigated the tumultuous waters of the Ph.D. together and although I'm one of the last to complete it, it wasn't a race right?

To Guilherme Amadio, although we didn't get to work together under Professor Miley for very long some of your original handiwork on the chamber still stands. Our conversations about life on the back porch of the union are some of my best memories of my time here. To Alex Ghosh, you were the first person I met at this university and little did I know then, you'd become one of my greatest friends. During the course of our friendship you helped me realize where my true passions lie and I'll take that forward with me when I choose my career path. To Ryan "Tug" Dowdy, our long discussions at Maize brought me new perspective. You taught me about those finer things in life and yes, it's always adventure time. To all those friends too numerous to mention, your support was invaluable.

I would like to thank my girlfriend Yun for being tolerant and supportive of me during the most stressful phase of dissertation and for providing the Stata software at a crucial moment in the data

analysis. You provided the perfect home atmosphere for me to get the most difficult writing done and became my writing buddy as we both worked long hours together.

I want to thank my Grandma and Grandpa for cheering me on for so many years. Thank you grandma for all the cards and letters and the little monetary gifts that helped a poor graduate student enjoy a night out to relax.

To my brother Ross, thank you for continuing to remind me almost every day how I hadn't graduated yet. It was a surprisingly good motivator.

Finally, I would like to thank my parents for their never ending support and keeping me motivated to finish the degree. Mom, you asked me every time we talked if I had good news. After six and a half years, I finally have some! Thank you for keeping me on task and reminding me constantly all the little things I needed to do. Dad, thank you for helping me solve so many of those little problems in life that crop up and for giving me perspective about my education.

Table of Contents

1.0 Introduction and Motivation

Since its invention in the 1960s, inertial electrostatic confinement (IEC) of plasma has shown great promise in a variety of applications as a result of its simple design and ability to confine plasma using only electrostatic fields. In its most simple configuration, an IEC device is a spherical plasma diode. A central negatively biased cathode is inside an outer grounded vacuum chamber that acts as the anode. Ions are confined by the spherical potential well and recirculate through the grid.

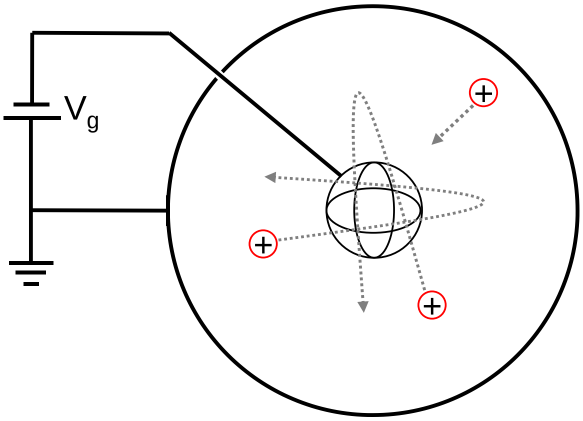

Figure 1. The simple spherical inertial electrostatic confinement (IEC) configuration with the cathode grid biased to a potential of $-V_g$ *with respect to the grounded anode.*

Devices utilizing IEC have already been used to create commercially available portable neutron sources [1]. All applications of IEC devices thus far rely on operation in only one mode, known as star mode. However, IEC devices have another potentially very useful mode of operation called jet mode. In this mode, a jet of plasma emanates from a central grid. This mode has not received much attention in the community because of the damage it can cause to the vacuum vessel if the jet is not specifically targeted into an energy absorbing medium. However, this mode may have application as a new type of electric thruster that we have termed HIIPER.

The special properties of the jet-mode operation in an IEC device could find application in the Helicon-Injected Inertial Plasma Electrostatic Rocket (HIIPER). HIIPER is a new proposed electric space propulsion concept created through the coupling of a helicon plasma source and IEC device. Because of the capability of the IEC configuration to produce potential wells deep enough to initiate fusion reactions, future versions of HIIPER may even be upgraded into an aneutronic fusion system offering a multi-role function as a combined spacecraft power reactor and propulsion system. A fundamental understanding of the jet-mode of IEC operation is required to move this vision forward.

The aim of this dissertation was to provide an initial understanding of the jet-mode operation of the IEC device by the study of key properties of the plasma jet itself. A spherical plasma probe was used to measure the coupling of the helicon plasma source to the IEC device. Coupling these devices was expected to the increase the quantity of ions available to the plasma jet relative to running in DC glow discharge mode. The helicon source is known to be a very efficient means of creating plasma and as such is gaining the attention of the wider IEC community. Two diagnostics were used to explore the electronic nature of the plasma jet. The Faraday cup measured the total plasma current for several plasma conditions while the gridded energy analyzer (GEA) was used to capture the electron energy spectrum. The Faraday cup also used to measure the thermal power in the plasma jet. The power deposited into the cup produced a temperature increase that was used to calculate the total power efficiency of the IEC device in transferring input power into jet power. The final diagnostic, the piezoelectric force sensor measured the force produced by the plasma jet.

This dissertation is divided into 11 chapters. The remainder of chapter 1 discusses the different ion injection and operational modes of IEC devices. Chapter 2 focuses on the previous work performed on the coupling of IEC devices to helicon plasma systems, as well as the previous studies of IEC jet-mode. Chapters 3 through 7 describe the vacuum system and the construction and calibration of the above described plasma diagnostics. The results of all diagnostic measurements are presented in chapter 8. Chapter 9 uses the experimental and simulation results to construct a model of how the IEC jet forms and how the measured properties are affected by changing experimental parameters. Additionally, two limiting calculations are provided that further the understanding of the maximum quantities expected in the device. The first calculation involves examination of a hollow cathode theoretical model to determine the maximum plasma current expected from the jet. The second calculation shows how the various particles in the jet, the electrons, ions and neutral particles contribute to the force measured by the force sensor diagnostic. The conclusions of this dissertation work are summarized in chapter 10. Finally, the potential directions for future investigation are presented in chapter 11.

1.1 IEC Ion Injection and Operational Modes

There are four methods to inject ions into an inertial electrostatic confinement device. They are a glow discharge, electron-emitter assisted discharge, ion gun injection, and plasma injection. In the simplest case, the glow discharge is a DC breakdown of the gas between two electrodes. In the case of an IEC device, the electrodes are concentric spherical grids. The discharge itself is self-sustaining and continuous for as long as the high voltage is applied.

In the electron emitter-assisted discharge, it is possible to sustain plasma at much lower pressures then would be possible for a glow discharge. Electrons are provided into the system by thermionic emitters made from tungsten filaments. These filaments are similar in construction to an incandescent lightbulb and are powered by an alternating current circuit. The electrons circulate around a second grid biased positive relative to the grounded chamber wall causing collisional ionizations with the background neutral gas. The newly-born ions then attract to the central cathode grid. This discharge is not self-sustaining however it has the improved property that the operating voltage of the cathode is independent of the pressure.

Ion gun injection uses an external ion source to drive the discharge or if the background pressure is low enough, nearly entirely provide the source of ions. The operating pressure for this kind of injection is well below 1 millitorr. A major study of different ion gun injection techniques was performed by Y. R. Shaban, a former graduate student of G. H. Miley [2]. Shaban studied a variety of techniques for ion injection into an IEC device. Several ion guns were constructed including a thermal-source ion gun and an inductively coupled radio frequency gun with magnetic indexing coils known as the Illinois Ion Beam Source (ILLIBS). The ILLIBIS in particular was found to have a very high beam efficiency and high current density, however the total power that could be supplied was relatively low due to equipment limitations.

In the plasma injection method, an external source is used however ions are not preferentially accelerated from the source. Rather, the generated plasma is allowed to diffuse into the chamber. This means that only a single grid can be used since the ions would not have enough energy to overcome an additional cathode. The plasma source is typically an inductively-driven wave discharge such as a radio-frequency helicon discharge. Using such a plasma source has several advantages. Similar to the electron-assisted and ion gun methods, plasma injection is pressure independent with respect to the IEC cathode voltage. Additionally, the ion density can be much higher because of the greater efficiency of these sources in ionizing the gas.

When operating a gridded IEC device in a glow discharge, there are three pressure dependent modes. They are known as the central spot, star, and jet (halo) modes so named because of their visual appearance. The star mode is considered normal operation for an IEC device that is attempting to produce nuclear fusions. To initiate the star-mode discharge, first the chamber is pumped down to base pressure. Gas is introduced to about 1 millitorr pressure and a high negative potential is set on the cathode. The pressure is slowly increased until breakdown occurs and the plasma is formed. Optimal star-mode occurs around 12 millitorr background pressure and only for symmetric cathode grids. The formation of ion microchannels which look like rays of light from a star at the center of the grid is the fundamental visual cue of star-mode. The intensity of the microchannels is a function of the cathode current.

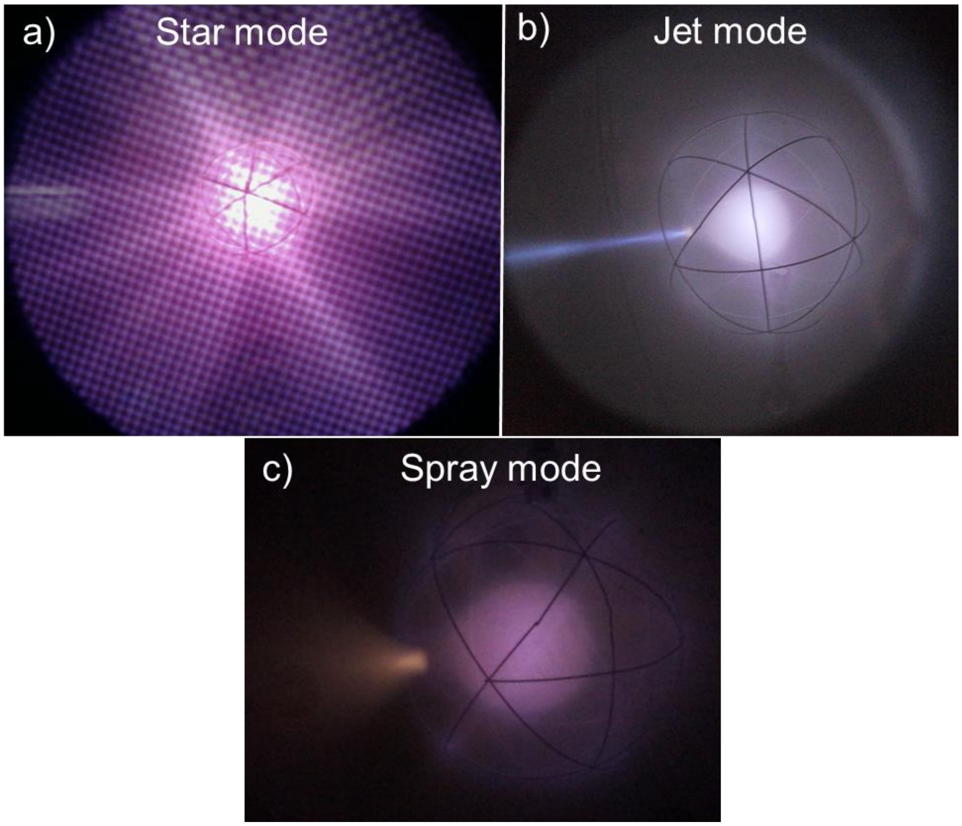

Figure 2. a) Star-mode operation of a symmetric gridded IEC device denoted by the plasma microchannels around the grid. b) Jet-mode propagating from an asymmetric gridded IEC device. The bright plasma jet is clearly visible emating from the central core. The grid shown is ~126 millimeters in diameter. c) The spray-mode occurs when an asymmetric grid is run at a higher pressure.

To produce the central-spot-mode, a second larger spherical grid is required. This grid is also negatively biased to about one quarter of the potential on the central cathode grid. It is characterized by a single bright spot at the center of the cathode. This is not a commonly used mode since the production of neutrons from fusions has been found to be substantially lower than the other modes.

For a symmetric gridded device, the jet mode is initiated in the same manner as the star-mode. The pressure is increased further until the microchannels disappear and only a single bright jet emanating from a very bright central region inside the grid remains. The jet-mode starts at only a slightly higher pressure than star-mode, around 15 millitorr. This means that the star-mode has a very narrow pressure range. The jet-mode can be preferentially induced at an order of magnitude lower pressure by introducing an asymmetry into the cathode grid usually by cutting out one section of the grid wires. This is preferable since the jet-mode propagates from a random grid opening when using a symmetric grid and may switch openings without warning. Using an asymmetric grid allows for complete control in the propagation direction of the jet.

When the jet-mode is first initiated, the jet is tightly focused and has very little space charge spreading over distances of tens of centimeters until it impacts the chamber outer wall. The beam has been found to carry a significant fraction of the overall power supplied to the cathode. In initial tests using a several hundred watt plasma, the beam was directed onto a small molybdenum plate (2 x 3 x 0.1 centimeters) causing it to become red hot. This means the jet must contain a significant fraction of the input power. At higher pressures the jet begins to fan out as the mean free path decreases and the electron scattering increases. This is known as spray-mode, a subcategory of the jet-mode. With a symmetric grid, the jet-mode is lost completely above around 65 millitorr.

2.0 Previous Work

The primary research focus on inertial electrostatic confinement relates to its application for fusion power. Since the jet-mode of operation is not conducive to steady-state fusion experiments in most laboratory setups, it has garnered little attention. One study on jet-mode propagation performed at the University of Illinois by J. Nadler will be presented in this this chapter. The individual components of the experiment such as the helicon plasma source and IEC device have themselves been topics of study for decades. Once again however, there has been little work done on how these two devices interact when coupled together. G. Piefer at the University of Wisconsin – Madison designed and tested a setup to couple these two devices together and the results of this work will be summarized here.

Helicon plasmas themselves have been studied for a number of years and remain a topic of intense research [3] [4] [5]. In recent years, there has even been a focus to use these plasma sources as electric thrusters themselves [6] [7]. M. Reilly studied helicon waves and sources for his Ph.D. dissertation under Professor G. H. Miley [8]. Some of the equipment used in his work has been integrated into the HIIPER Space Propulsion Laboratory device and as such his results are particularly relevant to this work. The goal of the work performed by Reilly was to better understand helicon waves coupling into plasma by providing a 3-d imaging of their propagation. To do this he utilized a custom-built magnetic induction probe, also known as a B-dot probe. Because the quartz tube helicon plasma source and the associated magnet coils were used by Reilly, we can directly consult the results of his work to determine the conditions where the helicon mode propagates. Additionally his calculations of density and temperature proved very useful in calculations performed by G. Chen for his work on the model of the helicon source coupling into the IEC. The results of that work will be summarized in chapter 4.1.

2.1 Helicon Injection into IEC Devices

The most relevant study of helicon plasma injection into IEC devices was performed by G. Piefer for his Ph.D. dissertation at the University of Wisconsin –Madison in 2006 [9]. The focus of the work was not a complete investigation of the coupling in terms of studying various efficiencies and loss mechanisms. The goal was to provide a better ionization source through the metric of ion production rate and efficiency to those traditionally used such as radio frequency inductive or capacitive discharges. Piefer's work is presented as motivation for use of a helicon plasma source to supply the primary ionization for the IEC device. The relevant details of his experiment are provided here as reference.

In the dissertation work, Piefer utilized the IEC star-mode for ^{3}He-^{3}He fusion experiments. In such experiments, because of the high cost of ^{3}He, it is very desirable to run as low of pressure as possible necessitating the use of an ion source to sustain the plasma. Initially constructed capacitive RF and DC discharges could not provide high enough ion fluxes for good fusion rates. To resolve this dilemma, helicon plasma source was built using a quartz tube (52 millimeters ID, 56 millimeters OD, 44 centimeters long) sealed with elastomer gaskets. The helicon antenna was a water-cooled Nagoya III winding constructed from a copper tube with an antenna ID of 58 millimeters and a length of 80 millimeters. He operated this antenna at 2 kilowatts (13.56 megahertz) for steady state and up to 3 kilowatts for short testing. The maximum power was dictated by the ability to keep the elastomer seals and the antenna from melting. The magnetic field was provided by a modified Varian commercial electromagnet pair with a field of up to 2 kilogauss. Piefer also constructed an extraction system for the ions which would minimize neutral gas leakage into the IEC chamber but it was eventually scrapped because it limited the maximum plasma current to a few milliamperes.

The focus of Piefer's work was to provide the highest source of ion current to his IEC device so a measurement of the current was needed. A simple planar probe measurement using a tungsten plate (10 x 10 centimeters) in the path of the plasma source measured the current for a ^{4}He plasma with respect to different plate voltages and magnetic field strengths of the helicon coils. It was found that the maximum ion current extracted from the helicon source was 12 milliamperes. This represented an order of magnitude increase over other ionization source types. Additionally operation IEC device with pressures as low as $1x10^{-3}$ Pascals with a cathode grid current of 1 milliampere became possible.

2.2 Jet Mode Studies

The overwhelming bulk of IEC investigations occur under star-mode conditions. The jet-mode has not received much attention because of the drawbacks to operating for extended periods in this mode, including damage to chamber walls. Because the pressure range of jet-mode is higher than star-mode, it is generally not seen by researchers tuning their chamber pressure to obtain star-mode.

The most targeted study of IEC jet-mode was performed by J. Nadler at the University of Illinois in 1998 [10]. Nadler studied three aspects of the plasma jet. First the current was measured from a variably-biased post inserted in the path of the jet. Second, the measurements were repeated in the presence of a strong external magnetic field. Third, thermal measurements quantified the power in the jet. The apparatus was a small spherical gridded IEC device located at time in the Nuclear Research Laboratory at the University of Illinois. This chamber had a diameter of 30 centimeters and operated in a pressure range of 5 to 60 millitorr. The stainless steel central grid was 6.35 centimeters in diameter with an enlarged hole of 1.9 centimeters to produce the jet-mode.

While operating in jet-mode at 2.2 kilovolts and 20 milliamperes cathode current, post bias voltage was swept from 0 to -100 volts. When the post was grounded a negative current was measured, interpreted electrons in the jet flowing to the ground. A few volts negative bias resulted in zero net current as the electrons do not have the energy overcome the negative potential. With more negative bias, the current goes positive indicating a collection of ions in the jet. The same experiment with the magnetic field yielded a severely reduced ion current. This was explained by the jet having a large electron beam component that when deflected by a magnetic field drastically reduces ionization of the neutral gas. It was estimated the magnetic field resulted in a Larmor radius of 5 to 10 centimeters which corresponded to electron energy in the range of 10 electron-volts.

In order to test the hypothesis that the jet-mode is a substantially different mode of operation, Nadler inserted the biased post into one of the microchannels of a star-mode. In that case there is no crossover point where the current goes to zero at a negative potential. The current was also over two times higher than measured from the jet.

The thermal power measurements involved aiming the jet at a blank vacuum flange and measuring the time rate of change of the temperature increase. This data was used to make a first order estimate of the thermal power of jet. The results indicated that the jet power of the electron beam had approximately 5 to 10% of the total power delivered to the cathode grid.

In his conclusions Nadler suggested that the inclusion of a “drift tube” was needed to allow the ions in exiting the central cathode to drift to the wall without loss of energy. This drift tube essentially consists of a cylindrical grid attached to the central cathode hole. He postulates that the tube would not interfere with the discharge as it only has a small solid angle. Additionally some neutralization measures would be needed to provide electrons into the ion jet to prevent the device from charging. Although the extraction grid technique will not be discussed in this work, the M.S. thesis work of P. Keutelian from the HIIPER Space Propulsion Laboratory showed using COMSOL simulations that such an extraction grid/drift tube system is capable of extracting a significant percentage of the ions from the central grid region [4].

3.0 Experimental Setup

The facilities used in this research are located in HIIPER Space Propulsion Laboratory in room 102 of the Nuclear Engineering Laboratory. The vacuum chamber and several of the power supplies were repurposed from previous IEC fusion experiments however all of the diagnostics and the design of the vacuum system were purpose-built for this research project. A schematic drawing of the overall experimental setup is shown in Figure 3.

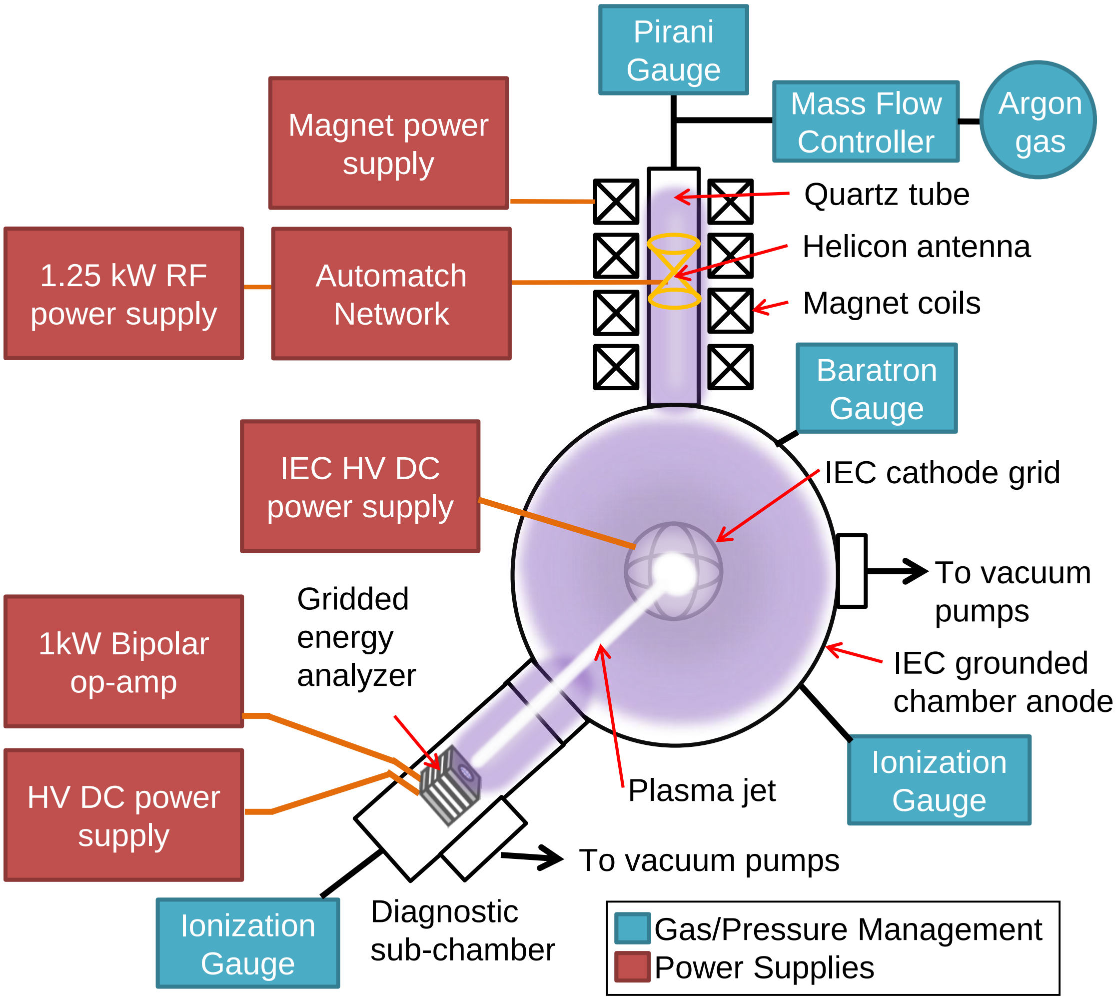

Figure 3. Schematic diagram of the full experimental setup showing the gridded energy analyzer as the mounted diagnostic. All diagnostics are mounted in the same location except for the spherical probe which replaces the IEC grid. Only one diagnostic can be installed at a time.

The IEC chamber consists of a 305 centimeter diameter spherical stainless steel vacuum vessel with a 12.6 centimeter diameter spherical grid mounted on a gimballing high voltage feedthrough that allows for manual in-situ grid alignment. Jet alignment into the installed diagnostic is done by first producing a stable jet at a low to medium power. The current to the diagnostic is monitored continuously using the Labview interface. The grid direction is adjusted using the gimbal while wearing rubber linesman's gloves. Proper alignment is found at the position of largest measured current.

A photograph of the chamber is shown in Figure 4a. This system has a base pressure below 10^{-6} torr (1.3×10^{-4} pascals) and a typical operating pressure of 1.5 millitorr (0.2 pascals) of argon gas. Since the operating pressure is critical to the plasma jet formation, the chamber pressure is monitored by an MKS Baratron capacitive manometer through the Labview interface. Gas is supplied into the helicon tube through an Alicat 5 SCCM (standard cubic centimeters per minute) mass-flow controller with a stable precision of ± 0.001 SCCM. The IEC grid voltage is supplied by a Glassman solid-state high voltage power supply that can operate up to 600 watts with a maximum voltage of 15 kilovolts and a maximum current of 40 milliamperes. Typically the voltage is kept below 10 kilovolts to keep x-ray production low.

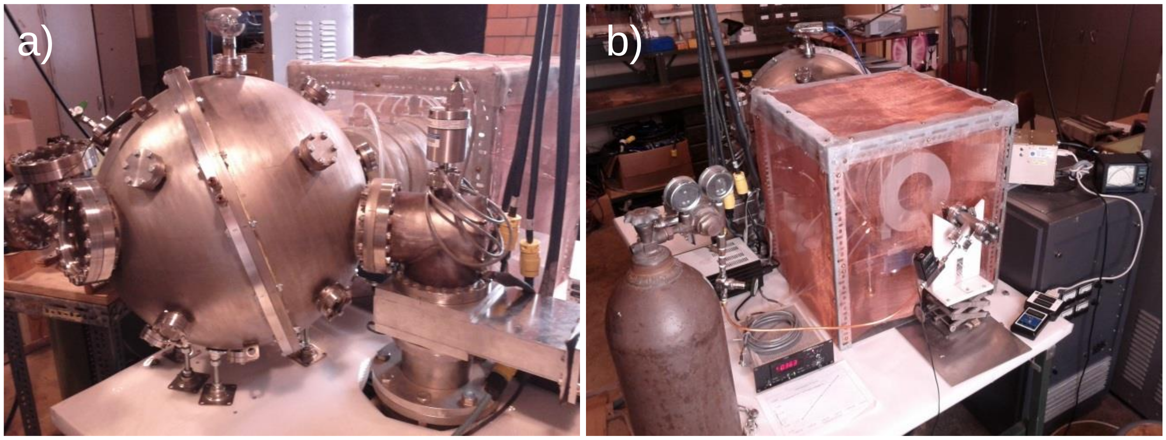

Figure 4. a) Spherical IEC chamber with pump port on the right and GEA diagnostic chamber on the left. The diameter is 61 centimeters (24 inches). b) Helicon plasma source shown inside a Faraday cage.

The helicon plasma source was graciously donated by the Air Force Research Laboratory. It consists of a copper strap m=+1 helical antenna wound around a quartz tube mounted to a 2.75

inch Conflat flange. It is powered by a radio-frequency (RF) power supply running at 13.56 megahertz providing up to 1.25 kilowatts max power connected through a Manitou Systems auto-matching L-network that keeps the reflected power very close to zero. There are four water-cooled magnetic field coils that can supply a field up to 1200 Gauss to propagate the helicon mode. Figure 4b shows the source mounted inside a Faraday cage.

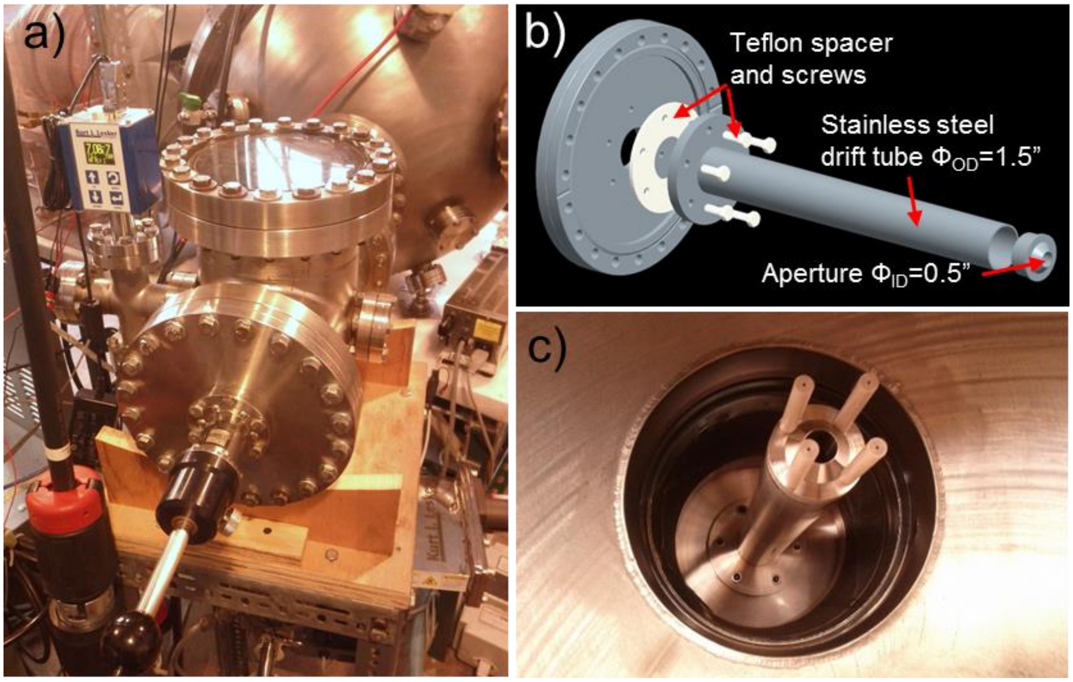

Figure 5. a) Diagnostic sub-chamber showing the linear motion feedthrough used to mount the gridded energy analyzer and Faraday cup. b) 3-d model of the 12 inch long drift tube plasma aperture. c) The drift tube aperture photographed from the main chamber leading to the diagnostic sub-chamber. The PEEK pegs shown around the aperture can be used to mount various electric extraction grids.

Attached to one of the 8 inch Conflat ports of the IEC chamber is the diagnostic sub-chamber shown in Figure 5a. The sub-chamber is constructed from a 6-way cross and is mounted on a separate stand so that it can be wheeled away when the IEC chamber is opened. It can be differentially pumped using a separate turbomolecular pumping system to achieve a pressure 40 times lower pressure than the main chamber which allows it to reach an even lower base pressure below 7 x 10^{-7} Torr (9.3 x 10^{-5} pascals). In order to achieve this pressure differential, a drift tube plasma aperture is required. It is a 12 inch long stainless steel tube with a 0.50 inch aperture facing the inside of the IEC chamber. It is electrically isolated from the grounded chamber using a Teflon spacer and screws thus allowing it to be independently biased or floating potential. Although constructed during the course of this work, the drift tube was not used for all results presented in this dissertation so that the diagnostics could be mounted closer to the IEC cathode grid. This meant that the plasma aperture was only the 8 inch Conflat zero-depth reducer flange shown in Figure 5b. The aperture used for all experiments was then 1.37 inches (3.48 centimeters) however this opening was large enough that no differential pressure existed between the diagnostic and IEC chambers. There are several electrical feedthroughs mounted on the 6-way cross providing for all connections to the internal diagnostics. Each diagnostic used in this work (with the exception of the spherical probe) was installed in this sub-chamber and changing them required venting the chamber and disassembling the old diagnostic.

4.0 Spherical Plasma Probe

In order to understand how the helicon plasma source affects the power and mass balance of the coupled system, the total current to the grid was provided using a spherical plasma probe. The probe is a hollow stainless steel ball of the approximate diameter of the central cathode grid. It replaces the grid on the high voltage feedthrough and is biased negative to draw ion saturation current from the helicon source generated plasma accelerating toward the IEC cathode grid. A photograph of the probe is shown in Figure 6. This method is similar to that used by Piefer in testing his helicon plasma source coupling with the IEC device. There are two major differences between his work and that performed for this dissertation. Piefer used a planar probe however spherical probe geometry used in this work better simulates the actual shape of the electrostatic potential of the cathode grid. Additionally Piefer applied voltages more than an order of magnitude greater than this work since very high energies are required to achieve significant cross sections and reaction rates in ^{3}He-^{3}He fusion. The potentials used on the probe in this work reflected the potentials commonly place on the cathode grid for exciting the jet-mode, up to 10 kilovolts.

Figure 6. Photograph of the spherical plasma probe mounted in place of the cathode grid. The small black spot on the bottom is a hole drilled to eliminate virtual leaks from the probe.

4.1 Summary of Plasma Probe Results

The plasma probe experiments were performed in collaboration with G. Chen and analyzed in his M.S. thesis [11]. A summary of Chen's work is provided in this section. The goal was to explore the coupling of the helicon plasma source to the IEC grid. He found a number of parameters that eventually allowed a calculation of the efficiency in coupling the helicon plasma source to the IEC device, defined as the fraction of power transferred into the IEC device from the helicon plasma source. Chen also analyzed loss mechanisms and identified inefficiencies. The results of that work are summarized in this chapter.

The data collected were the form of current measurements from the spherical probe for different settings of bias and plasma conditions. Since the bias voltage on the probe went as high as -5000 volts, Chen compensated for secondary electron emission from the probe due to high energy ion impacts. A primary assumption of the work is that ions born in the helicon plasma source will fall into the large negative potential of the spherical probe and cause a current to be measured by the current sensor. This assumption was first studied using a COMSOL model to determine the penetration of the electric field into the quartz helicon tube. The results showed a small, approximately linear potential drop of 20 volts across the quartz tube for a potential of -5000 volts on the probe.

In order to calculate the theoretical plasma properties inside the helicon plasma source, Chen created a one dimensional rate equation computational model. The electron temperature and ionization fraction were calculated for different pressures and RF powers. Additionally, the model provided a mechanism to find the power loss terms associated with electron-neutral scattering as well as impact excitation and wall collisions. He applied this model to the parameters typically used to run the IEC device in jet-mode. Using ionization fraction data provided by Reilly's Ph.D. dissertation, it was found that the approximate electron temperature inside the helicon plasma source was 3.7 electron-volts. Additionally Chen calculated that only about 15% of the input RF power goes into the ionization of argon neutral atoms at the specified conditions.

In measuring the coupling of the ions produced in the plasma source to the IEC, Chen discovered that at a bias voltage of -1000 volts, the probe only achieved a 4% efficiency in power collection as defined by the ratio of the collected probe power to the helicon input power. The result was roughly the same for all plasma parameters calculated for the narrow range in which the jet-mode can exist although decreasing somewhat for increasing RF power. Although it was initially expected that the high negative electric potentials on the probe would result in ion saturation, that did not seem to be the case.

Chen concluded by stating that the primary energy loss mechanism inside the helicon plasma source was electron excitation collisions accounting for around 54% of the power loss. However, for the helicon source itself he found a large fraction of 46% of the total input power was going into ion production. It is clear though, that more research is required to development mechanisms to get more of these ions into the main IEC chamber. One possible solution is to create a stouter helicon tube. This would allow the central potential from the IEC grid to reach a larger fraction of the ions created in the helicon source.

4.2 Calibration of Spherical Probe Current Sensor

One challenge that arose when designing the spherical probe experiment was the accurate measurement of the current delivered to the probe while it was biased at high voltage with respect to ground. Normally this would be performed by measurement of an analog output current measurement terminal on the power supply itself or through the use of a small resistor and a high voltage differential probe. Lacking both of these options, a different approach was used. A current sensor was constructed based on a sensitive Hall Effect device with a capability to be used with a large common mode voltage yet still have good sensitivity for measurement of low currents in the milliampere range. Physically, the current sensor is an external box containing the commercial Hall Effect current sensor, a model CS0.25A-02 from GMW Associates which connects to the IEC electrical feedthrough attached to the spherical probe. The sensor itself operates by sensing the DC magnetic field produced by current flowing in small internal loop of wire. The listed specifications for uni-polar operation are shown in Table 1.

Range	0 – 250 mA
Output	0 – 5 VDC
Sensitivity	20 V/A
Resolution	± 0.1 mA
Primary Resistance	6 Ω
Primary to Secondary Voltage Isolation	4 kV

Table 1. Manufacturer specifications for CS0.25A-02 Ametes High Sensitivity Current Sensor.

This model of current sensor was selected because of its high sensitivity to low DC currents, its high voltage isolation, and low cost of $25 per device. The listed voltage isolation is conservative as with any manufacturer specification and through experience it was found that the sensor can operate up to 6.5 kilovolts without fail. However it is sensitive to rapid changes in voltage and the sudden loss of plasma in the chamber, which causes a voltage spike in the power supply, typically destroys the sensor. An operating procedure to prevent this situation was implemented after the loss of two sensors which involved starting the RF plasma at higher than normal pressure with a magnetic field, then backing down the pressure to the desired operating level. Also very low pressure operation was avoided because of the instability of the plasma.

The current sensor was calibrated using a precision current source provided by a Keithley 2401 Sourcemeter. The high voltage cabling that connects the IEC power supply transformer to the feedthrough was disconnected and the current was sourced through this cable and the sensor using a 1.0 ohm resistor. The current was stepped in increments of 1.000 ± 0.001 milliampere. The calibration plot is shown in Figure 7.

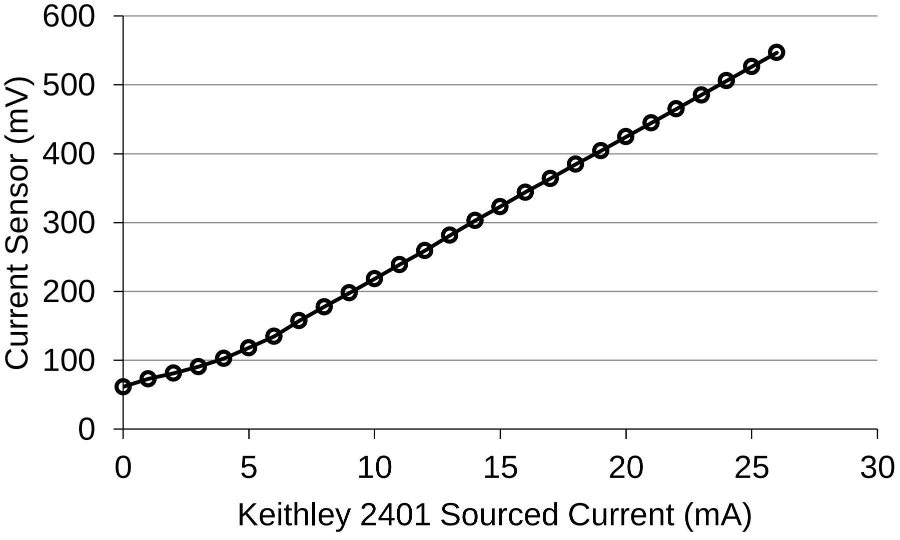

Figure 7. Calibration curve for spherical probe current sensor.

By inspection of Figure 7, the current sensor does not reach a linear slope until after 5 mA of sourced current. After 5 milliampere, the slope is 20.52 volts/ampere which is slightly above the manufacturer specification of 20 volt/ampere. Below 5 milliamperes, the slope can be fit using a third order polynomial. Although the current source was not able to go above 27 milliamperes, a linear trend is quite evident and provides confidence that the sensor voltage output will remain linear in the region of interest, up to 50 milliamperes or 1/5 of its rated maximum current. The calibration from sensor output voltage back to probe current (by reversing the axes of Figure 7) shown in (1) has been directly implemented into the Labview VI utilizing an if-statement. The variable V_{Ametes} is the measured voltage from the sensor.

$$I_{measured}\ [A] = \begin{cases} -17820 \times V_{Ametes}^3 + 4319.7 \times V_{Ametes}^2 - 241.96 \times V_{Ametes} + 2.663, & V_{Ametes} \leq 0.1182\ [V] \\ 48.71 \times V_{Ametes} - 0.6726, & V_{Ametes} > 0.1182\ [V] \end{cases} \quad (1)$$

5.0 Faraday Cup

A Faraday cup is a simple diagnostic used to measure the beam current in a plasma device. The two different circuit configurations are shown in Figure 8. In the biased configuration, a power supply bias is applied to the cup and an electrometer makes voltage measurements. This is the most commonly used configuration for the cup and has an advantage over the grounded configuration in that it can be used to measure ion beam current by setting the bias supply so that the cup is strongly negatively biased to reject all plasma electrons. The electrometer has a very high input impedance, typically greater than 10^{14} ohms such that it draws essentially no current making for highly accurate measurements. Since the high impedance electrometer is a requirement to run in biased configuration and this instrument was not available, the grounded configuration was used instead. This allows for a measurement of the total beam current in the jet-mode. It will be shown in the later results section that the electrons represent the largest contributor to the power in the plasma jet.

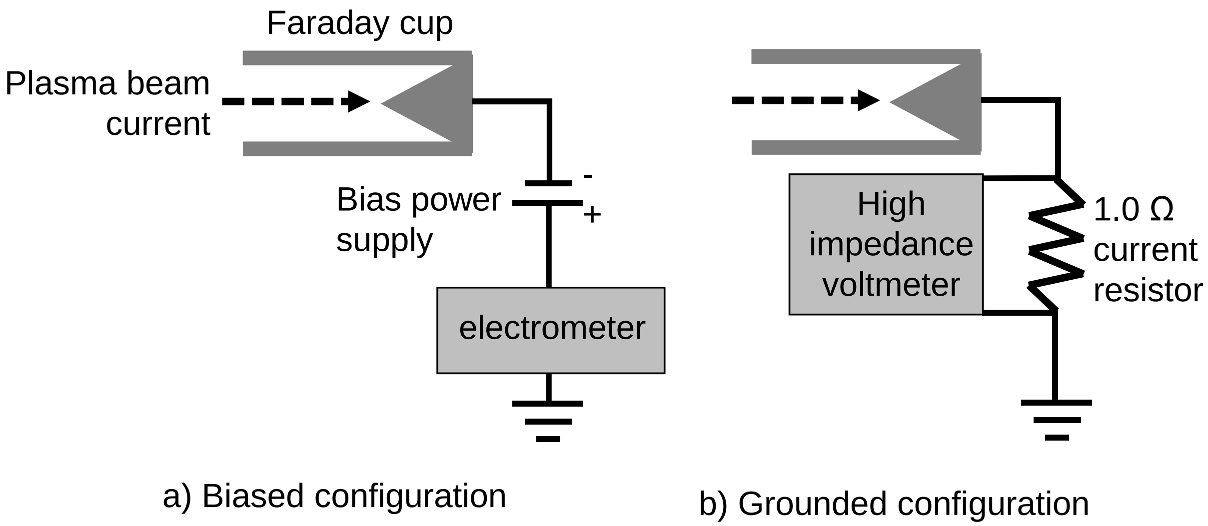

Figure 8. The Faraday cup can operate in two configurations. a) Biased configuration can probe the ion current using a large negative potential. B) Grounded configuration was used for all measurements in this dissertation and can collect the total beam current.

5.1 Construction

The Faraday cup was designed to be robust in order to handle large heat fluxes without any internal cooling mechanism since the diagnostic sub-chamber has no fluid feedthroughs for cooling liquids. Instead, a platinum resistance temperature detector (RTD) was attached to the central plate of cup to monitor the heat build-up. This RTD has the added benefit of allowing measurement of the thermal power as described later in the results chapter. The multi-stack insulation design was inspired by a smaller Faraday cup originally located inside the Spherical Electrostatic Analyzer donated by the Air Force Research Laboratory. Whereas that cup was small and designed to only handle a few watts of power, this design is scaled up and is capable of handling a few hundred watts of thermal power over short time frames. The plasma-facing components are 304 stainless steel while the support plates are made from aluminum and electrically isolated and mechanically separated by alumina ceramic spacers. The inner cup aperture has an inner diameter of 0.875 inches, approximately large enough to capture the entire visible diameter of the plasma jet. The stacked plate design means that inner cup, which fastens to the central aluminum support plate can maintain a high potential separate from ground. A wire connects to the underside of the central plate leading to the high voltage feedthrough which then bolts the cup to the linear motion feedthrough. Conduction through the electrical feedthrough bolts ensure that the top and bottom plates and the outer shield are maintained at ground potential. Normally the cup is mounted to a stainless steel threaded rod to allow it to be placed closer to the IEC cathode grid. It is shown mounted in this configuration in Figure 9d.

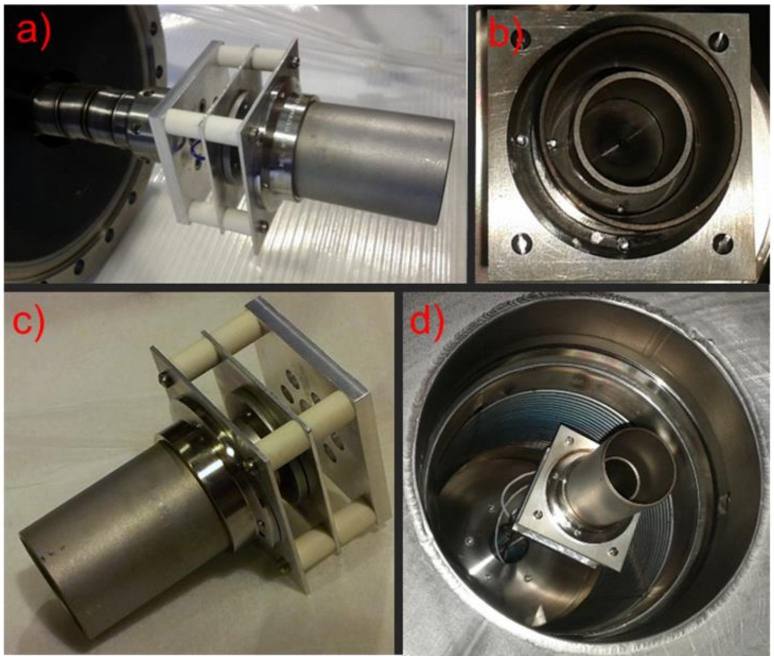

Figure 9. Photographs of the Faraday cup showing the key features: a) mounted on linear motion feedthrough. b) Double cupped structure and conical insert. c) High electrical isolation provided by large ceramic spacers. d) Mounted inside diagnostic sub-chamber.

5.2 Thermal Power Calibration

The Faraday cup can provide a useful estimate of the jet-mode thermal power by using the RTD mounted on the underside of the inner cup. To obtain the thermal power the slope of the temperature verses time data was correlated to jet power using a COMSOL simulation. The simulation was tuned by fitting it to experimental data using a cooling curve (a zero incident heat flux condition) produced by letting the system thermally equilibrate to room temperature from a high starting temperature of around 94 °C. The geometry of the simulation was produced using actual Faraday cup dimensions and the material properties were matched. The simulated geometry is shown in Figure 10. The highlighted (blue) surface shows the boundary condition of thermal heat flux. Conduction and convection are not an issue for a majority of the geometry because of the low pressure, however one set of surfaces was set to a conduction boundary condition to simulate the physical connection point of the Faraday cup to the threaded stainless steel rod that connects to the linear motion feedthrough. The remaining surfaces are set as radiative boundaries.

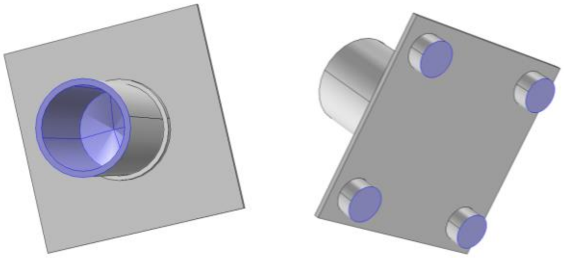

Figure 10. (left) Simulated geometry used in the thermal model COMSOL Faraday cup calibration curve showing the thermal flux boundary condition in blue. (right) The conduction boundary condition on the bottom is shown in blue.

The parameters needed by the simulation are k and epsilon, the thermal conductivity and the thermal emissivity respectively. In order to find a reasonable fit to the experimental data, an iterative trial and error approach was used after setting to the material properties to initial values provided by COMSOL as shown in Figure 11.

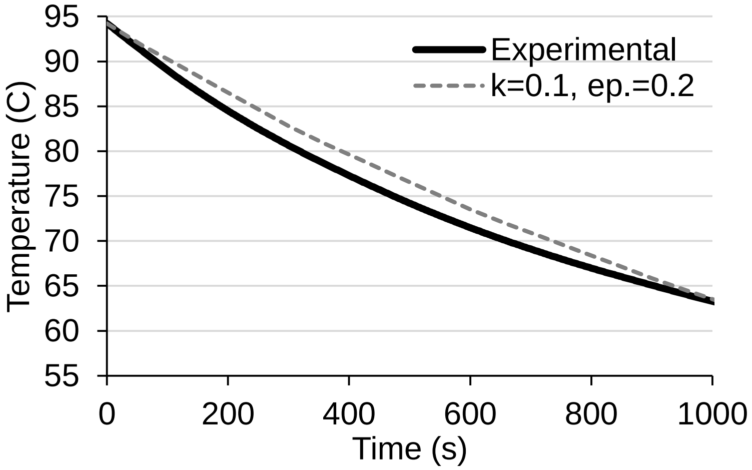

Figure 11. The experimental cooling curve that was used to find the parameters for k and epsilon in COMSOL. The dashed line represents the parameters used in the simulation.

After obtaining the k and epsilon parameters, the thermal flux boundary condition was enabled and the temperature slope was found for each thermal flux condition. The calibration curve was then constructed using the results from input thermal powers. Originally plotted with the ordinate at the thermal power and the abscissa as the thermal slope, the axes are reversed to make the thermal slope the independent variable such that now we need only multiply the thermal slope by 183.6 to find the thermal power.

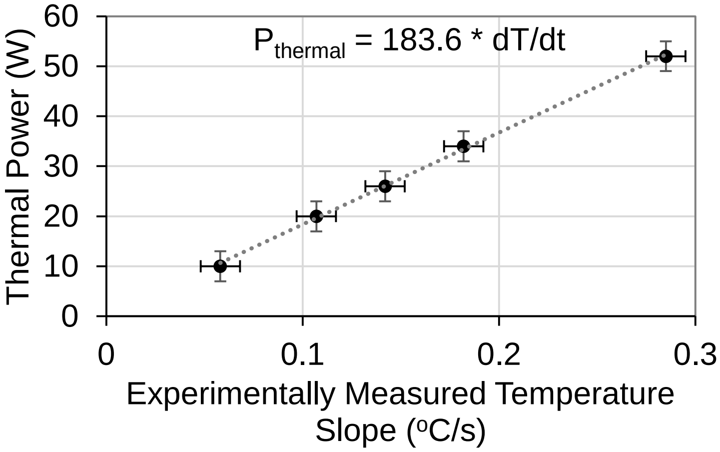

Figure 12. Thermal power calibration curve for the Faraday cup RTD sensor. The error bars are indicative of the uncertainty in the model fit to the experimental data, as well as the difficulty in choosing the proper range for the slope for each set of experimental conditions.

6.0 Gridded Energy Analyzer

The gridded energy analyzer (GEA), also known as a retarding potential analyzer, is a diagnostic tool that can be used to determine the ion and electron temperature distribution of a plasma beam [12] [13]. The GEA is essentially a more advanced version of the biased Faraday cup. It produces a current measurement as a function of a number of independently biased grids. It can operate in two different modes corresponding to the two different charged plasma species. The GEA is similar to the biased Faraday cup in that both are current-integrated devices. For the GEA, this means that any particle that does not have sufficient energy to overcome the potential of the sweeping grid is rejected. As an example of operation in ion mode consider a biased grid is set to a potential of V and is approached by singly-charged ion with energy E_0. If the $E_0 > eV$, the ion will pass the grid and be collected otherwise it will be turned back. The mathematical relation for the total current collected at a given energy is then

$$I(E) \propto \int_{E_0}^{\infty} I(E)dE, \tag{2}$$

Contrasted to a diagnostic such as the spherical electrostatic analyzer where

$$I(E) \propto |I(E)|_{E_0}, \tag{3}$$

the GEA appears to have a major drawback. However, the GEA is a much simpler device to construct and a reasonable energy spectrum of the ions and electrons can still be obtained.

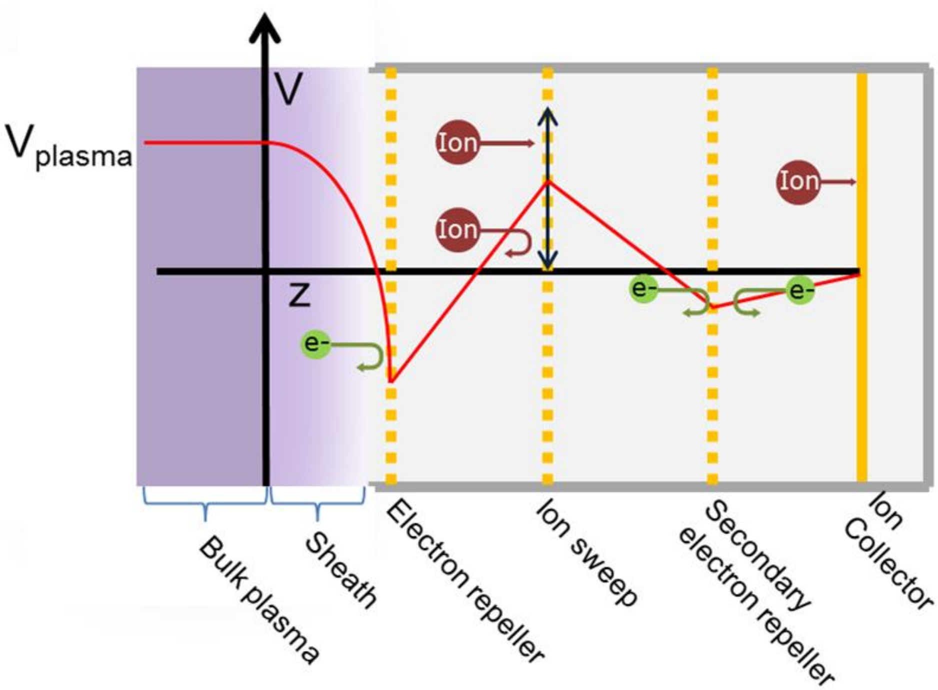

Figure 13. Illustration of electrical potentials on various grids in the GEA operating in ion mode. The floating aperture is not shown however would be placed in front of the electron repeller.

When operating in ion mode, the GEA consists of three electrically biased grids, a grounded collection plate and a floating aperture that limits the total current into the device as shown in Figure 13. The first grid is called the electron repeller and is strongly negatively biased to repel all of the plasma electrons. The second grid is the called the ion sweep grid and has the function of selecting the ion energy as in the above example. The third grid, called the secondary electron repeller, is slightly negatively biased with respect to the ion collector plate to repel secondary electrons created from collisions back to the plate. In general the ion collector plate can be biased negative to give the ions a small boost in energy before collector, but for electrical simplicity for the collection circuit, we have chosen to ground the plate. Similar to the Faraday cup, the GEA can also collect the total plasma current. To do this, the ion sweep grid is grounded. The electron repeller grid can then be swept to recover the electron spectra since as will be demonstrated later, the jet consists primarily of high energy electrons.

In order to find the energy spectrum, we need to differentiate the current verses voltage curve. Because of the noise present in any data acquisition scheme, this curve must be smoothed before a derivative can be taken or else the derivative produces only useless noise. The smoothing method chosen in this work was based on a Least-Squares polynomial fit to the data at each point using software called Stata. It is described in further detail in chapter 8.3.2.2. For many laboratory plasmas where thermal equilibrium is a fair assumption, it is possible to fit a Maxwell-Boltzmann distribution and calculate the ion temperature. However, because the shape of the distributions for these IEC plasmas are very non-Maxwellian fitting a value of ion or electron temperature does not make sense [14]. Instead it will demonstrated that the electron spectra show a sharply peaked distribution at high energy and a smaller secondary peak at much lower energy. The ion spectra was not measured in this work.

It is possible to get the shape of an ion or electron distribution directly without making any assumptions about its shape and without needed to do any smoothing to take the derivative. To do this requires the direct calculation of the derivative of the I-V function as it is being collected. This method is detailed in a 1958 paper by L.B. Leder [15]. He applied a small alternating voltage on top of the sweep voltage as shown in Figure 14. By making this AC signal sufficiently small and at a frequency sufficiently higher than the sweep grid frequency, the slope of the I-V curve can be directly calculated using the peak-to-peak value of the current fluctuation. In his work, Leder found that operating the AC signal at 1.0 kilohertz was adequate. This means the sweep voltage can be operated at tens of hertz for efficient data collection. This method of course will cause a fluctuation in the electron energy which depends on the amplitude of the AC signal. However for measurement of the jet mode electron current it would not present a problem since a few volt AC signal will not be noticeable to electrons with energies of hundreds of electron-volts.

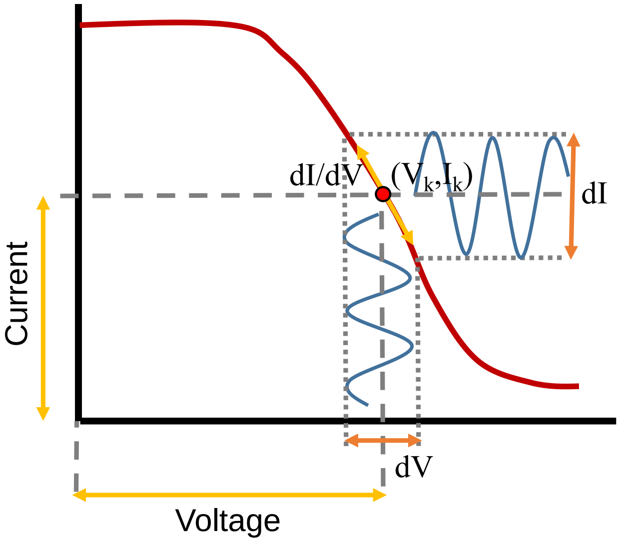

Figure 14. The derivative of the I-V curve can be extracted directly by using a small AC voltage signal on the sweep grid during the main voltage sweep. At each point (V_k,I_k) the peak-to-peak value dV and dI can be measured directly and thus dI/dV can be easily calculated.

6.1 Construction of Gridded Energy Analyzer

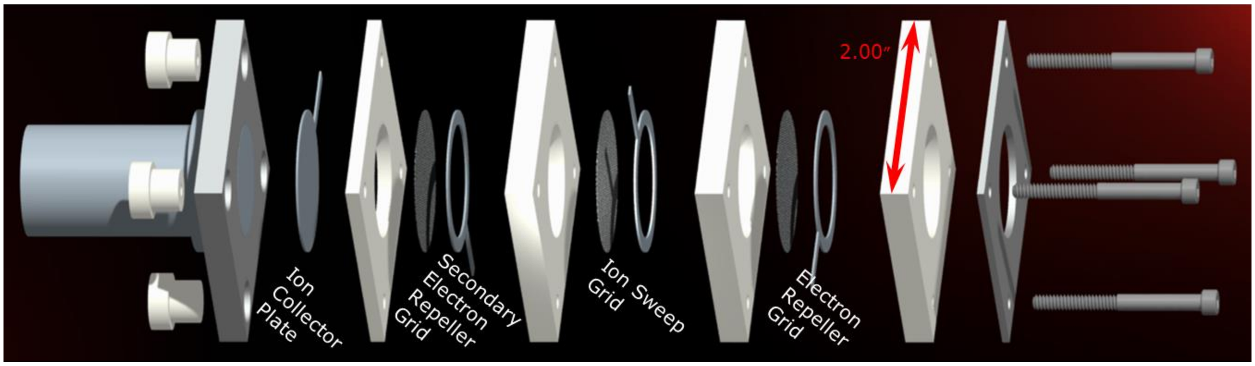

Figure 15. Exploded 3-D model of gridded energy analyzer showing the three biased grids and grounded ion collector plate. The plate at the front of the device on the right side is a nickel floating potential aperture.

A three dimensional exploded model of the GEA is showed in Figure 15. This is the second generation of the gridded energy analyzer built for this work. The first GEA suffered a catastrophic failure due to arcing between the electron repeller and ion sweep grids caused by a crack in the alumina ceramic insulation. This second design uses thicker Macor ceramic insulation chosen for its higher dielectric strength and significantly better machinability compared to alumina. The grid wires are 20 mesh tungsten gauze from Alfa Aesar with wire of diameter 0.004 inches. The wires need to be thin so they do not block too much of the jet and decrease the signal but at the same time they need to be robust enough not to melt under the heat load. This mesh size and wire size were a compromise between these two requirements and give a per grid transparency of 92.2%. A titanium ring electrode compresses each grid onto the Macor plates. This ring provides electrical contact through copper toothless alligator clips. The dimension of the center aperture is 1.00 inch with the plates themselves 2.00 inches on each side. All parts were machined to high tolerance so that the grids would have precise alignment. Four Teflon plugs act as insulating nuts for the screws holding the structure together. A temperature sensing RTD was connected to the underside of the aluminum structure although it unfortunately failed and provided no useful data for this work.

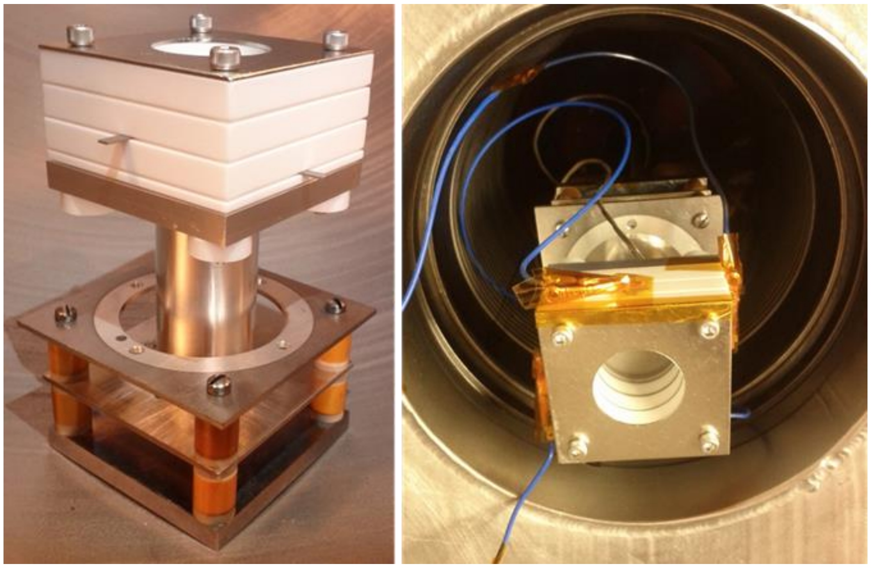

Figure 16. (Left) Photograph of the assembled GEA using the same base to connect to the linear motion feedthrough as the Faraday cup. (Right) GEA installed in the chamber at the 0 centimeter position where the aperture is at approximately the position of the chamber anode surface. This represents the maximum extension into the chamber possible without modification to the linear motion feedthrough.

A photograph of the completed GEA installed in the chamber is shown in Figure 16. The left photo shows the mechanical structure that holds the GEA to the linear motion feedthrough. The design utilizes the same three plate structure as the Faraday cup to ensure electrical isolation between the bottom ground plate, which is screwed onto the feedthrough, and the middle plate where the GEA is attached. A generous amount of Kapton tape was used to protect the electrical connections from any sputtering by the jet as well as sputtered material from the grid. The metal sputtered from the grid can cause electrical shorts if care is not taken. To minimize this effect, plasma facing ceramics were coated in Kapton tape and this tape is replaced each time the chamber was opened. However it was not possible to use Kapton on the interior surfaces of the GEA and as will be shown later, metal deposition ultimately led to the failure of the diagnostic. Removing the metal from these surfaces is required before it can be operated again.

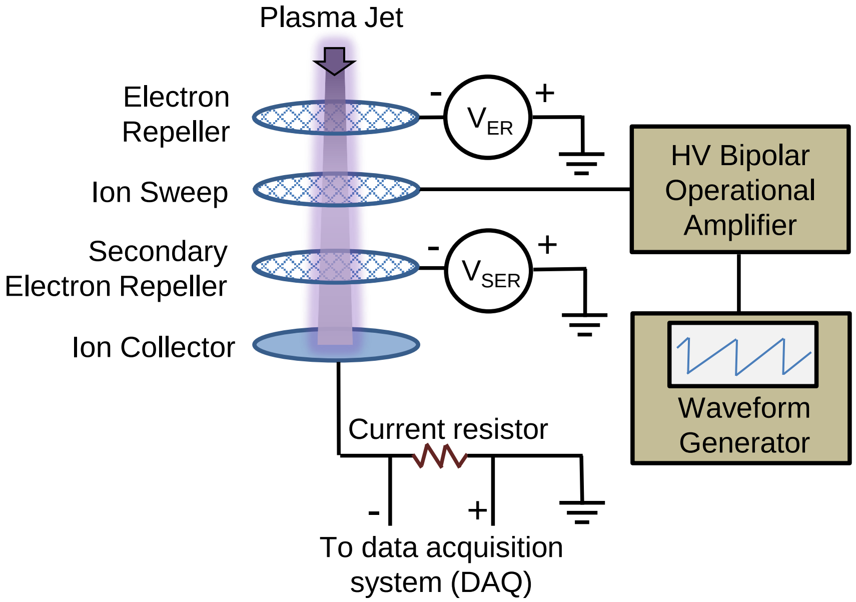

Figure 17. Electrical schematic diagram of the gridded energy analyzer (GEA). The two repeller grids are biased negatively to repel plasma and secondary electrons. The ion sweep grid is biased positively to only allow ions with energies above the sweep voltage threshold.

An electrical connection diagram for the GEA is shown in Figure 17. Note that this setup does not apply the small AC signal to the ion sweep grid. The power supplies V_{ER} and V_{SER} correspond to the electron repeller and secondary electron repeller grids respectively are biased negative with respect to the grounded ion collector plate. The electron repeller grid V_{ER}, is provided by a Hipotronics Model 8100-25 high voltage DC power supply capable of supplying up to 25 milli amperes and up to 100 kilovolts. This fully analog power supply was repurposed from its original use at driving IEC grids for fusion experiments. The voltage was monitored by a high voltage probe which fed into the DAQ. Although data on the current supplied by the electron repeller was not used, it was sometimes monitored using the Ametes current sensor originally built for the spherical probe experiment. However, it was found that under typical jet-mode conditions the sensor had inadequate sensitivity to be useful. The secondary electron repeller grid V_{ER}, was provided using a series of five 9-volt batteries to create a 45 volt potential. Batteries were chosen because a precise voltage was not needed and the current draw would be very low. The choice also keeps the option open of easily biasing the secondary electron repeller with respect to a biased collector plate instead of with respect to ground. A sawtooth voltage ramp is applied to the ion sweep grid using an Agilent model 33220A arbitrary waveform generator fed into a Kepco BOP-1000M bipolar operational amplifier to boost the signal by 100 times. This equipment pairing can provide a 0 to 1000 volt ramp. Because of the slow data collection speed of the data acquisition system, the ramp was performed at only 10 millihertz. This was referred to as a slow sweep. A fast sweep of 10 hertz was originally planned but untenable when it was discovered that the oscilloscope picked up too much noise to provide a useful waveform trace. Similar to the Faraday cup in bias configuration, the GEA can run the ion collector grid with negative bias voltage to enhance the ion signal. In order to do this, an isolation amplifier circuit can be used to isolate high common mode voltage from the oscilloscope or the DAQ.

The isolation amplifier circuit was design and tested on a proto-board but ultimately never able to be used since it suffered a failure of one of the integrated circuits during final construction. It is essentially a poor-man's high-voltage differential amplifier. This circuit was designed around the Burr-Brown ISO121 precision isolation amplifier [16]. The iso-amp is fed from an instrumentation amplifier and can provide continuous operation with a common mode rejection (CMR) of 160 decibels at up to 5000 VDC isolation from ground [17]. The gain is normally unity but can be set using (4). If a larger voltage isolation is desired, some sacrifice in gain is required since the max gain of the INA110 is 500x. It should be possible however to use another instrumentation amplifier to boost the signal back again after the iso-amp or to replace the INA110 with a higher gain chip.

$$Overall\ Gain = \frac{R_2}{R_1 + R_2} \times Gain_{INA110} \tag{4}$$

Power to the instrumentation amplifier and high-voltage side of the isolation amplifier is provided via battery source providing ±15 volts DC (V_{S1}). The low-voltage side of the iso-amp also needs ±15 volts DC (V_{S2}) but can be supplied by a standard laboratory power supply.

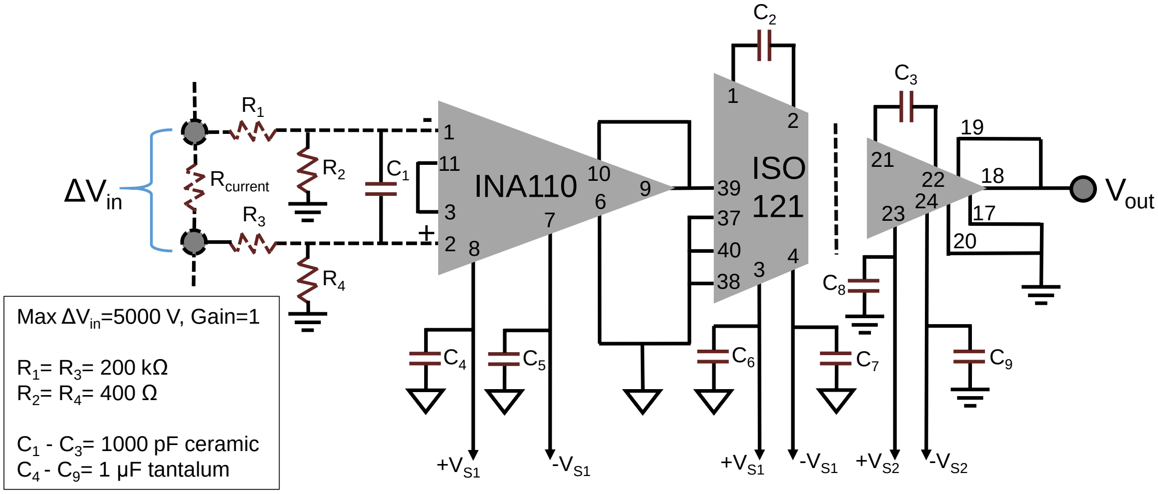

Figure 18. Circuit diagram of custom built high voltage differential amplifier using two integrated circuits, an instrumentation amplifier and an isolation amplifier. With the component parameters listed the circuit provides a max common mode rejection of 5000 volts with a gain of unity.

7.0 Piezoelectric Force Sensor

The piezoelectric force sensor was constructed based on a design by Chavers and Chang-Díaz [18] and later expanded upon by Longmier et. al. [19] [20]. The traditional method to measure force by electric propulsion devices is the thrust stand, i.e. a movable table mounted inside a very large vacuum vessel. This was completely impractical and ultimately unavailable to us. The piezoelectric design was then chosen because of its practicality in making in-situ force measurements.

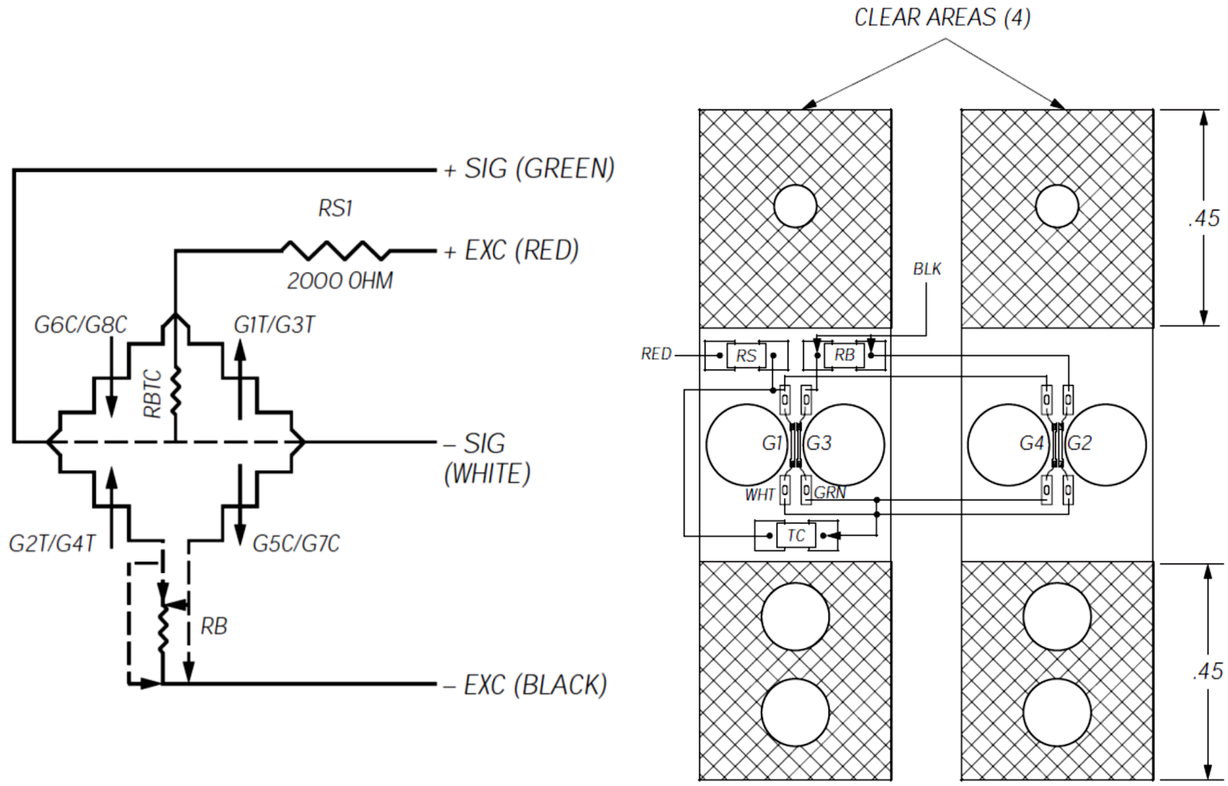

Figure 19. The manufacturer-supplied specification diagram shows the circuit configuration (left) and the physical sensor mounting position on the stress concentrator (right). The isthmus where the sensors are mounted is only 0.70 millimeters wide.

The design uses a large plasma target plate connected by an electrically insulated ceramic lever arm to a stress concentrator on which the piezoelectric sensors are mounted. The sensors themselves are configured in a Wheatstone bridge configuration shown in the original specification sheet in Figure 19. The piezoelectric sensors are excited by a 5.000 volt DC source (+EXC and –

EXC) and the voltage is measured at the other end of the bridge as a very small signal (+SIG and –SIG), on the order of millivolts. The circuit also has temperature compensating resistors (RS and RB) such that the change in signal as a result of plasma heating of the diagnostic does not affect the measurement.

7.1 Construction

The piezoelectric sensor gages are Micron Instruments model SS-09-060-1150P. They are very small, just 2.3 mm long and 0.2 mm wide and attach to a titanium stress concentrator which was machined by the author to a hole-alignment tolerance of 0.001 inches. After receiving the plate, Micron Instruments performed the installation and testing of the gages. The remainder of the diagnostic including the aluminum mounts and the titanium target plate was machined in the MRL machine shop by the author.

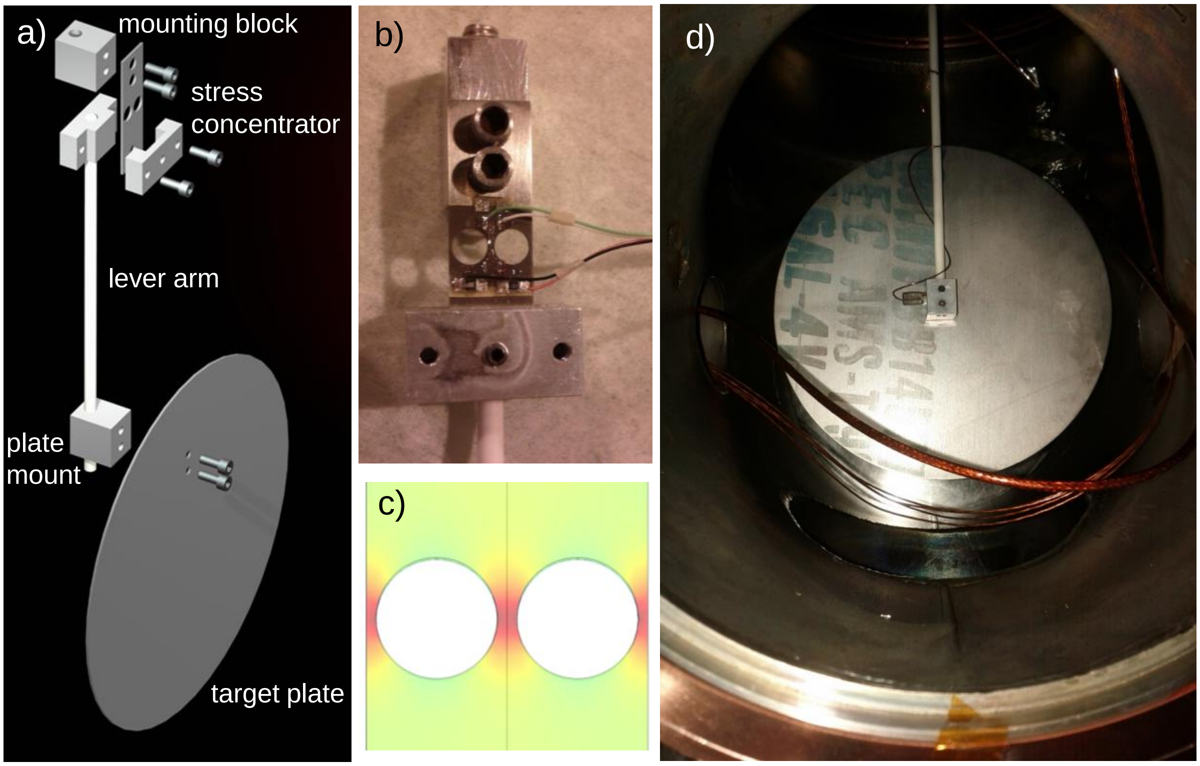

Figure 20. a) An exploded 3-d model of the piezoelectric plasma force sensor. The sensors themselves are attached to the rectangular stress concentrator. The plasma strikes the large circular target plate (12 centimeter diameter). b) A zoomed photograph on the stress concentrator with mounted sensors. c) A COMSOL simulation of the volumetric strain demonstrating the

efficacy of the stress concentrator. d) The sensor mounted in the diagnostic sub-chamber. This backside photo shows the thin and flexible grounding wire attached to the plate mount.

7.2 Calibration

The calibration procedure used by Chavers relied on a set of masses hung from a light string [18]. This method is very simple however a different calibration procedure was chosen based on a combination of physical measurement and COMSOL simulation. The decision was based on a few factors. The sensor was designed to be much more sensitive than the Longmier design because of the increased lever arm and higher-stress concentration plate. The precision in calibration for small masses was deemed to be not high enough considering the goal of being able to measure in the sub-millinewton force range.

The two-step calibration procedure involved first creating a calibration curve of sensor output as a function of plate deflection. An apparatus was machined to mount the entire force plate. A very small, precise deflection was applied to the center of the circular target plate using a micron screw. This produced a fairly linear sensor response as a function of displacement from equilibrium. The displacement-voltage curve was created by A. Krishnamurty during her M.S. thesis work in the HIIPER Space Propulsion Laboratory [21]. A COMSOL simulation was then created based on an accurately dimensioned 3-d model of the sensor. Various forces were applied to the plate in the same location as the micron screw and after several simulations, the displacement of the plate as a function of incident force was plotted. Lastly the two curves were combined to eliminate sensor displacement, leaving only the sensor output as a function of force. The calibration graph is shown in Figure 23.

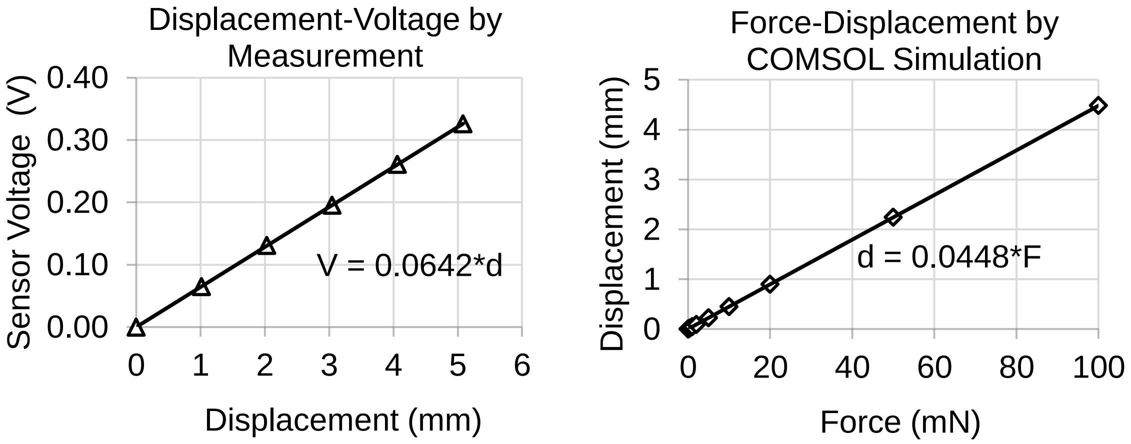

Figure 21. (left) The displacement-voltage relation was measured using a micron screw to push on the force plate. (right) The displacement-force relationship was created using a COMSOL simulation.

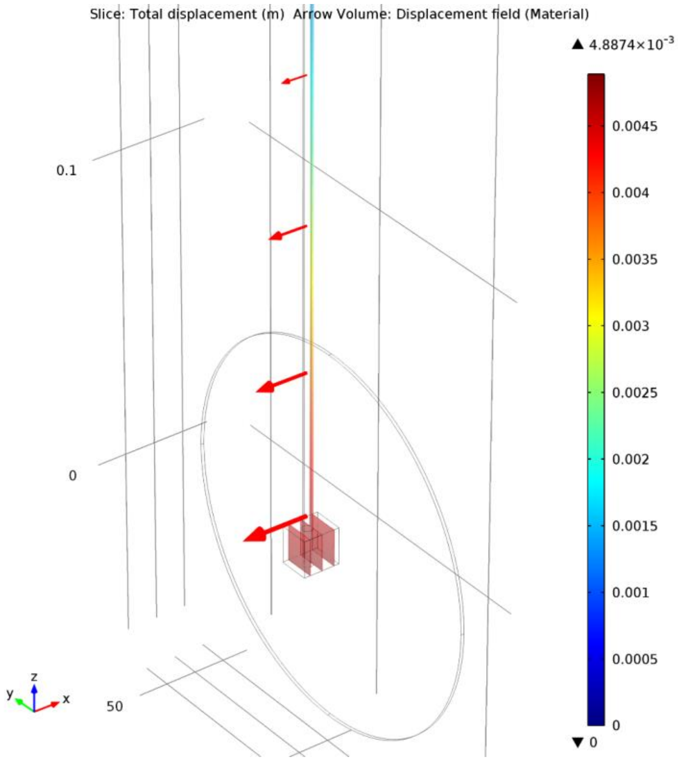

Figure 22. A series of COMSOL simulations were used to find the force-displacement relationship for the force sensor. The displacement field is shown for a 100 milliNewton force in the –x direction. The maximum displacement (in red) of the plate mount can be read directly from the maximum of the scale bar (in units of meters), e.g. 4.88×10^{-3} meters.

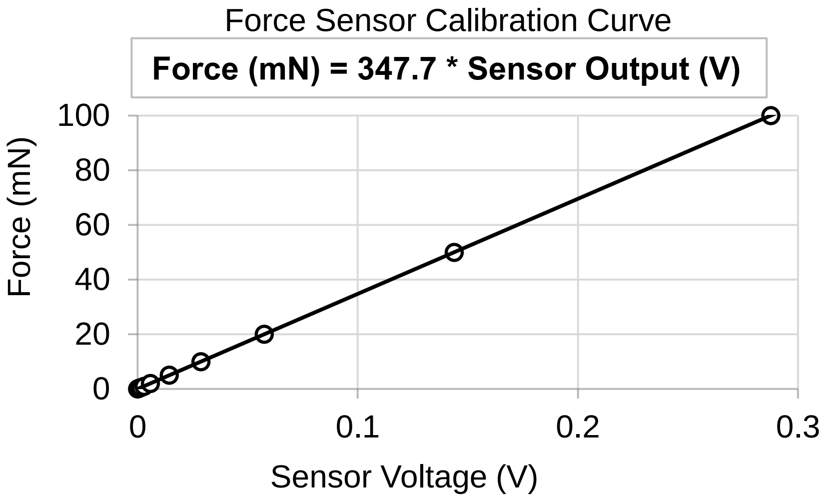

Figure 23. The force sensor calibration curve was produced from a combination of the graphs in Figure 21.

8.0 Results

The results of the experimental work to study the inertial electrostatic confinement jet-mode are presented in this section in three categories. First, the operational limits of the IEC jet-mode are given for this device. It is demonstrated that the use of RF power allows for an additional control of the conditions verses running the jet mode only with an IEC glow discharge. The second category of results shows two types of efficiency in the IEC device operation. The total efficiency is defined simply as the ratio of the total jet power to total input power. Another measure, called current efficiency is defined as the ratio of the plasma current to the grid current. It will be shown that the latter type of efficiency provides a more useful measurement when the RF plasma source is utilized. The nature of the plasma jet is the third and largest category of results. In this sub-section experimental data from all diagnostics are presented in order to understand how each controllable parameter affects the measurement. The collected data include Faraday cup measurements of total current, force measurements, and electron energy distributions from the GEA. These results are used in the next chapter in conjunction with presented COMSOL Multiphysics simulations to create a model of the IEC jet-mode operation.

8.1 Operational Limits of IEC Jet Mode

Discovering the operational limits of our IEC device is an important task that allows us to determine the controllable range of each external parameter. These parameters include the IEC grid voltage and current and therefore power, the chamber pressure, the radio-frequency power of the plasma ionization source, and the magnetic field strength of the helicon magnet coils. The IEC power supply allows control over the IEC grid voltage or grid current depending on if the supply is operated in voltage or current mode. Both of these parameters are controllable through the Labview interface. The pressure is physically controlled using the mass-flow controller to set the flow rate (typically 3.000 SCCM) along with a precise adjustment of the diagnostic sub-chamber gate valve.

Although some of the graphs in later sections are presented as a function of IEC power, this is not a settable parameter. The DC power supply for the cathode grid can run in current-limiting or voltage-limiting mode, meaning in order to reach a desired power level, either the voltage or the current (respectively) must be set arbitrarily high and the desired power reached by through an exploratory tuning of the other setting. For the majority of the data presented the power supply was run in current-limiting mode and the desired power was targeted through a careful tuning of the current setting. It was found later on however, that the power supply was actually more stable when operating in voltage-limiting mode. Additionally, the functional dependence of most of the measureable quantities such as electron energy spectra turned out to be functions of grid voltage rather than grid power.

The first important item in finding the operational limits of a plasma device is to measure the Paschen breakdown curves. These data were collected in collaboration with A. Krishnamurthy for her M.S. thesis work [21]. Krishnamurthy used different grid sizes and showed that grid size was not a major function in the Paschen breakdown. For this dissertation work, only the data for the 126 millimeter diameter grid is shown as it was the only one used for all collected data. This data subset is shown in Figure 24 with the narrow range of jet-mode propagation highlighted. Above the correct pressure range, the jet turns into spray-mode. The graph represents the entire range in pressure that it is possible to obtain the jet-mode of operation using only a DC glow discharge. As with all Paschen curves, on the low p-d side of the Paschen minimum the breakdown voltage rapidly increases as p-d decreases. For this experiment, the minimum p-d that can be used was limited by the requirement that the breakdown voltage not exceed around 10 kilovolts. This was due to safety (x-ray production) and equipment concerns (electrical arcing). Generally this was found to not be a major limiting factor since the IEC grid power supply had difficulty maintaining the plasma at low p-d factors before the safety limit was reached.

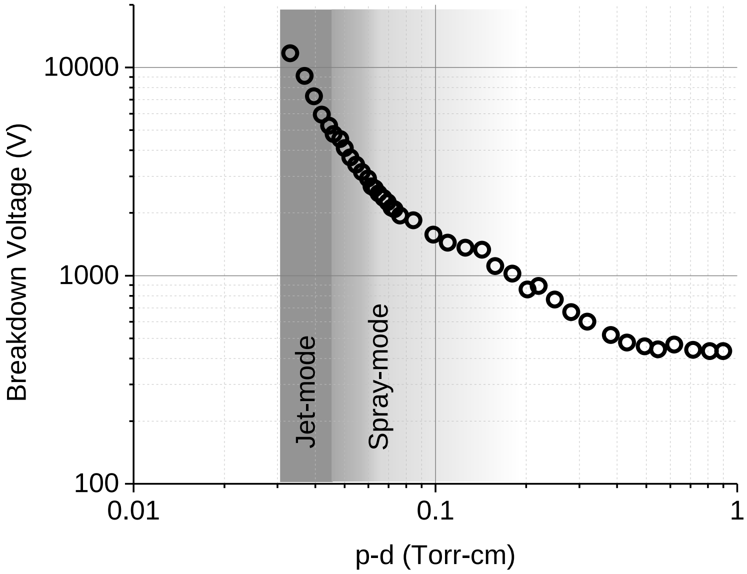

Figure 24. Paschen breakdown curve for the glow discharge IEC using a 126 millimeter diameter stainless steel grid. The pressure-distance (p-d) parameter range is shown for jet-mode and spray-mode operation.

The narrow operating pressure of the IEC jet-mode is made more explicit in Figure 25 by plotting the curve of main chamber pressure verses IEC grid voltage. In this figure the IEC grid current was fixed at 20 milliamperes, half the maximum available from the power supply. The pressure was swept by controlling the diagnostic chamber gate valve while flowing a constant 3.000 ± 0.002 SCCM of argon gas. At the low pressure end of around 1.29 millitorr (172 millipascals), the instability represented by the cluster of points results from the IEC grid power supply attempting and failing to sustain the glow discharge. Above this value, the jet-mode is possible until around 2.35 millitorr (313 millipascals) when the transition to spray mode occurs. It is difficult to say visually exactly when the transition occurs since it looks like the jet diverges gradually when increasing the pressure, however there is distinct knee in the graph at 2.35 mT that as will be demonstrated in a later section using Faraday cup data, represents a fairly abrupt transition into spray-mode due to vastly lowered measured plasma current.

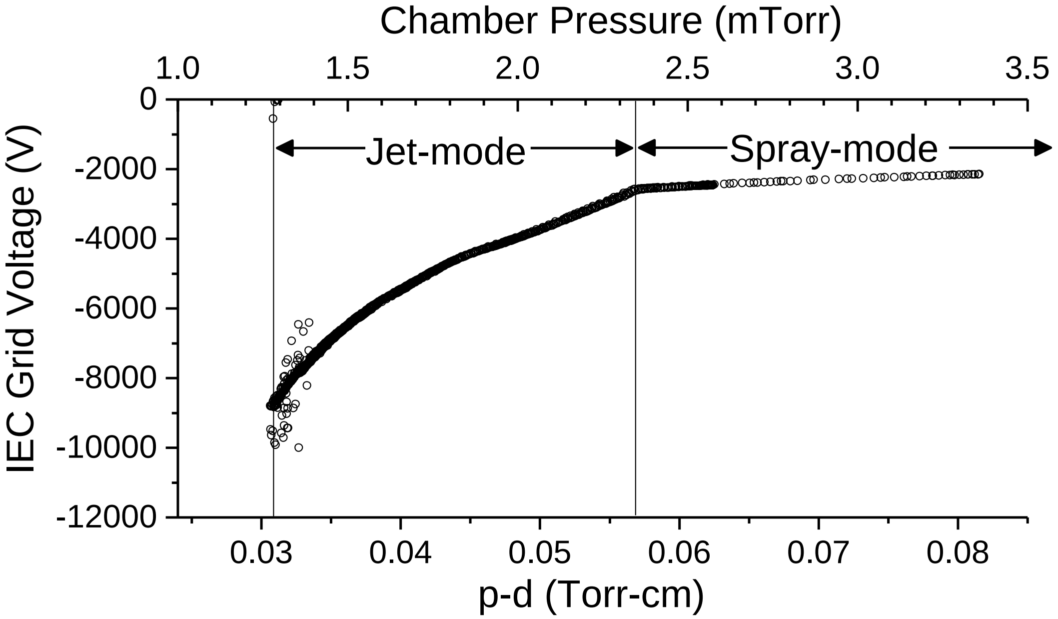

Figure 25. The grid voltage varies with respect to pressure when the IEC current is fixed (at 20 mA in this data). The scatter in the data around 1.29 mT represents instability in the power supply as it struggles to maintain the plasma. The knee in the curve around 2.35 mT represents the transition into the spray-mode of IEC operation.

Using a glow discharge to sustain the plasma means the pressure and voltage relationship is fixed for any given grid current. It is possible to break off this curve however if an external ionization source is introduced to sustain the plasma discharge. This is in essence the function of the RF/helicon power source. This effect is demonstrated in Figure 26 by examining the I-V characteristic curves at 1.48 millitorr. For a pure IEC glow discharge there is only one value of grid current for each grid voltage. However, when the RF ionization source is added, the current and thus the power delivered by the IEC power supply can be independently controlled (in a small range) by setting the RF power. An example is shown in the figure for around -5500 volts grid voltage. The IEC grid current in glow discharge is fixed at ~8 milliamperes. Following the grey contour indicates this is equivalent to around 40 watts delivered by the IEC cathode grid. Adding just 100 watts of RF power boosts the grid current to around 35 watts equivalent to around 190 watts delivered. By operating the RF power between 100 and 300 watts an operational range of 5 milliamperes is gained representing a power range of about 30 watts. When the RF source is run in helicon mode, the current and power delivered jumps drastically and are in fact outside of the range of this graph meaning that the grid power supply was not able to supply enough current for at that voltage.

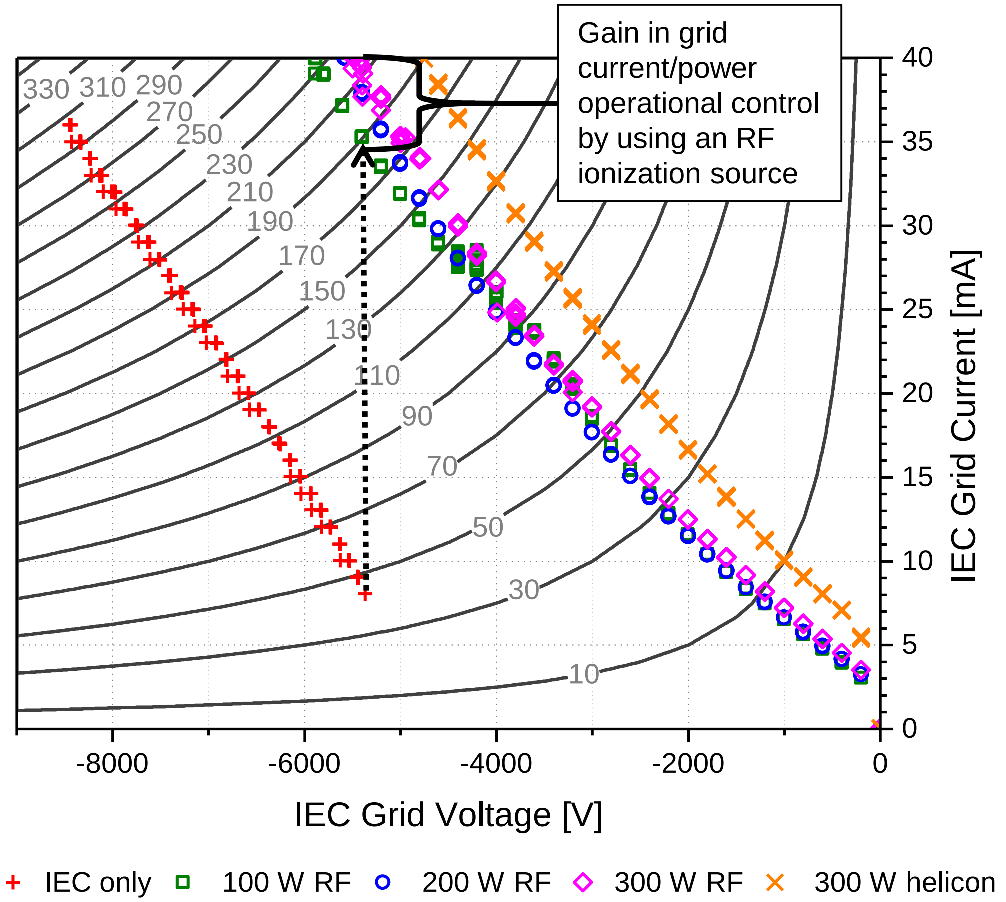
Gain in grid current/power operational control by using an RF ionization source

Figure 26. I-V Characteristic curves for the IEC device with DC glow discharge only and with RF power providing primary ionization. The grey contours represent power delivered by the IEC grid power supply in watts and is simply the product of the ordinate and abscissa of the graph. The graph shows how using an external ionization source increases the control in the adjustable parameters of the IEC discharge. Using only an IEC glow discharge there is no control in the grid current for each grid voltage. However, when RF ionization is used, the current and hence the power can be increased by increasing the RF power.

8.2 Efficiency Calculations of IEC Jet-Mode

Two kinds of efficiencies have been used to analyze the jet-mode. The total efficiency is the ratio of the total output power in the jet to the total input power of all power supplies, IEC grid, RF generator, and helicon magnets. While it is easy to read off the power supplied from the instruments, it is not trivial to measure the total power delivered by the jet due to more complexity such as thermal heating of the diagnostics and accounting for power loss mechanisms such as secondary electron emission and visible light production. Therefore, this measurement will only be presented for the IEC operating in a glow discharge with no RF ionization sources.

In order to calculate the power available in the plasma jet, a measurement of the thermal power representing the heat deposition was made using the Faraday cup equipped with a temperature sensor. The measurement utilized the RTD thermal sensor which recorded the temperature rise in the device over time. By using a calibrated COMSOL model of our cup, the temperature rise was converted into a thermal power. The details of this calibration were provided in chapter 5.2. Figure 27 shows the thermal power plotted as a function of IEC grid voltage for a pressure of 1.5 milliTorr argon gas. Although the thermal power absorption is also shown for RF power supplies, the thermal power absorbed by the cup is much larger for the IEC glow discharge.

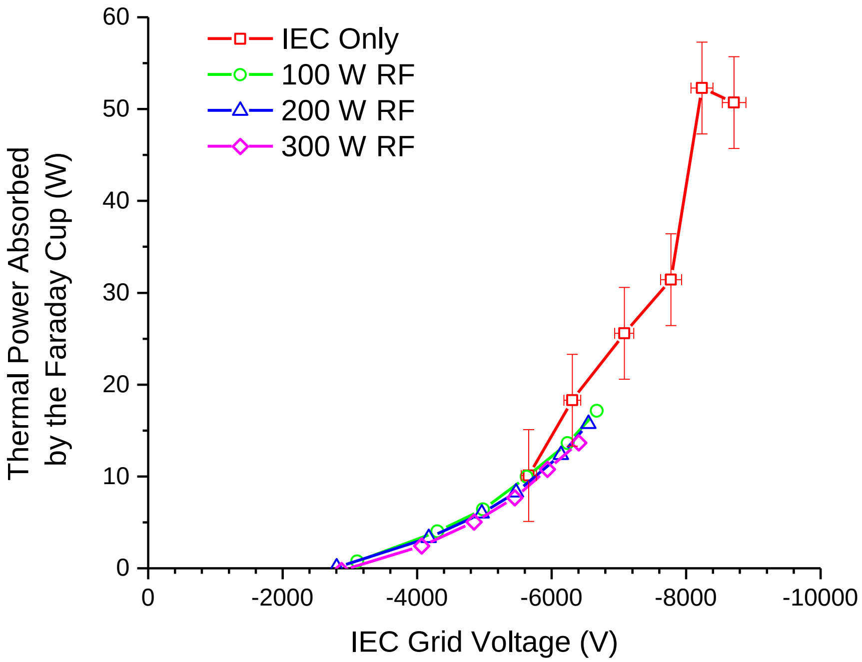

Figure 27. Thermal power measured using the Faraday cup was used to make an estimation of the total efficiency of the IEC device in converting input power to the grid to power in the plasma jet. The vertical error bars result from a large error in experimental repeatability and calibration error in the thermal measurements. The horizontal error bars are due to a ~2% IEC grid voltage instability due to the power supply.

Using the "IEC Only" data in Figure 27, the total efficiency in converting the input power into jet power can be calculated for IEC glow discharge operation. The graph in Figure 28 shows that the total efficiency is about 20% for all voltage values when the IEC device is run at low pressure (1.5 millitorr). This decreases to around 7% when the pressure is increased to 2.0 millitorr even though this is still in the jet-mode pressure range. The total efficiency then has a strong pressure dependence yet and no discernable dependence on the grid voltage. While it is possible to calculate the total efficiency of the device when using an external ionization source, the efficiency numbers look very poor when several hundred watts of power are included in the calculation. In fact, the total efficiency was only around 1-3% for low pressure 1.5 millitorr when the RF source is used. The efficiency was even found to decrease slightly with increasing power.

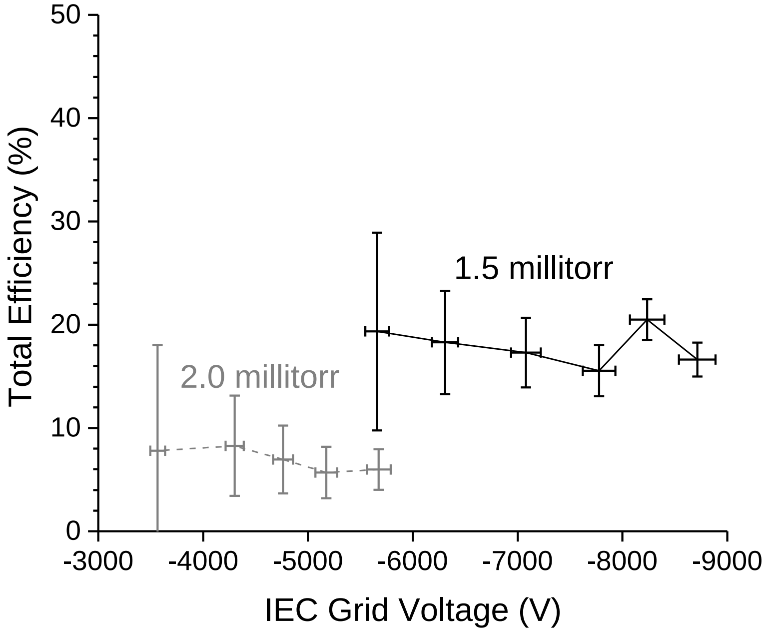

Figure 28. The total efficiency is defined as the ratio of the thermal power measured from the plasma jet to the power supplied to the IEC cathode grid. The efficiency for IEC only operation is shown to be about 20% which means a large fraction of power supplied to the grid ends up in the jet. The sources of the error are the same as in Figure 27.

The current efficiency is a measure created to determine the effectiveness of different ionization sources on the plasma current available in the jet. It is defined as the ratio of collected plasma current to the IEC grid supplied current. The graph in Figure 29 shows this calculation for several different RF power levels. Helicon mode RF is not shown because the geometry of this experiment means that the magnetic field deflects the plasma jet away from the detector and thus it registers an artificially lower value for the plasma current. Once again, the current efficiency is measured at around 20%. Of course this because for the glow discharge operation, the IEC grid current is directly related to the grid power.

When an RF source is added though the relationship is much more complex and the current efficiency is significantly lower. This could be interpreted in two different ways. The plasma current in the Faraday cup and GEA are always negative in sign as will be shown in later subsections. We can then assume that the jet has a large component of electrons accelerating away from the negatively biased grid. If RF power lowers the plasma current that could be interpreted as a strong increase in the number of positive charges being dragged along in the jet, cancelling out some of the plasma current. However, this interpretation doesn't line up with the measurements of total efficiency. As mentioned earlier, the total efficiency decreases by an order of magnitude when the RF source is used. If everything stayed the same we would only expect it to decrease by a factor of only 2-3 due to factoring the added power into the total power denominator of the ratio. A large number of ions impacting the diagnostic would cause extensive additional heating and increase the measured thermal power yet the decreased heating is actually observed as in Figure 27. It can be concluded then that the RF ionization probably does not produce significant additional ions into the plasma jet.

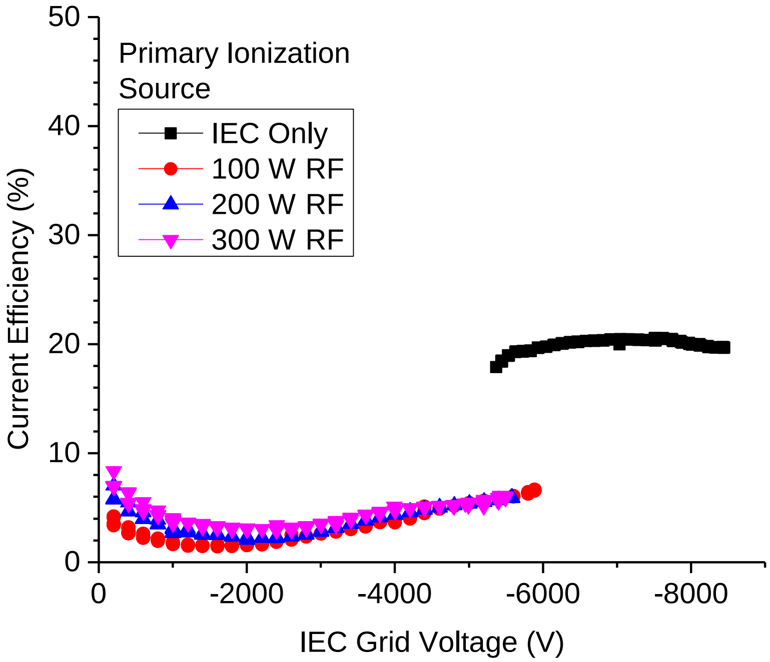

Figure 29. The current efficiency is defined as the measured plasma current over the current supplied to the IEC cathode grid. It useful in comparing the impact of using an external RF ionization source on the plasma jet current.

8.3 Nature of the Plasma Jet

The major focus of this dissertation involved the study of the nature of the plasma jet. There are several features of interest including the electron and ion energy spectra, the pressure of the jet, and the power. Study of these properties involved the use of the Faraday cup, gridded energy analyzer and plasma force sensor.

The power in the plasma jet can take several forms. The previous section demonstrated the thermal power, e.g. the power absorbed into the plasma-facing material of the diagnostic and dissipated as heat. The plasma current provides another form of power. This is measured as electrical current in the Faraday cup and GEA. A comparison of the total current collected by these two diagnostics for the same plasma conditions show good general agreement after accounting for the geometry differences. The plasma current is the main measurement that makes up the electron and ion energy spectra. The measurements of each will be discussed including how the captured GEA I-V curves are turned into spectra. Finally, the results of the forces measurements of the plasma jet will be discussed. It was found that the forces measured on the plate were not due to plasma jet momentum transfer but rather the radiometric force.

8.3.1 Plasma Current Measurement using Faraday Cup and GEA

The Faraday cup and the gridded energy analyzer are both mounted on the same linear motion feedthrough, cantilevered at the end of a threaded rod. This means that both diagnostics are at approximately the same distance from the IEC grid with a positional variation of only about 1 cm due to their length difference (the GEA is slightly closer since it is longer). The alignment for each device is performed by hand as detailed in chapter 3. The apertures of the two devices are comparable however the GEA is slightly larger. It has a precisely cut 1.000 ± 0.005 inch aperture while the Faraday cup utilizes a slightly smaller aperture with a nominal diameter of 0.875 ± 0.01

inch. The GEA also has grids that are 92% transparent by design but likely somewhat less in reality so due to slight misalignments of the 3 grids. With the geometric factors taken into account, the GEA should collect ~20% more current than the Faraday cup for the same conditions.

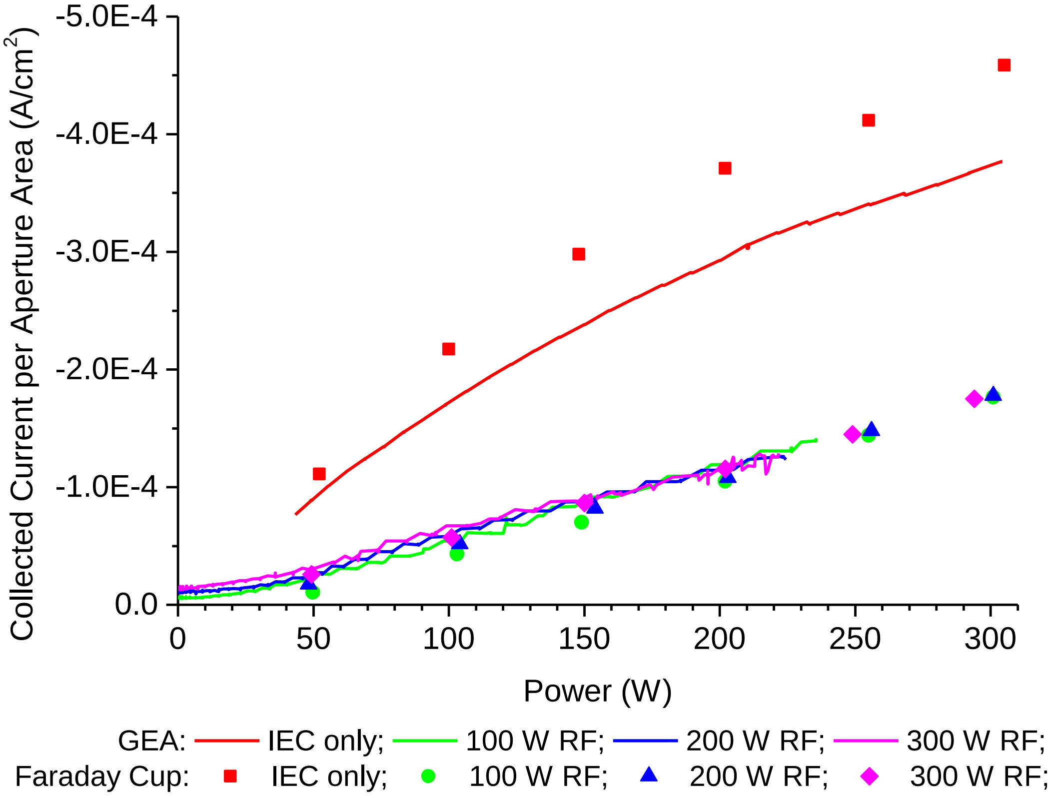

Figure 30. The collected current by the two diagnostics, the GEA and the Faraday cup are in good agreement when the RF power is used however deviate significantly from each other for the IEC glow discharge. These measurements were taken at 1.5 millitorr argon gas pressure with each diagnostic's position closest to the IEC cathode grid, at the approximate ground plane.

The collected plasma current normalized by the aperture size is plotted in Figure 30 for the two diagnostics. First, the general trend is that the plasma current becomes increasingly negative as the IEC grid power increases. Since this is conventional current, this is indicative of a large flux of electrons in the jet making their way to ground after striking the collector. This makes immediate intuitive sense since the grid is negative in potential with respect to ground meaning electrons born in the center of the chamber accelerate out toward the grounded walls.

The Faraday cup and the GEA are in good agreement when the RF power is enabled. However when examining the trend for the glow discharge “IEC only”, there is large offset in the plasma current verses the RF power conditions. If the plasma current is plotted as a function of the IEC grid voltage instead of the power as in Figure 31, now the all the trends overlap to such a degree that the IEC grid voltage must be the variable that most strongly determines the jet mode plasma current. Looking closely at the collected current for each RF power level, there is a small noticeable trend that increasing RF power slightly increases the jet current. This happened for both diagnostics so the effect is likely real. Comparing the “IEC only” glow discharge with RF power settings at -6000 volt grid potential shows that adding a few hundred watts of RF power doesn’t have a significant effect on the plasma current. The RF power must be having some other effect inside the central grid instead of its intended purpose of boosting the jet-mode power. The spherical probe data from chapter 4 indicated that only about 4% of the input power to the RF antenna wound up as measurable power to the probe. That indicates that the difference in plasma current may be too small to be noticeable. It is also possible that most of this power just flows straight into the grid causing metal sputtering.

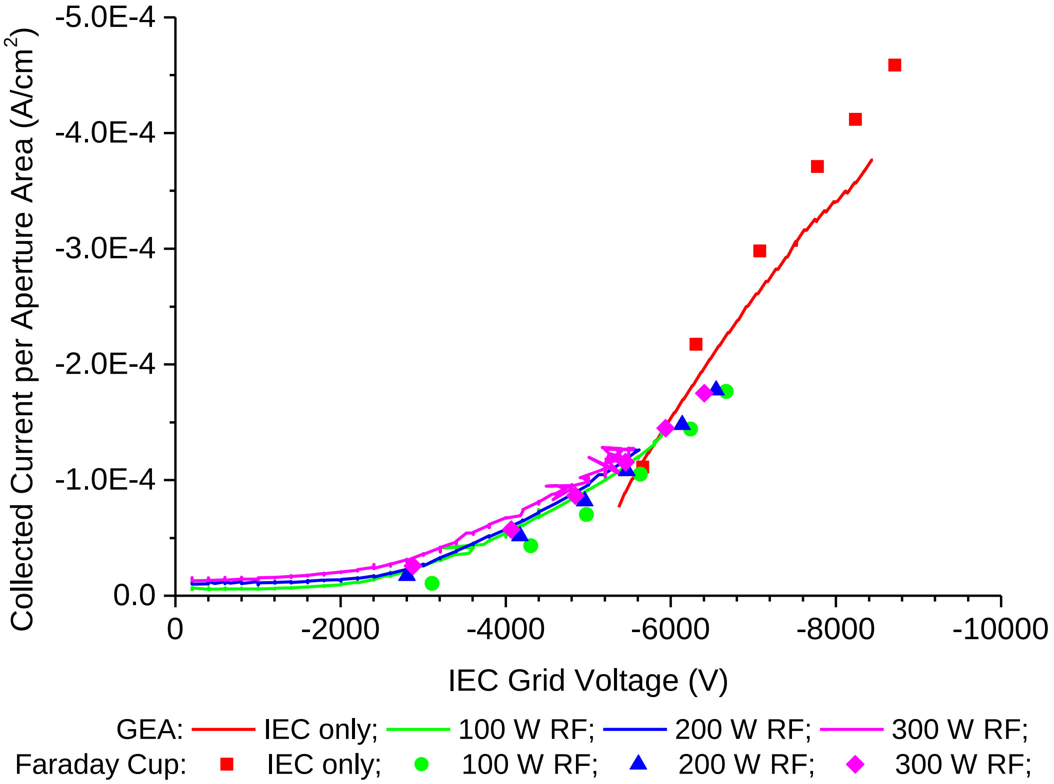

Figure 31. The collected current for each diagnostic plotted as a function of IEC grid voltage shows a much difference trend than verses IEC grid power indicating that the IEC voltage is the true independent variable determining the jet mode current.

8.3.2 Gridded Energy Analyzer Spectra

The ion and electron energy spectra are the most important properties to know about the plasma jet. These properties are also the most difficult to measure and to interpret. The main instrument to study the spectra was the gridded energy analyzer. The GEA was run in two different modes referred to as electron and ion spectra mode. As mentioned in chapter 6, electron spectra mode requires that the ion sweep grid is turned off and the electron repeller grid is swept through large negative voltages. For ion spectra mode, the electron repeller is held near the maximum negative potential before breakdown inside the diagnostic and the ion sweep grid is varied from 0 to +1000 VDC. Because of the very large electric field inside the GEA, there was a large degree of instability in the measured data. Electron energy spectra were captured however no ion spectra were produced. This is explained in detail in chapter 8.3.2.4.

8.3.2.1 Paschen Breakdown inside the Gridded Energy Analyzer

Once a breakdown occurs inside the GEA, no more data can be collected pertaining to the plasma jet so this represents a hard limit to the maximum electron energy that can be measured. Because the breakdown inside the GEA is an important property, a Paschen breakdown curve was measured for this diagnostic. To collect this data, the electron repeller grid was increased until a simultaneous jump in current was recorded by the collector plate and the Ametes current sensor which registered the current delivered to the electron repeller grid. An example of this process is shown in Figure 32. The error is large because of the difficulty in deciding exactly when the breakdown occurs. The GEA measures a dark current before any plasma glow is visible and before the Ametes current sensor registers an increasing in electron repeller current. The breakdown itself is rather gradual but was loosely defined for the purpose of the Paschen curve as the point where the electron repeller grid current exceeded 1 milliampere. The grid spacing was ¼ inch or 0.63 centimeters since it was assumed the breakdown occurred between the electron repeller grid and the nearest grounded grid, the ion sweep grid.

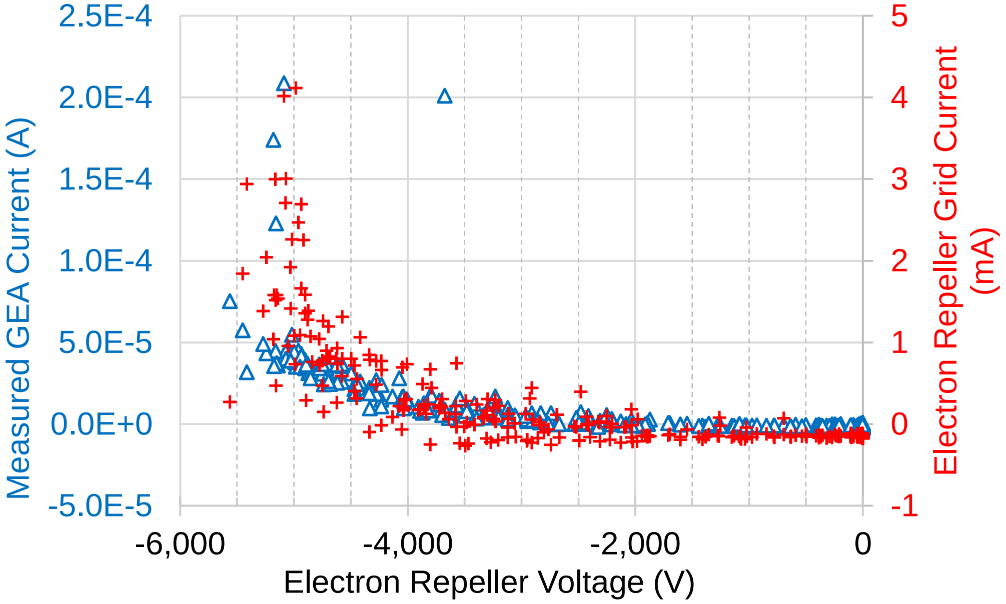

Figure 32. Detailed example data of Paschen breakdown inside the GEA at 4.55 millitorr.

The Paschen breakdown inside the GEA is shown in Figure 33. The curve is plotted on a log-log scale with the measurement error approximated by the size of the points. The electron repeller was forbidden from exceeding 10 kilovolts so the minimum p-d we were able to achieve occurred for a pressure of 1.3 millitorr, similar to the minimum IEC grid voltage in glow discharge mode. When plotted on the same graph as the IEC breakdown voltage, it is immediately apparent that they don’t match up very closely. While it might be expected that the curves should lie on top of each other since the gas is the same, there are several factors that influence the Paschen breakdown. The material property of the electrodes is dependent on secondary electron emission from the electrodes. The IEC grid is stainless steel while the GEA grids are all tungsten, each having a different secondary electron coefficient. Additionally, it has been demonstrated experimentally by Ledernez et. al. in 2009 that the Paschen curve for argon is actually a function of p-d and d for values of d in the same range as the GEA grid spacing [22].

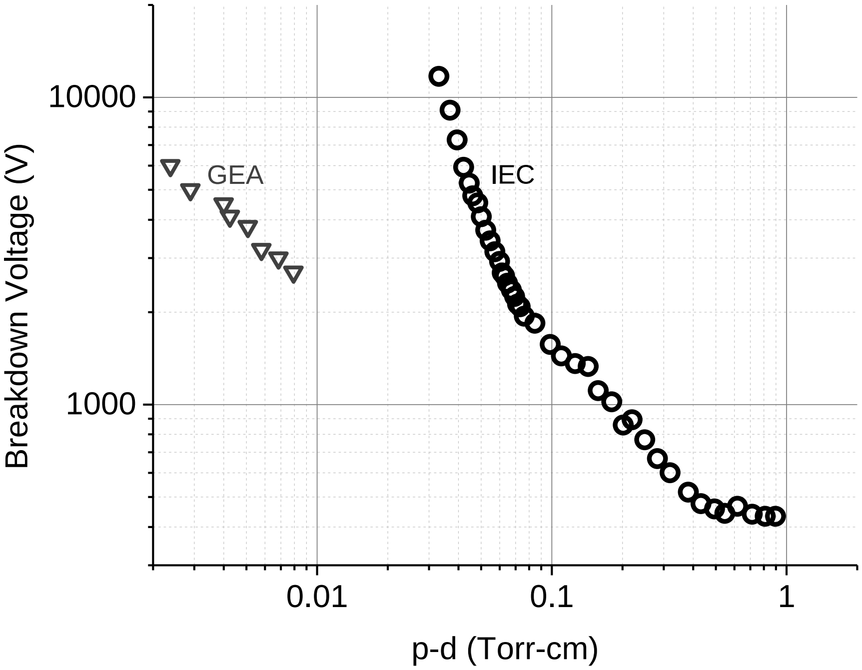

Figure 33. Paschen breakdown inside the GEA from the electron repeller grid shown alongside the IEC glow discharge breakdown.

There are two contrary objectives when choosing the thickness of the ceramic between the GEA grids. Obviously to avoid plasma breakdown, p-d needs to be kept as small as possible such that the breakdown potential remains high. However this introduces the possibility of arcing across the surface due to contamination. In fact, the latter is the cause of the total failure of the first generation design of the GEA. The issue remains in the second generation design since the diagnostic sees a large amount of sputtered grid material. This is demonstrated by the photographs in Figure 34.

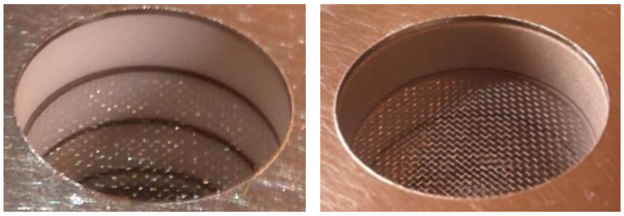

Figure 34. Side-by-side comparison of the white pristine GEA aperture and grey post-experiment aperture showing heavy sputter deposition on the Macor ceramic spacers. Failure of the second GEA occurred by conduction along the metal-sputtered inner walls.

8.3.2.2 Stata and Mathematica Data Analysis

Since the electron spectra was the easiest to capture and allowed us to obtain experience with the operational limits of the GEA, it was the first to be collected. Figure 35 shows the collected current as a function of the electron repeller voltage. This represents the first step in the analysis as the time component has been removed and the I-V curve plotted. The GEA collected current measurements represent the total current for all electrons with energies above the electron repeller voltage. The second step then is to calculate the slope of the curve to obtain the electron energy spectrum. However because each I-V trace has significant measurement noise it must be smoothed before a derivative yields useful information.

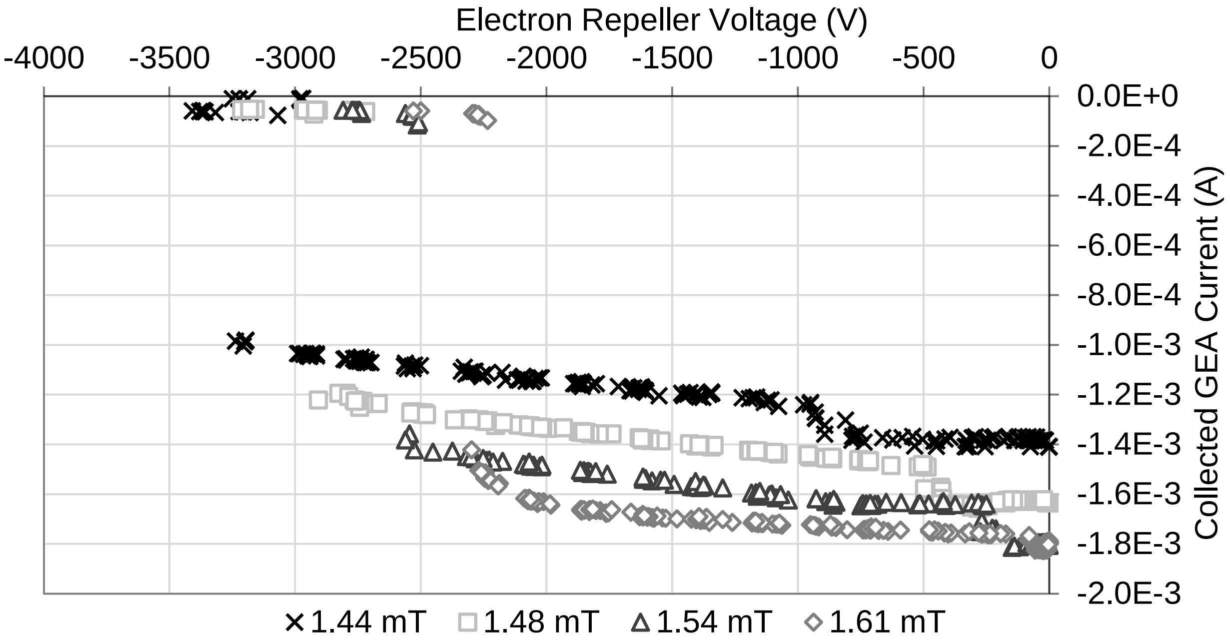

Figure 35. Collected current for GEA run in electron spectra mode for a small range of pressures at 50 watts IEC grid power.

The program Stata/SE 11.1 by StataCorp LP was used to apply a smoothing filter. The filter uses a kernel-weighted local polynomial smoothing with variable degrees of freedom and kernel half-width. After some trial-and-error, it was discovered that the filter performed reasonably well without too much loss of detail around important drops in the current using a Gaussian kernel with 1 degree of freedom and a halfwidth of 100 points. Additionally the evaluation was performed at each voltage value rather than an evenly spaced grid. Figure 36 illustrates the process of cropping the data set and doing the smoothing operation.

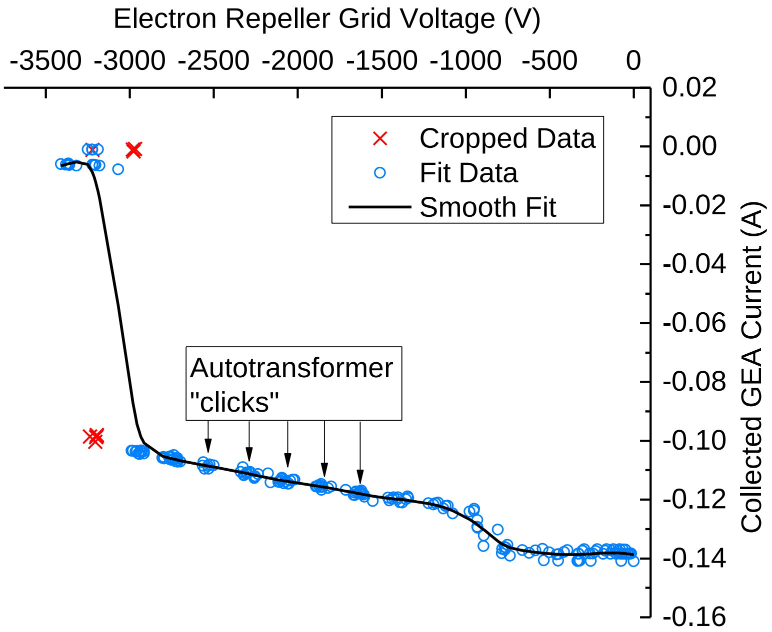

Figure 36. An example of the result of the smoothing filter is shown for 1.48 milliTorr and 50 watts IEC grid power. Eliminated data points before the filter was applied are shown as red X's while the data used are the blue circles. The black line represents the smoothed result. The error in the position of the large peak comes from the decision on which data points to crop.

The choice on which data points to crop ultimately effects the position of the peak once the derivative is taken and is not always easy. Generally points were cropped in such a way that the smoothing filter did not become too confused and give a fit that produced an unintelligible derivative. The reason that the data points are so unevenly space is due to the electron repeller grid power supply. It was an analog Hipotronics power supply with the voltage set through a large autotransformer meaning that the voltage has a fixed number of possible settings correlated to the number coil windings. Each new voltage setting is equivalent to another "click" to a new winding. Since the maximum range of the power supply was 100 kilovolts and this experiment only required up to 4 kilovolts that meant that each "click" represented a significant jump in voltage. A small spread around each fixed setting was achieved by performing many sweeps through the electron repeller voltage range however this issue meant that precision around the important drop in voltage was unable to be realized. It is suggested to use a more precise power supply to feed the electron repeller grid in future work.

There is one more phenomenon worth mentioning in the electron repeller grid voltage sweep data. A hysteresis was evident as the reason for the overlapping points that were removed when smoothing the data. This is shown in Figure 37 for 1.48 millitorr chamber pressure. The transition voltage from high to low current occurs about 200 volts higher when ramping up voltage as opposed to ramping down the voltage. The reason for difference can be explained by the space charge of the plasma jet modifying the local electric potential. When ramping up the electron repeller grid voltage, this modification allows the jet to reach slightly higher energy. When ramping down, the jet must be reestablished near the electron repeller grid for the glow discharge electric potential.

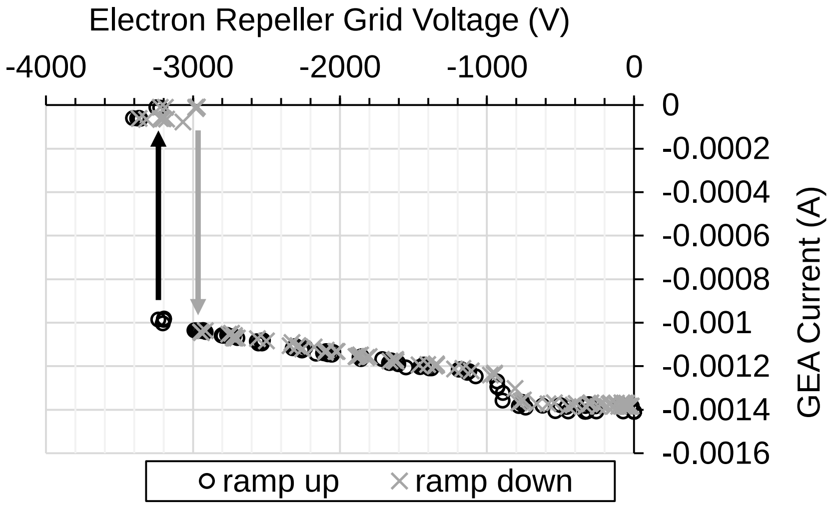

Figure 37. A hysteresis is present in the electron repeller grid voltage sweep data. The transition point is higher by approximately 200 volts when ramping up as opposed to ramping down the voltage.

8.3.2.3 Electron Energy Spectra Results

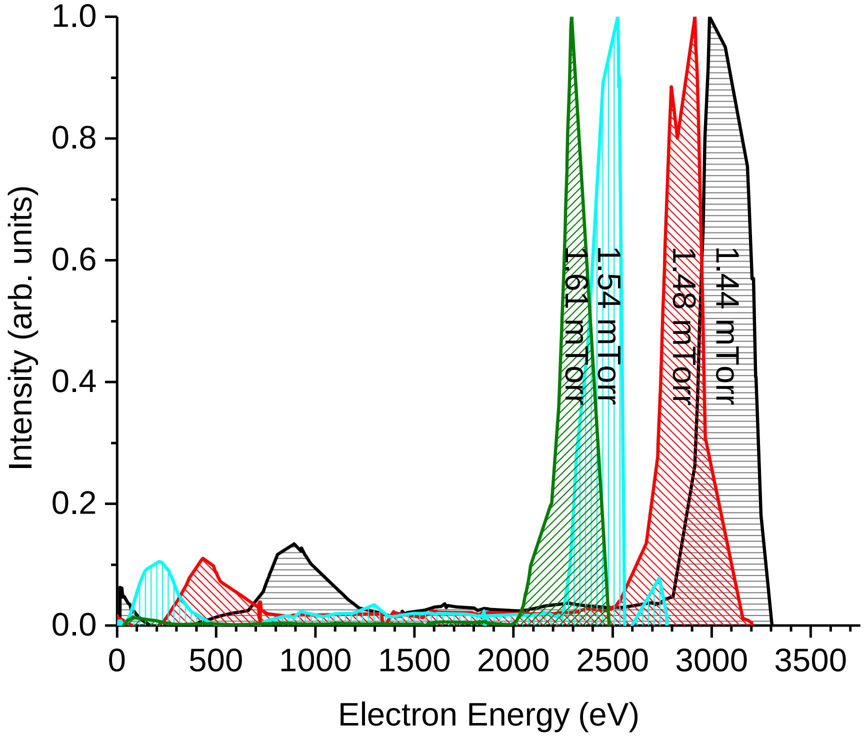

Figure 38. Electron energy spectra for 50 W IEC grid power are shown for pressures of 1.44-1.61 mT. The spectra are normalized by the maximum peak height. There is a clear trend that the peak of the electron energy spectrum decreases with increasing pressure. The sharp drop off in intensity after the large peak may be an artifact of the smoothing filter and not a function of the actual physics.

The electron energy spectra for the low power condition of 50 watt IEC grid power are shown in Figure 38. There are several important features about these spectra that warrant some discussion. First, the spectra are double-peaked. There is a small first peak in the range of a few hundred electron-volts. Then there are a smaller number of electrons with energies that fall in between the two peaks. The second large peak is a significant fraction of the IEC grid voltage. The trend related to pressure is also quite clear: both peaks shift toward higher energies when the pressure is decreased. This shift is shown to be very sensitive to the pressure. For example, decreasing the pressure from 1.48 to 1.44 millitorr causes the peak electron energy to increase by about 400 electron-volts. This indicates that the operation of the IEC jet-mode is a strong function of the mean-free-path of the electrons in the plasma. This concept will be revisited in the modeling chapter.

The small peak may be explained by examining the electric field between the electron repeller grid and the grounded ion sweep grid. If the electron repeller voltage is set to -1000 volts that means that the electric field between those grids is around 143,000 volts per meter. In the small distance of ¼ inch available for the electrons to accelerate, they can gain an energy of about 900 volts. This agrees well with the peak for low pressures. This means that the small peak arises due to electrons created very near the electron repeller grid and their spread in energy relates to the exact position of their birth. The electrons are most likely created through ion collisions with the electron repeller grid creating low energy secondary electrons.

It is instructive to look at the relationship between the peak of the electron energy spectra and how it relates to the IEC grid voltage. These spectra were all captured at 50 watts IEC grid power meaning the voltage was slightly different for each since it has previously been shown that the grid voltage is strong function of pressure for a glow discharge. Figure 39 shows that for each pressure value, the ratio of the peak energy to the grid potential is around 0.5 indicating that the electrons gain kinetic energy equal to about half of the grid potential. These data will be used in chapter 9 to show that location of the birth of the majority of the plasma jet electrons occurs near the cathode grid aperture.

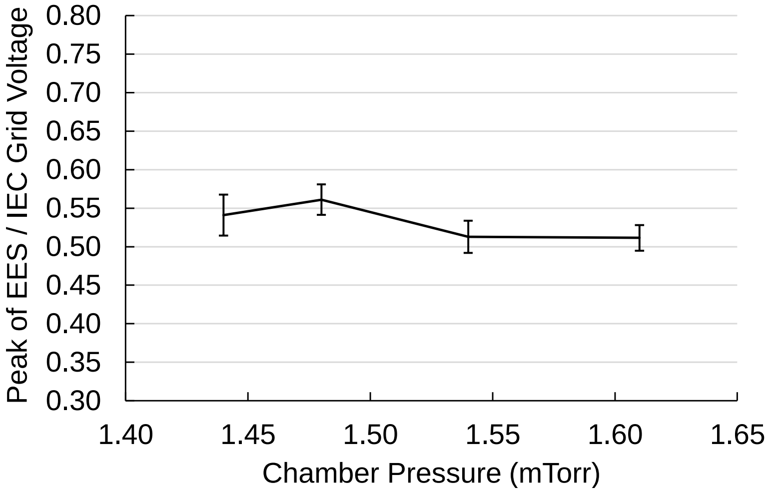

Figure 39. The ratio of the peak of the electron energy spectrum (EES) to the IEC grid voltage shows that for each value of pressure, the electrons gain kinetic energy equal to approximately half of the of the grid potential. The error bars represent the full-width half-max of the peaks.

8.3.2.4 Ion Energy Spectra Results

Capturing an ion spectra is done by setting the electron repeller grid voltage to a level high enough to repel all the plasma electrons. The previous sub-section showed that the largest peak of the electron energy is at least half of the grid voltage which requires setting the electron repeller to over -3000 volts. Then the ion sweep grid could be run from 0 to 1000 volts. The original intention was to run the sweep at a frequency of 10 hertz however difficulties with noise in the signal using an oscilloscope required signal collection using the DAQ which runs at much lower frequency. To compensate the ion sweep was performed at 10 millihertz meaning that each sweep required 100 seconds to complete. During that time, the baseline of the signal would drift slightly however general shape of the signal was still apparent.

Although several attempts were made to collect ion spectra, it was not possible to set the electron repeller voltage high enough to repel the highest energy electrons in the spectrum. When it was finally discovered which conditions would work the GEA experienced a failure due to the sputtered material accumulated on the internal ceramics causing a short between the electron repeller grid and the ion sweep grid along the now conductive sidewall. This was shown previously in Figure 34.

8.3.3 Force of Plasma Jet

So far the evidence presented points to the plasma-jet consisting of a high energy beam of electrons. The plasma force sensor can determine if there is also a component of ion or neutral atoms riding along in this electron beam. As shown previously in the force sensor calibration chapter, the sensor itself is capable of discerning forces as small as 1 millinewton.

The output of the force sensor for a typical long-duration plasma jet pulse is shown in Figure 40. The x-axis is scaled such that the plasma is ignited at time zero for each data set. It takes about 120 seconds to establish a new equilibrium value. A force pushing the sensor backward registers as an increase in voltage so it appears that the new equilibrium value is a positive force on the sensor.

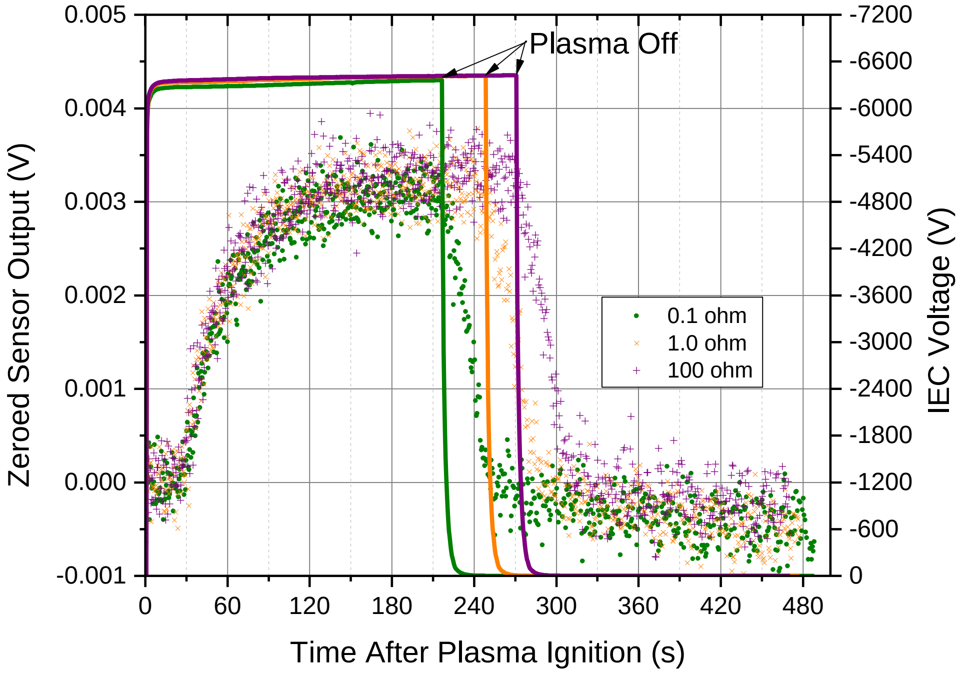

Figure 40. The force sensor takes about 120 seconds to establish a new equilibrium after plasma ignition regardless of the value of the plate grounding resistor. After the plasma is extinguished the sensor only takes about 60 seconds to go back to its original level. Solid lines represent IEC grid voltage which was nearly the same value for each set.

It is immediately noticeable that the sensor takes quite a long time to respond to the plasma and then even longer to establish a new equilibrium. Several experiments were untaken to determine the cause of the slow sensor response. It was hypothesized that the plate was charging like a capacitor and this was somehow affecting the sensor output without actually registering a force. However as shown in Figure 40, the resistance to ground of the titanium force plate does not affect the time constant of this capacitive-like behavior. Additionally the decay is twice as fast as the rise time which doesn't fit with a stray capacitance as the issue. The rise time was also not found to be correlated with the IEC grid voltage, and was always about 120 seconds regardless of the plasma conditions. Perhaps the strangest aspect of the force sensor response is the 30 second dead time before the sensor even responds to the plasma being switched on although this dead time doesn't occur when switching it off. From a visual stand point, the plasma jet is established immediately after the plasma is ignited and diagnostics measuring the current record a step change.

Assuming that the new equilibrium established on the force sensor shown in Figure 40 represents an actual force, it can be plotted as a function of the IEC grid voltage as in Figure 41. The trend is clearly positively correlated with power. Because of the high noise level in the signal, the error bars are large at about ±1.4 milliNewtons. In the modelling chapter, some analysis will be provided to determine which of the possible plasma species, ions, electrons and neutral particles might carry the pressure shown on the plate.

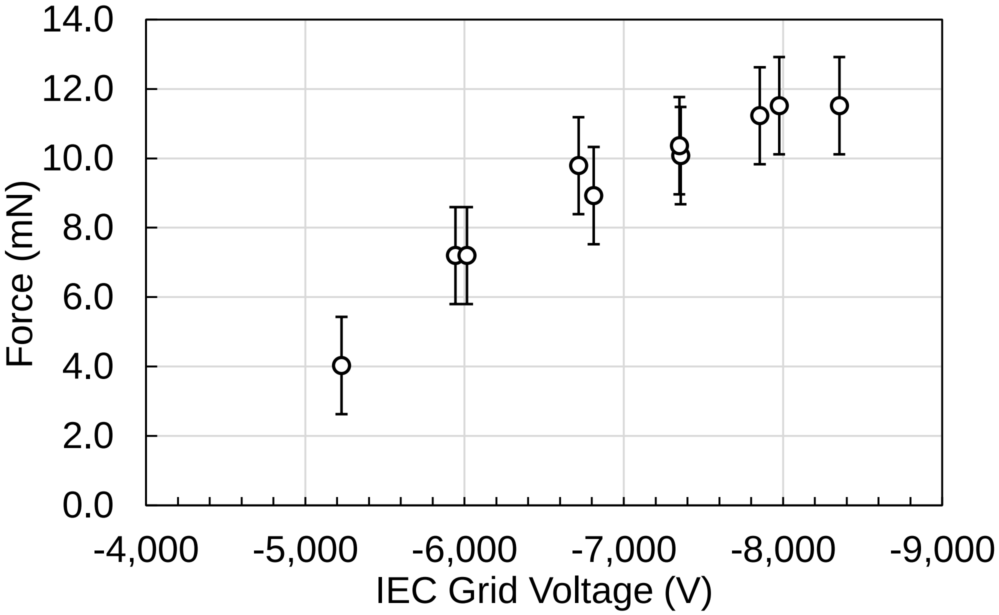

Figure 41. Force measured by the plasma force sensor as a function of the IEC grid voltage. The error bars are ± 1.4 millinewtons representative of the signal noise. The error from the calibration of the sensor is not factored in this graph since it represents a smaller contribution than the measurement error.

8.3.3.1 Radiometric Force as Explanation of Force Sensor Results

It will be shown in the modelling chapter that the pressure on the plate cannot originate from species in the plasma jet. However the results of the force sensor measurements can be explained by the radiometric force [23]. It is a thermal phenomenon that results from uneven heating of the target plate and is amplified by the particular geometry of the diagnostic chamber. This section is dedicating toward explaining this force and how it affected the force measurements. Some suggestions will be made on how to eliminate or minimize this force for future force sensor experiments.

The radiometric force is strongest in the transitional flow regime, i.e. when the Knudsen number is a little less than one. The Knudsen number is defined as

$$K_n = \frac{\lambda}{L} \tag{5}$$

where λ is the mean free path of gas particles and L is the characteristic length representing in this case the average dimensional size of the chamber, taken to be around 20 centimeters. The mean free path is calculated from Lieberman (3.5.7) using

$$\lambda \approx \frac{1}{330p}\ [cm], \qquad (p\ in\ Torr) \tag{6}$$

making the mean free path approximately 2 centimeters for typical IEC jet-mode operating pressure [24]. This puts the Knudsen number around 0.1 for which the radiometric force is large [25]. There are three components of the force: two act from the hot to the cold side of the plate called the area and edge forces and the third called the shear force is small and acts from cold to hot. The area force results from hot molecules transferring more pressure to the plate then cold molecules since their momentum is higher. The edge force results from non-uniform gas heating near the edge of the plate. From Scandurra [26] the normal force on a thin plate in the presence of a thermal gradient is

$$F_{norm} = (2-\alpha)\frac{15}{32\sqrt{2}\pi}\frac{k}{\sigma^2}\Delta T l \tag{7}$$

where k is the Boltzmann coefficient, $\pi\sigma^2$ is the collisional cross section and α is the energy accommodation coefficient defined as

$$\alpha = \frac{E_{in} - E_{re}}{E_{in} - E_w} \tag{8}$$

The factors E_{in}, E_{re}, and E_w respectively represent the incident particle energy before a surface collision, the reflected particle energy after a collision and the energy of a particle having a temperature equal to the surface. It has a value between 0 and 1. For argon incident on machined stainless steel the value has been shown to be 0.87 [27]. Although the plate is titanium, this value will be used in this calculation since it is representative of most metals for heavy gases.

To obtain an estimate as to the thermal temperature differentials that may be expected, a COMSOL simulation was performed on the force sensor plate. A heat source was set to 50 watts on the center of the plate and the temperature was tracked for the volume using appropriate material constants for the aluminum, titanium and alumina ceramic. Figure 42 shows the model geometry as well as the steady-state solution. The heat builds up significantly until the plate becomes hot enough to radiate away the input power. It shown in Figure 43 that the center temperature of the plate reaches a few hundred degrees Celsius after only a couple minutes. The edge of the plate however takes about a minute to show any change. While it was not the original intent to study the radiometric force in depth in this work, it is apparent that if the radiometric force on the plate is primarily due to the edge temperature that would explain why the force takes tens of seconds to materialize. Additionally, if the force also has a component that depends on the difference in these two temperatures, the center – edge temperature difference in Figure 43 reaches an approximate equilibrium after about 2.5 minutes. This aligns well with the time scale seen in the experiment. Because the radiometric effect has several components, it is likely that all contribute to the total force with different magnitudes at different times.

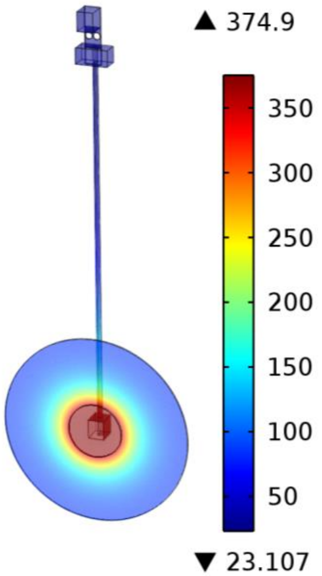

Figure 42. A COMSOL thermal simulation of the force sensor plate with a 50 W heat source. This image shows the steady-state solution. The scale bar is in degrees Celsius.

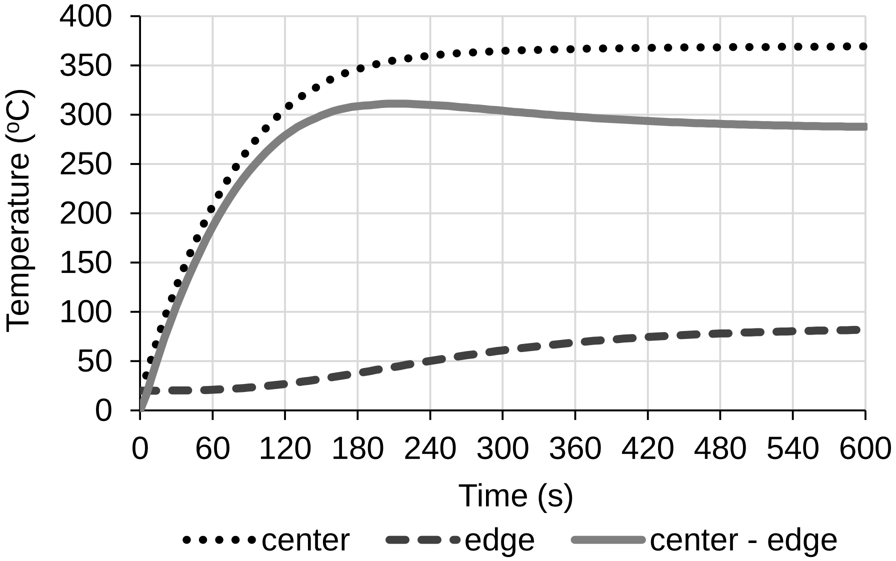

Figure 43. The temperature vs. time plotted for edge and center of the plate.

If the magnitude of the force is calculated from equation 7, we obtain a plot as shown in Figure 44. The large temperature differentials produce a force that approximates the experimentally demonstrated values. It is noted that the 50 watts input thermal power relates to the force for the highest shown voltage values in Figure 41.

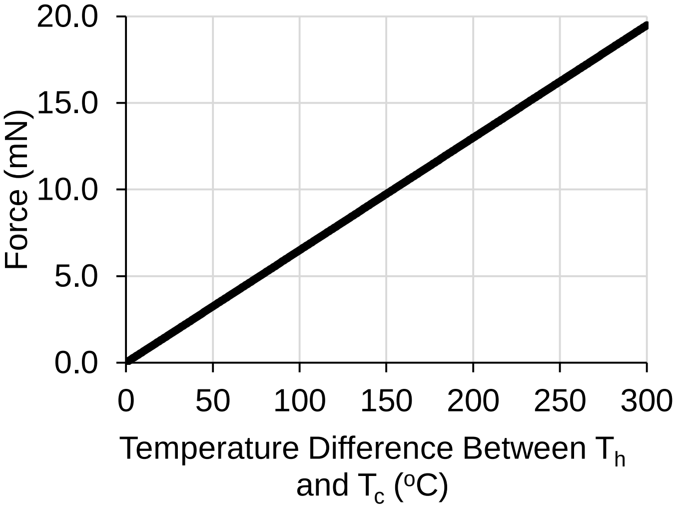

Figure 44. Calculated radiometric force using equation 7. The simulated temperature differentials produce forces in the range of experimentally demonstrated values.

After demonstrating evidence that the force measured in the experiment was likely due to the radiometric force, it is desirable to prevent this force from having such a strong effect on future force sensor work. Fortunately after the lessons learned here, simple steps can be taken to minimize this force. Because the force is prevalent in the transitional flow regime, we can move out of this regime and into molecular flow by decreasing the pressure in the diagnostic sub-chamber. To do this requires only reinstalling the drift tube and aperture so that the sub-chamber can once again be differentially pumped. Another simple way to minimize the edge radiometric force is to shrink the size of the plate so that it is not in such close proximity to the chamber walls. The spot size of the jet is presently only about 2-3 centimeters in diameter at the plate so the full 12 centimeter diameter plate is unnecessary. Finally, if the plate is to remain grounded, the alumina ceramic rod could be replaced with a heat pipe to prevent the large thermal gradients from accumulating. The use of an alumina ceramic lever arm was done to allow for biasing of the target plate, however in practice this was never done.

9.0 Model of IEC Jet-Mode Formation and Propagation

A general model of the plasma jet formation from an IEC device is presented in this chapter. Although, no direct experimental data was collected about the plasma conditions inside the cathode grid, using the experimental results of the external properties of the jet along with knowledge of the simulated electrostatic potentials and some basic theoretical limiting calculations, we can form a general understanding of how the jet forms and how its properties should change with respect to certain experimental parameters. COMSOL simulations were performed to solve for the electrostatic properties of the IEC grid geometry; the electric potential and electric fields in the absence of plasma are presented. The basic model is then compared with the experimental results of the electron energy spectrum to expand it to predict the location of the birth of the peak electrons in the jet. Next two limiting calculations will show that measured quantities fall within the range described by our model. Finally, evidence of the model's ability to predict certain observed quantities and visual phenomenon will be presented.

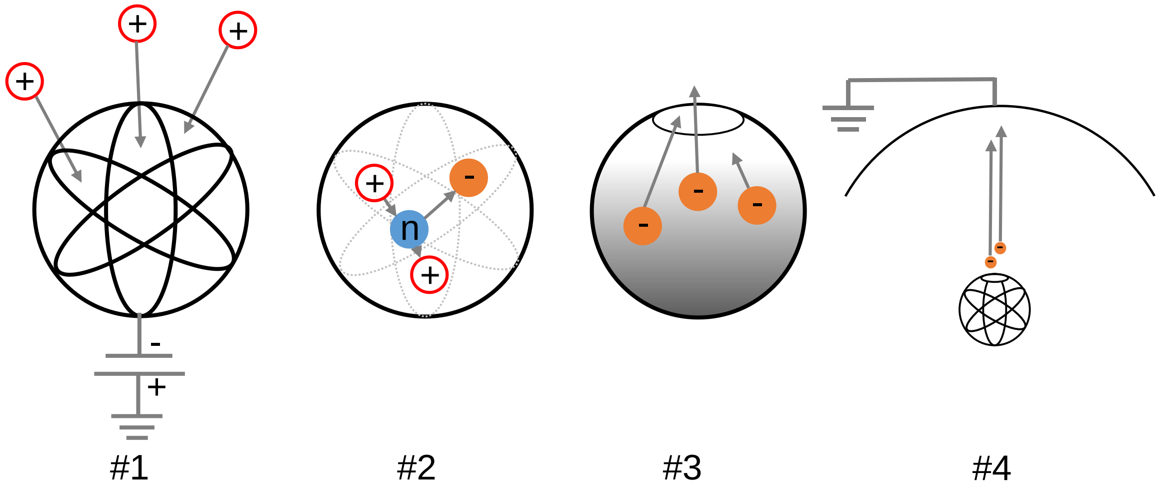

Figure 45. A very simple model for the formation of the plasma jet in an IEC device. #1) Ions are drawn toward a negatively biased central cathode grid. These ions can be produced through a DC glow discharge or other mechanism. #2) Ions circulate through the central grid region, causing collisional ionizations with background neutral atoms and secondary electron emission from grid collisions. #3) Low kinetic energy electrons born through these collisions experience a strong potential gradient accelerating through the grid asymmetry. #4) The plasma jet is formed by the electrons streaming out of the cathode grid to the grounded chamber wall.

The simple diagrammatic model of the IEC jet formation is summarized in Figure 45. The four processes shown represent the mechanism by which an electron beam will form from the grid asymmetry and accelerate toward the anode chamber wall. The first step is representative of a DC glow discharge or other ionization process that creates the initial plasma. The second step represents a key process in the formation of the jet which is different from that of star-mode. The collisions with the background neutrals and the grid wires themselves are primarily responsible for creating electrons inside the grid. This represents one rate limiting step in the amount of plasma current that can be extracted from the plasma jet. It will estimated and compared to experimental results. The third step is also critical and a unique property of IEC asymmetric grid. The collisionally-created electrons experience a net acceleration toward the asymmetry such that it represents an aperture for electrons to escape the interior of the grid. This will be demonstrated in the next chapter by COMSOL simulation of the electrostatic potentials. Finally, the fourth step represents a simple acceleration of the electron beam away from the grid by mutual repulsion.

9.1 COMSOL Simulations

A full 3-dimensional COMSOL simulation of the electrostatic potentials in the absence of plasma was performed as a useful tool in understanding the IEC device operation in jet-mode. Although plasma will change the potential during operation due to plasma sheaths around the various components, it useful to understand the general shape of the electrostatic potentials in the device. The simulation was created using the proper geometry of the IEC grid, outer vacuum vessel and gridded energy analyzer. The GEA was modeled as a series of 1.00 inch diameter circular grids with the same spacing as the experiment. The floating aperture was also modeled although this has no effect on the shape of the electric potential. In this simulation the collector plate has a floating potential, although in experiments, the plate is actually grounded. The orientation of the axes shown in Figure 46 was used for all COMSOL simulations. The red plane is the Y-Z plane which passes through the middle of the grid and GEA. The dashed line represents the Z-axis and is a radial line that points through the center of the IEC grid asymmetry (from which the jet exits) to the center-line of the GEA.

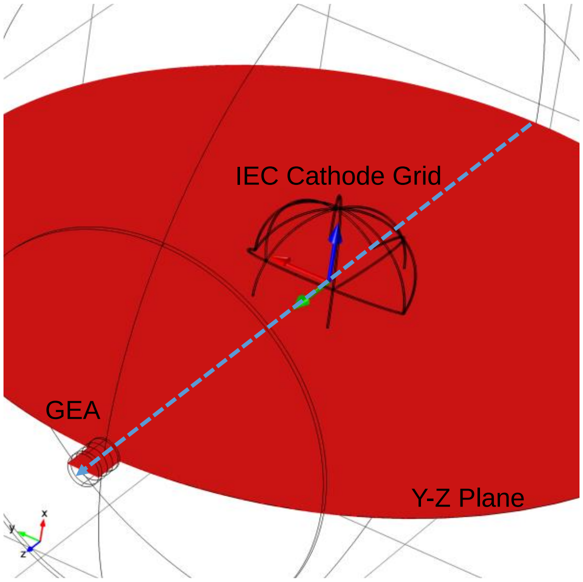

Figure 46. A 3-d image showing the orientation of the Y-Z plane (red) and Z-axis line (dashed line) used in the following COMSOL simulated data. The grid asymmetry points in the positive Z-direction toward the GEA.

The IEC grid potential was set to -5000 volts and the potential on the electron sweep grid was varied from -5000 volts to -1000 volts. The ion sweep grid was grounded for the simulations shown, however a series was also performed for ion sweep grid voltages up to +1000 volts, the maximum value achievable with our present experimental setup. Although the potential was fixed at a radial position of -0.063 meters since this was a grid wire in the geometry, the opposite side of the grid where the jet exits has a potential over 1000 volts less negative. This is shown in Figure 47 as a 2-dimensional slice plot in the Y-Z plane.

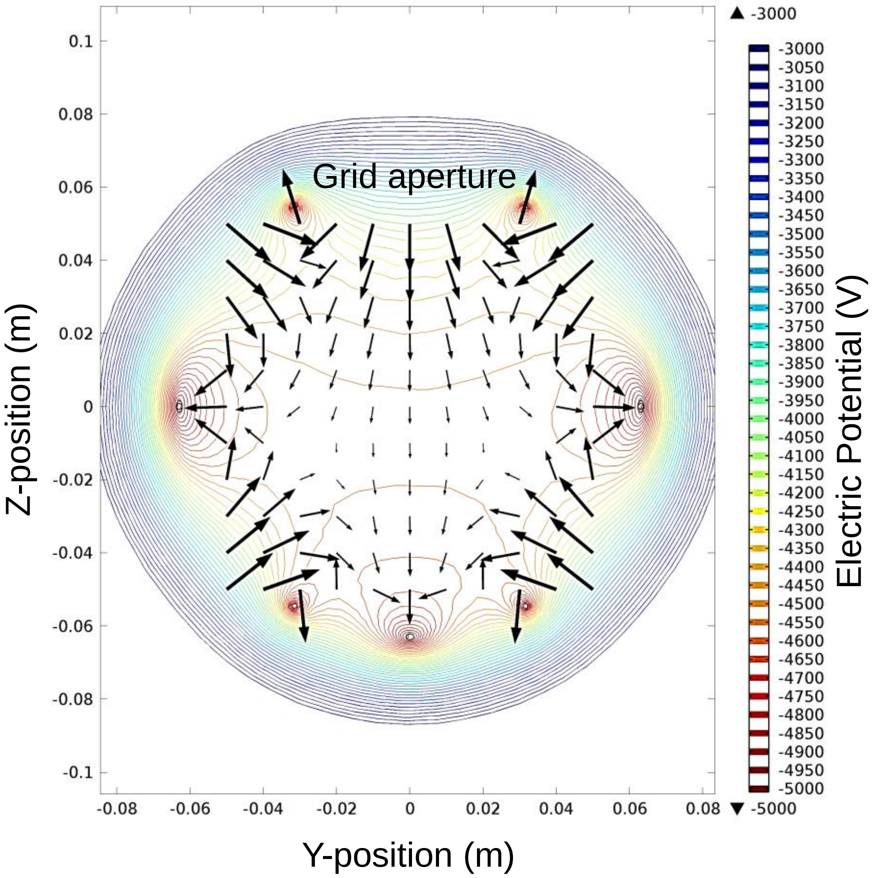

Figure 47. A 2-d slice of the Y-Z plane of contours of electric potential in volts. The black arrows show the direction and magnitude (log scale) electric field. The grid asymmetry creates an electric field inside the grid in the negative Z-direction. This means electrons inside most of the volume of the grid would accelerate in the positive Z-direction.

The electric potential shows an overall gradient in the positive Z-direction, i.e. normal to the asymmetry in the direction of the GEA. This means that the electric field inside the grid has a preferred direction in the negative Z-direction since it is a negative of the gradient of the potential. Therefore, an electron placed inside the grid will be accelerated out of the asymmetry. This will occur as long as the electron is not born too close to another grid opening or it will be accelerated out of that opening instead. This can be shown in another way by examining the Z-component of the electric field as in Figure 48.

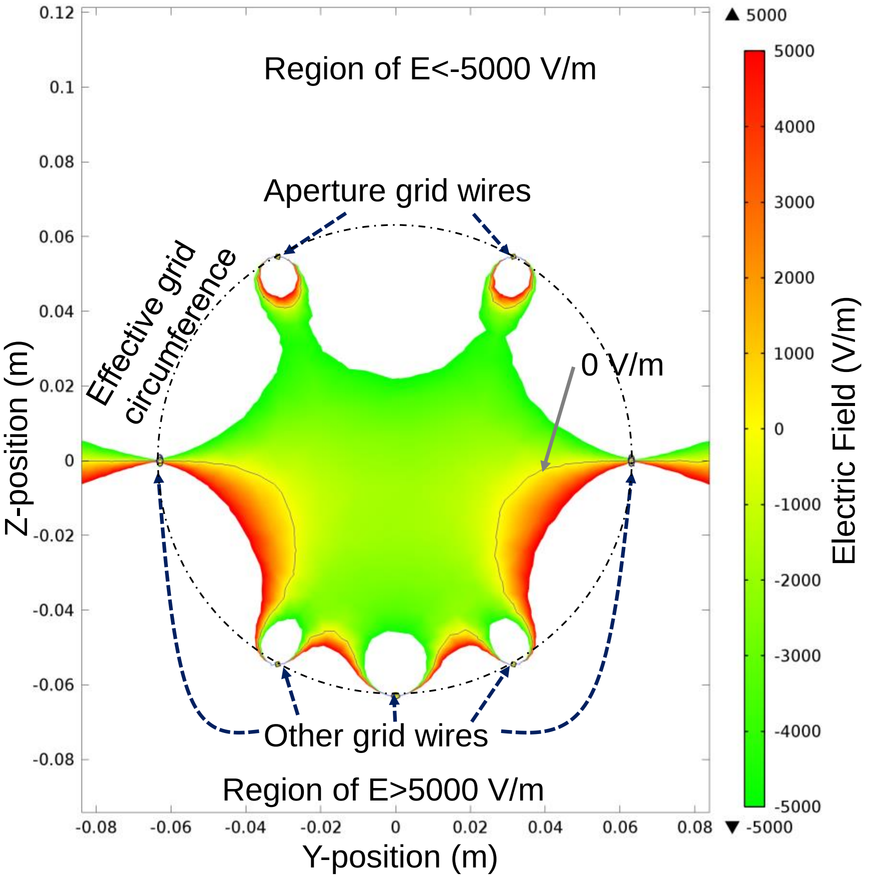

Figure 48. A Y-Z plane contour gradient plot showing the Z-component of the electric field inside the grid. The 0 V/m electric field contour line is shown in grey. Any green color means that an electron would have a Z-component of acceleration in the positive Z-direction with the reverse being true for red and orange hues. Most of the central area of the grid is green indicating electrons would strongly accelerate in the direction of the grid aperture.

The Z-component of the electric field inside the grid is generally strongly negative. This means that electrons born inside the grid would experience a large acceleration in the direction of the grid aperture. Once they escape the grid they will continue accelerating toward the grounded outer wall. Figure 49 shows that the magnitude of the GEA electron repeller grid has no discernable effect on the potential inside and near the IEC grid even if it is biased to the same potential as the IEC grid. This is due to the radial geometry; the areal size of the GEA in steradians is small compared to the entire area of the anode chamber wall. It does have significant effect however once the electron reaches within about 0.10 meters of the electron repeller grid. Again, because of the small area of the electron repeller aperture, the potential depresses very rapidly such that the electrons approaching the grid experience a very large loss in energy.

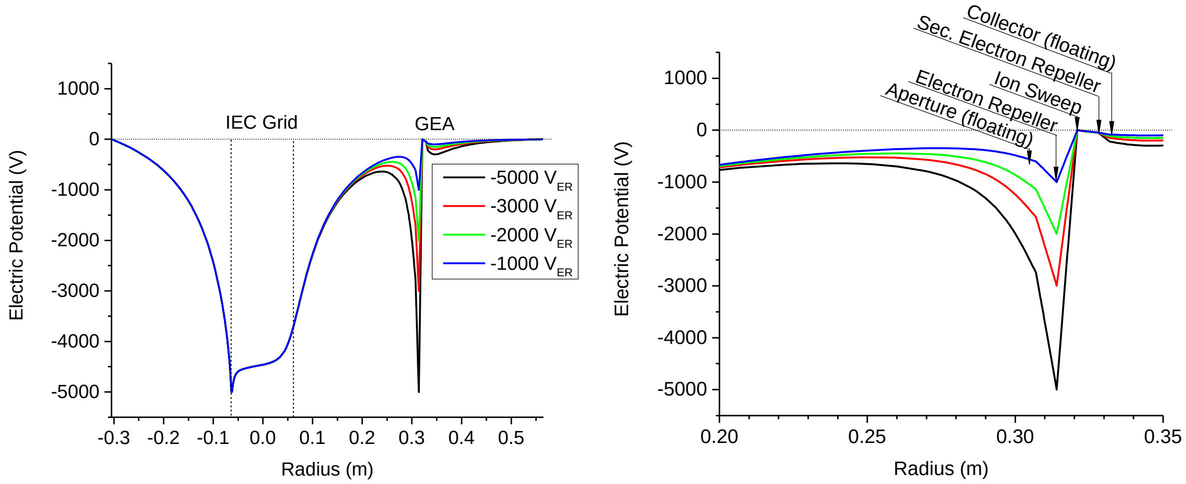

Figure 49. COMSOL simulations of the electric potential down the Z-axis of the IEC grid and gridded energy analyzer. (left) The radial extent of the grid is shown along with the general position of the GEA. (right) Zoomed in detail of the positions of the grids in the GEA diagnostic. Note that the potential peaks in between the IEC grid and the GEA electron repeller grid.

The COMSOL simulations have demonstrated a number of important features. First, there is a potential gradient inside the center of the IEC grid that sets up an electric field. In the following sections, this electric field will be used to create a computation model to predict the electron current drawn from the grid. In the next section, comparisons of the simulations with the experimental data suggest that the electrons in the jet are born at the aperture of the grid. This important result will again be corroborated by photographic evidence of the grid during jet-mode.

9.2 Expansion of Model for Prediction of Electron Energy Spectrum of the Jet

The simple model presented at the beginning of the chapter accounts for the formation of the plasma jet, however it does not offer much explanation as to the properties of that jet. In this section, several details of the model will be presented to offer greater predictive behavior of the properties with respect to changes in experimental parameters.

A comparison of the simulated electric potential with the electron energy spectra (Figure 38) provides evidence as to the physical location of source of the plasma jet. The large peak in the electron spectra occurs at a maximum energy of around 3500 electron-volts at the low pressure end. This energy matches the energy that an electron would gain if placed in the simulated potential at the IEC grid aperture. Assuming the absence of an energy loss mechanism such as electron-atom collisions, this suggests that the primary component of the electron-rich plasma jet consists of electrons born at the aperture.

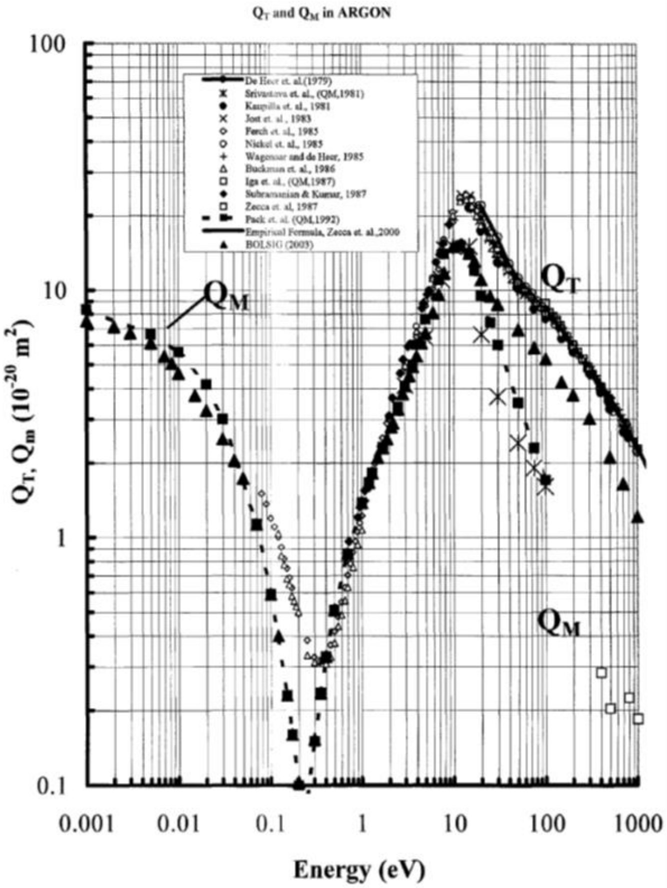

Figure 50. The total (Q_T) and momentum (Q_M) collisional cross sections for electrons in argon gas. The cross sections decrease exponentially with increasing electron energy above 10 electron-volts. This means that the high energy electrons exiting the grid would experience very few collisions with argon atoms or ions while accelerating toward the anode chamber wall. © 2004 IEEE [28]

To examine the validity of the assumption, the electron-atom collisional cross sections are shown in Figure 50 [28]. The total electron-atom collisional cross section decreases exponentially as the particle energy increases for electron energies over 10 electron-volts. The COMSOL simulations also indicate an extremely high electric field in the area of the aperture, as high as 40,000 volts per meter. This means that electrons born at the aperture accelerate extremely rapidly. If they do not undergo any collisions near the aperture, their energy kinetic energy would be high enough such that their now low collisional cross section would mean they would likely not experience any more collisions all the way to the chamber wall. This is known as electron runaway.

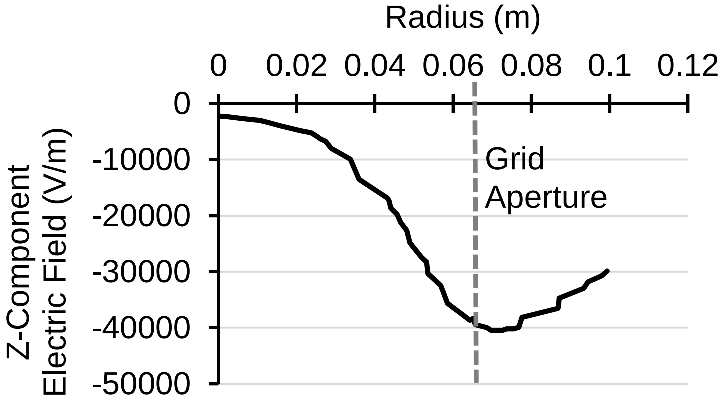

Figure 51. The Z-component electric field near the grid aperture produced by taking the derivative of simulated Z-component electric potential. The field is very high near the aperture of the grid.

This argument was made for the low pressure case. For higher pressure, the mean free path would be lower such that the electrons escaping the grid aperture would experience more frequent collisions resulting in scattering electrons out of the jet. This means a higher electric field is needed to induce thermal runaway and hence the birthplace of the electrons shifts radially outward. The onset of spray mode occurs when the maximum electric field is no longer high enough to produce a thermal runaway and a fanning out of the jet occurs as the electrons undergo collisions. This is the spray-mode described in the background chapter. Each time an electron scatters it loses some energy. It is expect then for the electron spectrum to have a wider peak for higher chamber pressures due to this energy spreading. Examining the experimental results for evidence of this spreading, it is possible to see this effect in Figure 35 in the I-V curves especially for 1.61 millitorr pressure where the current displays a graduate drop off rather than a sharp drop as for the other pressures. It is more difficult to however to see this effect in the electron energy spectra due to the way that the data was smoothed. The previous explanations have been summarized in Figure 52.

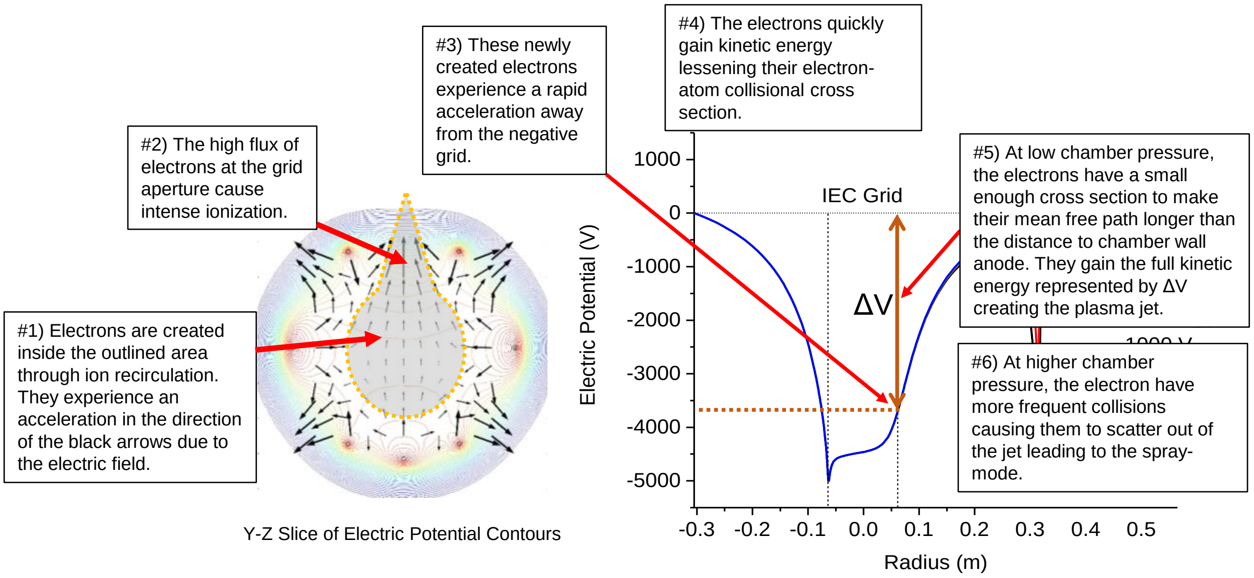
#1) Electrons are created inside the outlined area through ion recirculation. They experience an acceleration in the direction of the black arrows due to the electric field.

#2) The high flux of electrons at the grid aperture cause intense ionization.

#3) These newly created electrons experience a rapid acceleration away from the negative grid.

#4) The electrons quickly gain kinetic energy lessening their electron-atom collisional cross section.

#5) At low chamber pressure, the electrons have a small enough cross section to make their mean free path longer than the distance to chamber wall anode. They gain the full kinetic energy represented by ΔV creating the plasma jet.

#6) At higher chamber pressure, the electron have more frequent collisions causing them to scatter out of the jet leading to the spray-mode.

Figure 52. A summary model describing the formation location and the observed energy spectrum of the plasma jet. At the low end of the jet-mode pressure range when the grid voltage is -5000 volts, the observed electron energy spectrum has a sharp peak around 3500 electron-volts. Comparing to the COMSOL simulated electric potentials (#4), this means that the electrons in this peak were born at approximately the location of the cathode grid aperture/asymmetry.

9.3 Limiting Calculations

Two limiting calculations are presented in this section to provide further insight into the formation and propagation of the IEC plasma jet. The first calculation relates to the maximum number of electrons that are created inside the grid volume. This will give an estimate of the maximum plasma current expected to be measured with the Faraday cup. In the second calculation, the contribution to the total force for each of the species in the plasma, the electrons, ions and neutral particles will be explored. Using values from the previous calculation it will be shown that none of the species can provide a significant enough contribution to explain the origin of the experimentally measured force.

9.3.1 Maximum Expected Plasma Current

To calculate the maximum plasma current in the jet, it is assumed that it consists entirely of electrons born inside the volume of the grid. The problem is then one of estimating the number of electrons created per second inside the grid. If we treat the interior of the IEC grid as a solid spherical hollow cathode DC discharge, it is possible perform an analysis to compute the density. This analysis assumes that all electrons in the core region of the cathode escape to the remote anode to form the plasma current. A diagram explaining the configuration for the calculation is shown in Figure 53.

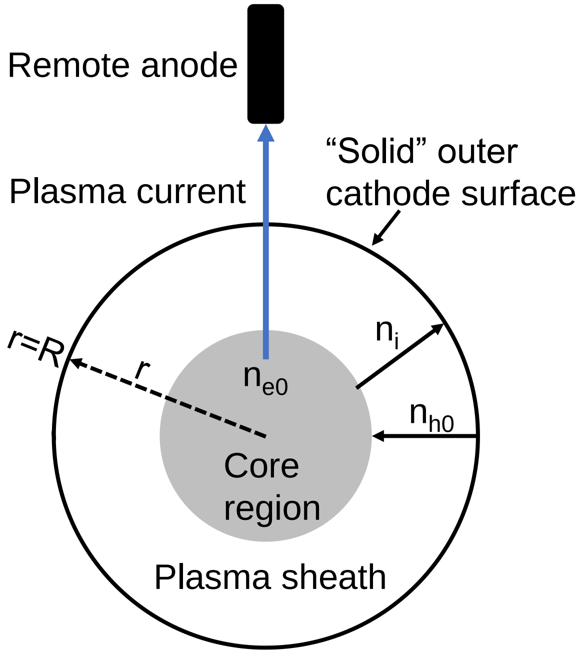

Figure 53. A diagram of the configuration used in the calculation of the maximum plasma current.

The analysis proceeds in a similar manner to the hollow cathode discharge model shown by Lieberman and Lichtenburg [24] except now the geometry necessitates the use of spherical coordinates. The plasma discharge is assumed to consist of hot electrons streaming across the plasma sheath into the core region, positive ions born in the core, and cold core electrons maintaining the plasma discharge. The hot electrons are assumed to be created through ion-cathode surface collisions through secondary emission. It is assumed that all cold electrons are accelerated by an electric field E_0 inside the core region and produce the plasma current. The analysis begins with the plasma diffusion equation (Lieberman 5.2.30),

$$-D\nabla^2 n = G_0 \tag{9}$$

Transforming the equation to spherical coordinates and applying the necessary source term G_0 gives,

$$-D_a \frac{1}{r^2}\frac{d}{dr}\left(r^2 \frac{dn_i}{dr}\right) = K_{iz} n_g n_{h0} \tag{10}$$

where n_{h0} and n_g are the hot electron and neutral gas densities, K_{iz} is the ionization rate coefficient for the hot electrons and D_a is the ambipolar diffusion coefficient for the cold electrons. Assuming a uniform hot electron density n_{h0} and integrating (10) gives

$$\frac{dn_i}{dr} = \frac{K_{iz} n_g n_{h0}}{3D_a} r + c_1 \tag{11}$$

The constant of integration is found by assuming the ion flux at the surface is equal to the hot electron flux. Therefore $c_1 = dn_{h0}/dr$. Integrating a second time and assuming the ion density is equal to the cold electron density at the center $n_i = n_{e0}$, gives

$$n_i = -\frac{K_{iz} n_g n_{h0}}{6D_a} r^2 + n_{h0} + n_{e0} \tag{12}$$

Setting the boundary condition that $n_i = n_{h0}$ at $r = R$ we find

$$n_{e0} = n_{h0} \frac{K_{iz} n_g R^2}{6D_a} \tag{13}$$

Substituting n_{h0} into the derivative of (12) gives a formula for the ion flux at the surface of the cathode.

$$\Gamma_i(R) = -D_a \frac{dn_i}{dr}\bigg|_{r=R} = 2D_a n_{e0}/R \tag{14}$$

The current provided to the cathode surface sets the cold electron plasma density in in the core by

$$I_{DC} = 2 \times 4\pi R^2 e\Gamma_i \tag{15}$$

Where the first factor of 2 accounts for the cathode current used to create plasma on both sides of the cathode. Substituting (14),

$$n_{e0} = \frac{I_{DC}}{16\pi ReD_a} \tag{16}$$

For the model to be complete we assume that the flux of the ions in the sheath must be equal to the flux of hot secondary electrons weighted by the number of secondaries per ion, known as the secondary electron coefficient γ_{SE}.

$$\Gamma_i(R) = \Gamma_h(R)/\gamma_{SE} \tag{17}$$

The current density at the center point (14.4.12) is given by

$$J_0 = en_{e0}\mu_e E_0 \tag{18}$$

where μ_e is the electron mobility and E_0 is the electric field strength at the aperture that draws out the electrons from the grid. Plugging in (16) for the center point electron density gives

$$J_0 = \frac{\mu_e E_0}{16\pi RD_a} I_{DC} \tag{19}$$

Values for the electron mobility and ambipolar diffusion coefficients can be estimated using Lieberman (5.1.4) and (5.1.5)

$$\mu_e \approx \frac{e}{mn_g K_{el}} \;\; [cm^2/(V\cdot s)], \quad D_a \approx \frac{e\lambda_i}{M\bar{v}_i} T_e \;\; [cm^2/s] \tag{20}$$

An estimate of the ion mean free path λ_i and the neutral gas density n_g are given by Lieberman (3.5.7) and (2.3.18) as simple functions of pressure by

$$\lambda_i \approx \frac{1}{330p} \ [cm], \qquad (p \ in \ Torr) \tag{21}$$

$$n_g \approx 3.250 \times 10^{16} \ p \ [cm^{-3}], \qquad (p \ in \ Torr) \tag{22}$$

Computing λ_i and n_g for a pressure of 1.5 mTorr gives λ_i=2 cm (0.02 m) and n_g=4.88 x 10^{13} cm^{-3} (4.88 x 10^{19} m^{-3}).

It should be noted that this analysis assumes that the ions inside the core region have low energies having been created due to cold electron-neutral collisions. It does not account for fast ions that are streaming through the grid. The mean free path would be longer for these ions since the scattering cross sections is lower at high energies. The collision rate coefficient for elastic scattering in argon gas at low ion energy is estimated by (3.5.6) as $K_{el} \approx 10^{-13}$ m^3/s. However it is several times larger for ion energies in the keV range as we could expect for the streaming ions. However, it is difficult to estimate the number density of these ions so they will be ignored.

The two remaining missing quantities to compute the ambipolar diffusion coefficient are the average ion velocity and the cold electron temperature. A reasonable value of the cold electron temperature is given by Lieberman as 0.5 eV. If the cold ion temperature is assumed to then be 0.05 eV, since they are created from the cold background gas, then the average ion velocity in the core is computed using

$$\overline{v_i} = \left(\frac{8kT_i}{\pi M}\right)^{1/2} \tag{23}$$

to be 430 m/s. Plugging values in for the ambipolar diffusion coefficient and the electron mobility gives D_a = 640,000 m^2/s and μ_e = 36,000 $m^2/(V \cdot s)$. While these numbers are high, the pressure in the system is very low compared to most laboratory plasmas, just 1.5 mTorr in this calculation.

We can also now calculate the expected cold electron density at the core center from (16). Using a cathode grid current I_{DC} of 20 mA, we find an electron density of ~6.2x10^{10} m^{-3}.

The current drawn out of the jet is the center point current density multiplied by the cross sectional area of the core region. We can estimate the size of the core based on visual observations (see Figure 57, page 89) of the plasma to have a diameter of approximately 1/3 of the grid diameter. This means that area, $A_c \approx 3.5\text{x}10^{-4}$ m^2.

$$I_{jet} = A_c J_0 = \frac{\mu_e E_0 A_c}{16\pi R D_a} I_{DC} \tag{24}$$

It is useful to know the fraction of the supplied DC grid current that makes it into the jet for this model. We assume a value of $E_0 \approx 2000$ V/m from the Z-component electric field from the COMSOL simulations. Plugging in all the computed values for the constants we find that the jet current represents about a 0.098 fraction (or about 10%) of the total input current. Because the current is dependent on the square of the radius of the core, if we consider the entire volume of the grid to be the core region, the fraction jumps .89 or nearly 90%.

Another calculation of the maximum plasma current can be made by examining the Child-Langmuir space charge limited current. To find this current, one must solve the spherical Poisson's equation using the ion energy and flux conservation equations given by

$$\frac{1}{2} M u^2(r) = -e\Phi(r) \tag{25}$$

$$e n(r) u(r) = J_0 \tag{26}$$

The mathematical formulation for the total current density limit for planar geometry is given by Lieberman (6.3.12) [24] as

$$J_0 = \frac{4}{9}\epsilon_0 \sqrt{\frac{2e}{m}} \frac{V^{3/2}}{s^2} \tag{27}$$

where *s* is the distance between the electrodes and V is the voltage through which the electrons are accelerated. Since we are considering the current being drawn out only through the aperture of the grid, it is fair to use the planar equation. This formula can be compared to data collected by the Faraday cup shown in Figure 31. That data was plotted as current density at the aperture of the diagnostic, not the grid aperture. The current drawn out of the grid aperture is plotted in Figure 54 for various size grid aperture radii. From previous experimental results it was found that the energy gained by the jet electrons is approximately half of the full grid voltage. Therefore we choose V in (27) to be half the grid voltage. If we consider only the experimental data greater than -3000 V, an aperture size of 5 mm in radius shows the best functional fit to the data. This aperture size is fair approximation given the physical size of the bright ionization region witnessed in the experiment. (See Figure 57). For grid voltages less than -3000 V, it is difficult to say if the jet-mode was even established. The Child-Langmuir space charge maximum current provides a good approximation to the current drawn from the grid.

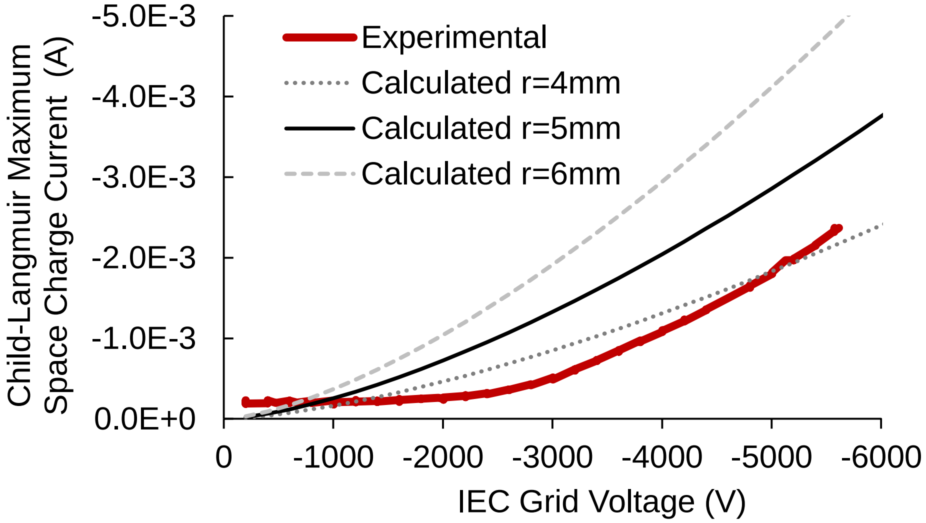

Figure 54. The Child-Langmuir maximum space charge has the same functional dependence above -3000 volts grid voltage for a grid aperture radius r of 5 millimeters similar in visual size to the bright cone of plasma at the aperture seen in the experiment.

9.3.2 Maximum Expected Force of the Plasma Jet

The goal of this section is make some estimates of the maximum force we can expect from the plasma jet measured by the piezoelectric force sensor. The kinetic theory of gases explains that each particle hitting a surface produces a momentum gain by a surface and loss by a particle which creates a pressure when averaged over a number of particles. There are several sources of pressure in the plasma jet including the electrons, ions and neutral particles. Each has a different pressure on the surface corresponding to how the particle reacts with the surface.

It is assumed that any neutral particles in the jet have a low enough energy to disregard physical sputtering such that the momentum transfer is completely inelastic. This means the momentum transferred to the surface for each neutral particle collision with mass M_g and velocity v_z is

$$\Delta p_{g,z} = 2M_g v_{g,z} \tag{28}$$

The force on the surface is Δp/Δt so

$$F_g = \frac{\Delta p_{g,z}}{\Delta t} = \frac{2M_g v_{g,z}}{\Delta t} \tag{29}$$

The quantity Δt represents the time between each particle collision with the surface and can therefore be written as the inverse of the collision frequency as

$$F_g = \frac{2M_g v_{g,z}}{1/\nu} = 2M_g n_g \sigma v_{g,z}^2, \qquad \nu = n_g \sigma v \tag{30}$$

In this case the cross section σ does not represent an atomic collision cross section but the area of the plasma striking the plate. Therefore the variable is renamed, $\sigma = A_p$.

$$F_g = 2M_g n_g A_p v_{g,z}^2 \tag{31}$$

For an electron the result is slightly different. It is assumed that when an electron strikes the surface it does not rebound but is absorbed as in a perfected inelastic collision. Therefore the factor of 2 is eliminated and

$$F_e = M_e n_e A_p v_{e,z}^2 \tag{32}$$

Because the energy of the electrons in the plasma jet is so high (~3 keV), we need to check to see if the relativistic momentum should be used instead of the standard expression. The relativistic expression of momentum is

$$p = \gamma m_0 v = \frac{m_0 v}{\sqrt{1 - \frac{v^2}{c^2}}} \tag{33}$$

Assuming that a 1% change in the momentum is enough to consider using the relativistic form, that means that $\gamma = 1.01$. We can calculate the energy threshold by using the relativistic kinetic energy

$$KE = (\gamma - 1) m_0 c^2 \tag{34}$$

Plugging the values for an electron we find that relativity becomes a concern when the electron energy exceeds ~5.1 keV. The values used in this calculation are close but we can safely ignore relativity.

For an ion we assume a neutralization at the surface such that the mass of the rebounding particle is slightly higher. This momentum difference is negligible though since the total ion flux is expected to be small in comparison to electron flux to the surface and as such it will be ignored. The ion pressure has the same form as the neutral gas pressure

$$F_i = 2 M_i n_i A_p v_{i,z}^2 \tag{35}$$

The total force on the plate surface is then written as the sum of these three forces,

$$F_{tot} = F_g + F_e + F_i \tag{36}$$

It may be expected that the electron beam would contribute negligible momentum and may be neglected but it is important to check this assumption. From the previous sub-section we have an estimate of the electron density and we can compute $v_{e,z}^2$ using (23) by the realization that the average velocity accounts for three degrees of freedom. For a beam we only desire the z-direction so we need to divide this value by 3. The temperature of the electrons for this calculation is 2700 eV based on the electron energy spectrum experimental results and extrapolated for 1.5 mTorr (which was used to in all calculations in the previous sub-section). This gives the average z-velocity for the electrons in the jet striking the plate as 1.14 x 10^7 m/s. We assume the size of the A_p based on the size of the aperture to the diagnostic sub-chamber to be 9.5×10^{-4} m^2. Plugging in the values to (32) yields a force of only 7 x 10^{-9} N. The electron momentum transfer to the plate is therefore not significant at these energies.

To make a calculation on the maximum momentum expected in the plasma jet the source of the ions must be considered. It could be assumed that the ions that could impact the grid come from inside the grid in which case information on the number density of core ions is needed. Although it would appear that the potential well structure does not support this assumption, it is possible that the there is a double well potential structure inside the cathode grid. This would be similar to those experimentally found in symmetric gridded IEC devices and that a virtual cathode created by the high electron density near the aperture may act to draw ions out of the grid [29] [30]. However this is beyond the scope of the model presented in this dissertation. Instead a different approach will be used that relies on the space charge created by the high energy electron-rich jet after it has passed through the aperture of the diagnostic sub chamber and is at essentially zero potential. These electrons ionize neutral argon gas particles which fall into the plasma sheath. We will assume for a maximum case that all neutral gas particles in this volume become ionized and fall into the plate with a velocity of $v_{i,z}$. Using (35) we can then estimate the force on the plate as a function of the ion velocity. A plot of this equation is shown Figure 55.

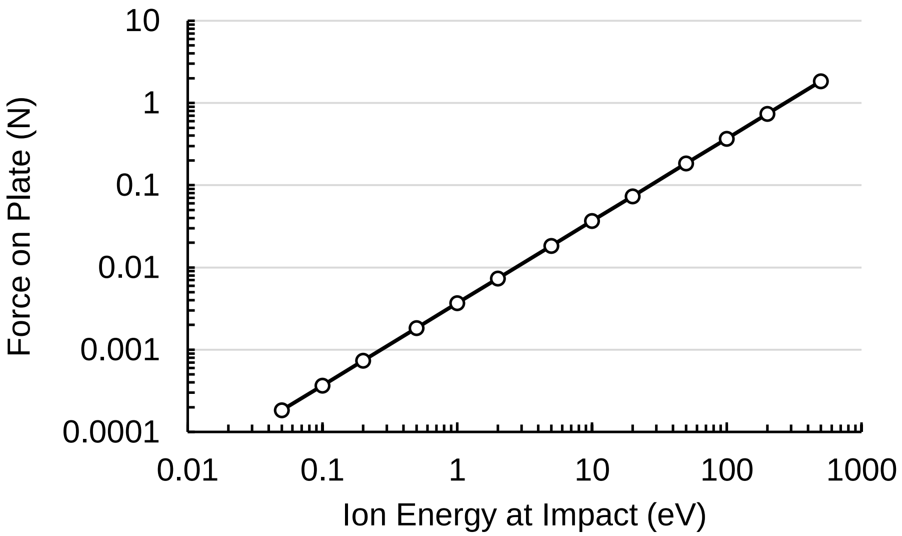

Figure 55. If the electron beam results in complete ionization of the neutral gas, the force on the plate would be within the range of the experimental results for an ion energy of around 1 eV.

Clearly it is not realistic to expect that complete ionization would occur so to examine the fraction of ionization that may occur we use ionization rate provided by Lieberman (3.1.8)

$$\nu_{iz} = n_g \sigma_{iz} v \tag{37}$$

The velocity is that of the electron and the σ_{iz} is the electron-argon ionization cross section. Extrapolating the cross section from Raju shown in Figure 56, the cross section is estimated to be 4 x 10^{-21} m^2 at 2700 eV electron energy. Computing using (37) gives an ionization rate of merely 2.3 x 10^6 s^{-1}. In Figure 55 is was assumed that the density was that of the neutral density in the range of 10^{19}. Therefore if proper ionization is considered the force on the plate would be some 15 orders of magnitude lower than the plot. This is fact much lower than the force generated by the electrons. Ions generated using these assumptions cannot be the cause of the apparent measured force on the grid.

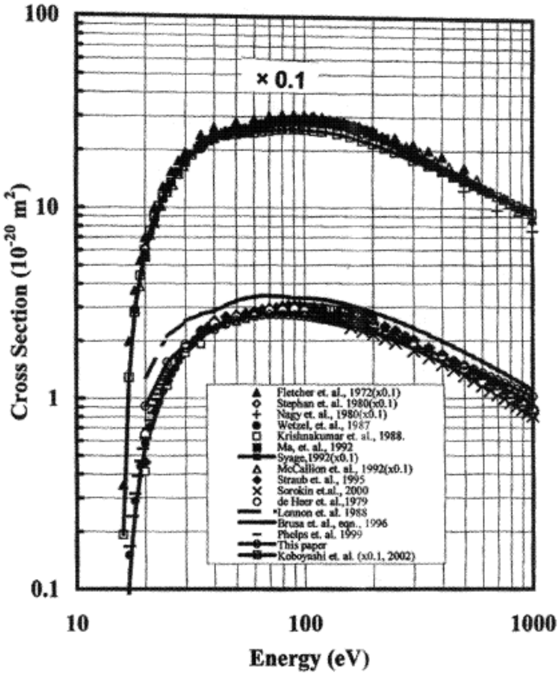

Figure 56. Electron-argon ionization cross sections compiled by Raju. The large amount of data has been split for clarity. The top curve should be multiplied by 0.1. © 2004 IEEE [28]

The force by the neutral particles can be examined in the same way as the ions. If an estimate is generated of the amount of fast neutral particles as a fraction of the total neutral gas density, then Figure 55 can be used directly by multiplying by the fraction. It is clear that each order of magnitude decline in the fraction represents an order of magnitude decline in the force on the plate. Since we would expect the number of fast neutral particles to represent a very small fraction of the neutral gas density, it is again not possible that the neutral particles would contribute significantly to the force. Since it has been demonstrated that none of the three components of the plasma jet, the electrons, ions and fast neutral particles seem to carry enough pressure to cause the experimentally measured force on the plate, it remains an open question as to the origin of the experimentally measured force.

9.4 Additional Explanation of Experimentally Observed Phenomena

The refined model from chapter 9.2 can provide additional explanation for some of the experimentally observed phenomena. This section will explain some of the visual features of the plasma jet observed in the experiment. A photographic side-by-side comparison of the jet-mode and spray-mode are shown in Figure 57. The bright cone that is always visible at the grid aperture can now be explained by the model as a region of intense ionization caused by electrons squeezing through the high electric field region of the aperture. The location of this cone shifts radially outward as the chamber pressure increases. Although the model does not account for this shift, it does predict that location of the cone represents the location where most of the electrons are created that end up in the jet. Since the cone moves radially outward at higher pressures, this means that the peak in the electron energy spectrum should shift to a lower kinetic energy. This is due to the extremely sharp drop in the potential with respect to radial distance. Therefore even a shift of a few millimeters can change the peak of the spectrum by thousands of volts. This is exactly what we observe experimentally at higher pressures.

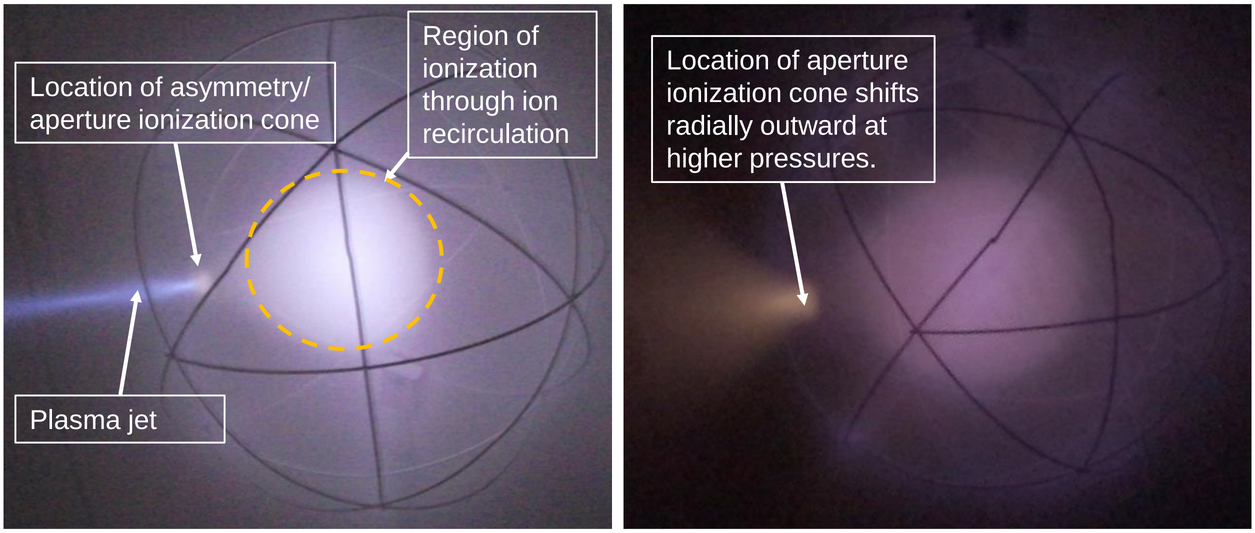

Figure 57. Examining photographs taken of the IEC operating under jet-mode (left) and spray-mode (right) reveal several characteristics that can be explained by the model.

10.0 Conclusions

The goal of this Ph.D. dissertation work was to provide an understanding of the unique phenomenon of an IEC jet-mode plasma. This involved the construction, calibration and testing of the experimental apparatus and all of the related plasma diagnostics. The operating parameter space for jet-mode was explored and it was found to only exist in a narrow pressure range of 1.3 to 2.35 millitorr. It was demonstrated that use of an RF plasma source increases the controllable parameter space by decoupling to a certain degree, the IEC grid voltage from the grid current.

The measurements and simulations untaken in this work explored the properties of the jet-mode plasma and allowed for the creation of a model that explains its formation and propagation. The IEC plasma jet consists primarily of a high energy electron beam created at the aperture of the cathode grid. Simulations indicate that electrons born inside the cathode grid experience an electric field force that accelerates them toward the aperture. At low pressure, these electrons gain enough energy due to the high electric field near the grid that they do not undergo many collisions as they accelerate toward the anode chamber wall. This is due to the greatly decreased electron-atom collisional cross section for electrons at high kinetic energies. This intense beam of electrons is what we know as jet-mode. When the pressure is increased, the electrons have a shorter mean free path leading to increased electron-atom collisions. This acts to scatter electrons out of the jet before they can reach the anode. This is what is known as spray-mode.

Each diagnostic allowed a unique measurement of some aspect of the plasma jet. In addition the spherical probe was used to gain an understanding of how the RF plasma source couples ions it produces into the IEC grid. The Faraday cup produced two sets of data, the total plasma current and with the addition of a temperature sensor a measurement of the thermal power transferred to the cup by the jet. The total plasma current was utilized in the creation of the model of the IEC jet-mode system. The thermal power measurements allowed calculation of the total efficiency of the IEC device in transferring power into the jet. This was found to be around 20% for all glow discharge conditions and about 1-2% when the RF plasma source was utilized. The gridded energy analyzer was used to measure electron energy spectra. This data was compared to the COMSOL simulation to determine that the peak in the electron energy spectra indicated that the majority of the electrons in the jet were born at the grid aperture.

As a result of this work a more thorough understanding of the IEC jet-mode is available. This work will provide a launching point for additional investigation to eventually utilize this device for electric space propulsion. Although it has been shown in this work that the most basic version of an IEC jet-mode device does not lend itself to immediate use as an electric propulsion device, the beneficial attributes of the device such as the intensity and energy of the electron jet make it attractive for further study.

11.0 Future Work

There are several opportunities for future study on the topic of the IEC jet-mode. This chapter will present several areas that warrant continuing and new investigation as a direct result of the conclusions of this work. There are several questions presented throughout this work that we were unable to answer with the diagnostics and capabilities available. Additionally a new line of investigation is proposed to allow use of the unique properties of the jet-mode to be used for electric space propulsion.

11.1 Open Questions to Answer

The first part of any future work on studying the IEC jet mode should focus on answering a number of open questions from this work. The first question relates to the ion energy spectra. Because of design flaws related to the gridded energy analyzer, it was not possible to collect a true ion spectra. In order to remedy this issue, there are two possible directions to explore. The first is to install the plasma aperture to the diagnostic sub-chamber such that it can once again be differentially pumped. This will greatly decrease the p-d factor in the breakdown curve meaning it will be more difficult to breakdown a plasma inside the diagnostic. Of course, this will also come with a corresponding lowering of the signal from the jet however the signal-to-noise ratio is high enough that even a loss of 10x to 100x signal strength shouldn't pose a significant issue. The other possible remedy is to decrease the spacing between the electron repeller and ion sweep grids as another mechanism to decrease p-d. This would involve machining a new Macor ceramic spacer plate. To prevent sputtered material from depositing on the interior walls of the space plate, the floating aperture should be made smaller.

The second open question relates to the plasma properties inside the grid. It was originally intended to take spectroscopic measurements inside the core using borrowed equipment however it was discovered that this equipment did not possess a fine enough full-width half-maximum precision to obtain line spectrum that could be used to compute the electron temperature and density in the core. It should be possible to make spectroscopic measurements on the core region if the proper equipment could be obtained. If not, using plasma probes may provide some useful information if the data could be properly interpreted. Analyzing this data will be difficult due to the highly non-Maxwellian nature of the energy spectrum such that standard techniques do not apply.

The final open question is how it may be possible to increase the efficiency of the device. It was shown that the efficiency of the jet-mode at low pressure is approximately 20%. While enhancing this efficiency was not explored beyond showing that an external ionization source does not improve the properties, there are some aspects that could be investigated that could help. The first thing that is needed before any experiments should be performed is to produce a more robust model of the processes inside the grid using theory and modeling. Experimentally then, it might be possibly to control the electron density inside the grid by using an electron injection technique. This could be in the form of a thoriated tungsten grid or electron emitters placed just inside the grid using electron field emission or some other means. Because the IEC jet-mode has been demonstrated in this work to be an electron dominated phenomenon, controlling the density of the electrons inside the grid seems like the most logical way to control the efficiency as well as other properties of the device.

11.2 Expansion of Diagnostic Capability

Enhancing the diagnostic capability will allow for more accurate and precise measurements of the various jet-mode properties such at the electron and ion energy spectra. A significantly more precise instrument for measuring electron and ion spectra is already present in the HIIPER Space Propulsion Laboratory. It is called a Spherical Electrostatic Analyzer (SEA). This device is on loan from the Air Force Research Laboratory and offers the capability to select for specific energies in the spectrum through its special design. This means the spectrum is recovered directly by sweeping the gating energy. This is contrast to the GEA in which the data must be differentiated to recover a spectrum. In order to get this instrument functioning, some additional vacuum components are required to connect it in place of the present diagnostic sub-chamber. The multi-channel plate detector also needs to be replaced as these devices develop cracks when they absorb moisture from the air.

One enhancement to the data collection to eliminate noise is already being undertaken as this dissertation is being finalized. A Faraday room has being constructed in the laboratory that will allow better measurements made with much less electromagnetic noise. This was generally a problem for any measurements made using the RF generator and especially when it was run in helicon mode. Any future work on this device will benefit greatly from lower noise measurements.

The final focus for the diagnostics should be on the improvement of the plasma force sensor. Care must be taken to eliminate the effects of the radiometric force if one desires to make an accurate measure of the thrust on the plate. It is suggested then to eliminate this force but taking the plate and diagnostic sub-chamber out of the transitional flow regime by reinstalling the plasma aperture at the entrance to the sub-chamber. This would greatly decrease the pressure inside the sub-chamber and prevent the effects of the imbalance in gas temperature seen in this work. Additionally, the size of the plate should be decreased in order to minimize the edge effects that are very strong when the plate diameter is a significant fraction of the sub-chamber diameter.

11.3 Negative Ions and Nanoparticle Injection for HIIPER Thrust

It was stated in the introduction that the major interest in studying the IEC jet-mode is to apply its design to a new type of electric space propulsion. The findings in this dissertation mean that it may not be possible to directly implement it this capacity but there are still lines of research that could be explored to eventually realize this goal. One such method involves the use of negative ions. Boris et. al. showed that IEC devices have the capacity to produce large numbers of negative ions [31]. Since a negative ion would behave very similarly to an electron in the electric potential well of the IEC grid, this may provide the large momentum flux desired of HIIPER. Since electric propulsion is the goal, not fusion, we are free to choose any highly electronegative gas in place of argon used throughout this study. Another possible mechanism to use the unique jet-mode structure is to inject nanoparticles such as fullerenes. The molecules would rapidly gain a multiple negative charge state and act as very large negative ions. We believe these ideas warrant further investigation in light of the discoveries in this dissertation on the modeling of the formation and propagation of the IEC jet-mode.

12.0 References

[1] G. H. Miley and J. Sved, "The IEC star-mode fusion neutron source for NAA - status and next-step design," *Applied Radiation and Isotopes,* vol. 53, no. 4-5, pp. 779-783, 2000.

[2] Y. R. Shaban and G. H. Miley, "High Neutron Yield, Steady State, Below Breakdown PV Regime in Inertial Electrostatic Confinement Device".

[3] F. F. Chen, "Plasma Ionization by Helicon Waves," *Plasma Physics and Controlled Fusion,* vol. 22, no. 4, pp. 339-364, 1991.

[4] F. F. Chen, "Experiments on helicon plasma sources," *Journal of Vacuum Science and Technology,* vol. 10, no. 4, pp. 1389-1401, 1992.

[5] T. Lafleur, C. Charles and R. W. Boswell, "Ion beam formation in a very low magnetic field expanding helicon discharge," *Physics of Plasmas,* vol. 17, p. 043505, 2010.

[6] F. F. Chen, "Permanent magnet helicon source for ion propulsion," *IEEE Transactions on Plasma Science,* vol. 36, no. 5, pp. 2095-2110, 2008.

[7] K. Toki, S. Shinohara, T. Tanikawa and K. Shamrai, "Small helicon plasma source for electric propulsion," *Thin Film Solids,* Vols. 506-507, pp. 597-600, 2006.

[8] M. P. Reilly, *Three Dimensional Imaging of Helicon Wave Fields Via Magnetic Induction Probes,* Urbana: Ph.D. Dissertation, University of Illinois, 2009.

[9] G. R. Piefer, *Performance of a Low-Pressure, Helicon Driven IEC 3He Fusion Device,* Madison: Ph.D. Dissertation, University of Wisconsin, 2006.

[10] J. Nadler, E. Yoder and C. Hunsicker, "Experimental Investigation of Unique Plasma Jets for Use as Ion Thrusters," *American Institute of Aeronautics and Astronautics,* p. 2570, 1998.

[11] G. Chen, "Analysis of energy balance in a helicon coupled to an inertial electrostatic confinement device," Univerisity of Illinois, Urbana, 2013.

[12] R. A. Pitts, R. Chavan, S. J. Davies, S. K. Erents, G. Kaveney, G. F. Matthews, G. Neill, J. E. Vince and I. Duran, "Retarding field analyzer for the JET plasma boundary," *Review of Scientific Instruments,* vol. 74, no. 11, pp. 4644-4657, November 2003.

[13] S. L. Meredith, *Construction of a gridded energy analyzer for measurements on ion energy distribution in the versatile toriodal facility,* Boston: M.S. Thesis, Massachusetts Institute of Technology, 1998.

[14] J. Khachan, D. Moore and S. Bosi, "Spatial distribution of ion energies in an inertial electrostatic confinement device," *Physics of Plasmas,* vol. 10, no. 3, pp. 596-599, 2002.

[15] L. B. Leder and J. A. Simpson, "Improved electrical differentiation of retarding potential measurements," *The Review of Scientific Instruments,* vol. 29, no. 7, pp. 571-574, July 1958.

[16] Burr-Brown Corporation, *ISO120, ISO 121 Precision Low Cost Isolation Amplifer Specification Sheet,* 1992.

[17] Texas Instruments Incorporated, *INA110 Fast-Settling FET-Input Instrumentation Amplifier Specification Sheet,* 2005.

[18] D. Chavers and F. R. Chang-Diaz, "Momentum flux measuring instrument for neutral and charged particle flows," *Review of Scientific Instruments,* vol. 73, no. 10, pp. 3500-3507, 2002.

[19] B. W. Longmier, B. M. Reid, A. D. Gallimore, F. R. Chang-Diaz, J. P. Squire, T. W. Glover, G. Chavers and E. A. Bering III, "Validating a Plasma Momentum Flux Sensor to an Inverted Pendulum Thrust Stand," *Journal of Propulsion and Power,* pp. 746-752, 2009.

[20] B. Longmier, E. Bering III, B. Reid, A. Gallimore, J. Squire, T. Glover, F. R. Chang-Diaz and M. Brukardt, "Hall Thruster and VASIMR VX-100 Force Measurements Using a Plasma Momentum Flux Sensor," in *47th AIAA Aerospace Sciences Meeting*, Orlando, Florida, 2009.

[21] A. Krishnamurty, *Development and Characterization of an Inertial Electrostatic Confinement Thruster,* Urbana: M.S. Thesis, University of Illinois, 2013.

[22] L. Ledernez, F. Olcaytug, H. Yasuda and G. Urban, "A modification of Paschen law for Argon," in *29th ICPIG*, Cancun, 2009.

[23] D. N. Ruzic, Interviewee, [Interview]. 1 November 2013.

[24] M. A. Lieberman and A. J. Lichtenburg, Principles of Plasma Discharges and Materials Processing, Hoboken: John Wiley & Sons, Inc., 2005, pp. 551-555.

[25] S. F. Gimelshein, N. E. Gimelshein, A. D. Ketsdever and N. P. Selden, "Analysis and Applications of Radiometric Forces in Rarefied Gas Flows," in *27th International Symposium on Rarefied Gas Dynamics*, Monterey, 2010.

[26] M. Scandurra, F. Iacopetti and P. Colona, "Gas kinetic forces on thin plates in the presence of thermal gradients," *Physical Review E,* vol. 75, p. 026308, 2007.

[27] D. J. Rader, W. M. Trott, J. R. Torczynski and J. N. G. T. W. Castaneda, "Measurements of Thermal Accomodation Coefficients," Sandia National Laboratory SAND2005-6084, Albuquerque, 2005.

[28] G. G. Raju, "Electron-atom Collision Cross Sections in Argon: An Analysis and Comments," *IEEE Transactions on Dielectrics and Electrical Insulation,* vol. 11, no. 4, pp. 649-673, 2004.

[29] R. A. Nebel, S. Stange, J. Park, J. M. Taccetti, S. K. Murali and C. E. Garcia, "Theoretical and experimental studies of kinetic equilibrium and stability of the virtual cathode in an electron injected inertial electrostatic confinement device," *Physics of Plasmas,* vol. 12, p. 012701, 2005.

[30] Y. Gu and G. H. Miley, "Experimental Study of Potential Structure in a Spherical IEC Fusion Device," *IEEE Transactions on Plasma Science,* vol. 28, no. 1, pp. 331-346, 2000.

[31] D. R. Boris, J. F. Santarius and G. L. Kulcinski, "Negative ions in inertial electrostatic confinement devices," in *IEEE International Conference on Plasma Science*, San Diego, 2009.